Finite Strain Behavior of Polyurea for a Wide Range of Strain Rates

by

Jongmin Shim

M.S., Massachusetts Institute of Technology (2005)
M.S., Korea Advanced Institute of Science of Technology (2001)
B.S., Korea Advanced Institute of Science of Technology (1998)

Submitted to the Department of Civil and Environmental Engineering
in partial fulfillment of the requirements for the degree of

Doctor of Philosophy in the field of Engineering Mechanics

at the

MASSACHUSETTS INSTITUTE OF TECHNOLOGY

February 2010

ARCHIVES

MASSACHUSETTS INSTITUTE OF TECHNOLOGY
MAR 2 3 2010
LIBRARIES

© 2009 Massachusetts Institute of Technology. All rights reserved.

Signature of Author .....
Department of Civil and Environmental Engineering
November 16, 2009

Certified by .....
Tomasz Wierzbicki
Professor of Applied Mechanics, Department of Mechanical Engineering
Thesis Supervisor

Certified by .....
Dirk Mohr
CNRS Assistant Research Professor, École Polytechnique
Thesis Supervisor

Certified by .....
Eduardo Kausel
Professor of Civil and Environmental Engineering
Thesis Reader

Accepted by .....
Daniele Veneziano
Chairman, Departmental Committee for Graduate Students

Report Documentation Page

Form Approved
OMB No. 0704-0188

Public reporting burden for the collection of information is estimated to average 1 hour per response, including the time for reviewing instructions, searching existing data sources, gathering and maintaining the data needed, and completing and reviewing the collection of information. Send comments regarding this burden estimate or any other aspect of this collection of information, including suggestions for reducing this burden, to Washington Headquarters Services, Directorate for Information Operations and Reports, 1215 Jefferson Davis Highway, Suite 1204, Arlington VA 22202-4302. Respondents should be aware that notwithstanding any other provision of law, no person shall be subject to a penalty for failing to comply with a collection of information if it does not display a currently valid OMB control number.

1. REPORT DATE **FEB 2010**	2. REPORT TYPE	3. DATES COVERED **00-00-2010 to 00-00-2010**
4. TITLE AND SUBTITLE **Finite Strain Behavior of Polyurea for a Wide Range of Strain Rates**		5a. CONTRACT NUMBER
		5b. GRANT NUMBER
		5c. PROGRAM ELEMENT NUMBER
6. AUTHOR(S)		5d. PROJECT NUMBER
		5e. TASK NUMBER
		5f. WORK UNIT NUMBER
7. PERFORMING ORGANIZATION NAME(S) AND ADDRESS(ES) **Massachusetts Institute of Technology,77 Massachusetts Avenue,Cambridge,MA,02139**		8. PERFORMING ORGANIZATION REPORT NUMBER
9. SPONSORING/MONITORING AGENCY NAME(S) AND ADDRESS(ES)		10. SPONSOR/MONITOR'S ACRONYM(S)
		11. SPONSOR/MONITOR'S REPORT NUMBER(S)
12. DISTRIBUTION/AVAILABILITY STATEMENT **Approved for public release; distribution unlimited**		
13. SUPPLEMENTARY NOTES		
14. ABSTRACT		
15. SUBJECT TERMS		

16. SECURITY CLASSIFICATION OF:			17. LIMITATION OF ABSTRACT	18. NUMBER OF PAGES	19a. NAME OF RESPONSIBLE PERSON
a. REPORT **unclassified**	b. ABSTRACT **unclassified**	c. THIS PAGE **unclassified**	**Same as Report (SAR)**	**112**	

Standard Form 298 (Rev. 8-98)
Prescribed by ANSI Std Z39-18

Finite Strain Behavior of Polyurea

for a Wide Range of Strain Rates

by

Jongmin Shim

Submitted to the Department of Civil and Environmental Engineering
on November 16, 2009, in partial fulfillment of the
requirements for the degree of
Doctor of Philosophy in the field of Engineering Mechanics

Abstract

Polyurea is a special type of elastomer that features fast setting time as well as good chemical and fire resistance. It has also good mechanical properties such as its high toughness-to-density ratio and high strain rate-sensitivity, so its application is recently extended to structural purpose to form sandwich-type or multi-layered plates. Those structures can be used for retrofitting of military vehicles and historic buildings, absorbing energy during structural crash.

In order to investigate its behavior of hysteresis as well as rate-sensitivity, three different testing systems are used to cover a wide range of strain rates up to strain of 100%. In view of impact and blast events, the virgin state of polyurea is considered throughout the experiments. First, a hydraulic universal testing machine is used to perform uniaxial compressive loading/unloading tests in order to investigate its hysteresis behavior at low strain rates ($0.001/s$ to $10/s$). Second, two distinct gas-gun split Hopkinson pressure bar [SHPB] systems are employed to cover high strain rates: a nylon bar system ($700/s$ to $1200/s$) and an aluminum bar system ($2300/s$ to $3700/s$). Lastly, the rate-sensitivity for intermediate strain rates ($10/s$ to $1000/s$) is characterized using a modified SHPB system. The device is composed of a hydraulic piston along with nylon input and output bars.

A finite strain constitutive model of polyurea is presented in order to predict the hysteresis and rate-sensitivity behavior. The 1-D rheological concept of two Maxwell elements in parallel is employed within the framework of the multiplicative decomposition of the deformation gradient. Model parameters are calibrated based on the uniaxial compressive tests at various rates. The corresponding algorithms is implemented as a user-defined material subroutine VUMAT for ABAQUS/Explicit, and used to predict the response of polyurea. The proposed constitutive model reasonably captures the experimentally observed asymmetric rate-sensitivity and stress-relaxation behavior: strong rate-sensitivity and large amount of stress relaxation during loading phase, but weak rate-sensitivity and smaller amount of stress relaxation during unloading phase. In order to validate the proposed model, various dynamic punching tests are performed, and their results are well compared with the model predictions during loading although the prediction of unloading behavior can be further improved.

Thesis Supervisor: Tomasz Wierzbicki
Title: Professor of Applied Mechanics, Department of Mechanical Engineering

Thesis Supervisor: Dirk Mohr
Title: CNRS Assistant Research Professor, École Polytechnique

Thesis Reader: Eduardo Kausel
Title: Professor of Civil and Environmental Engineering

Acknowledgments

I would like to express my deep gratitude to Professor Tomasz Wierzbicki for taking me into the Impact and Crashworthiness Lab and providing me with much needed support, guidance, and mentorship. He has enlightened me on how important to keep an engineering mind. My sincere thanks are due Professor Dirk Mohr at École Polytechnique for his mentorship and his valuable insight into my research. He has shown me an excellent example for how to do research. I would also like to offer many thanks to Professor Eduardo Kausel, Professor Jerome J. Connor, and Professor David Roylance for their participation in my thesis committee and for their helpful comments. Moreover, I am indebted to Professor Gerard Gary at École Polytechnique for his guidance into the split Hopkinson pressure systems. The financial support of this work through the Office of Naval Research is also greatly acknowledged.

I would like to thank all the members and alumni of the ICL (Dr. Young-Woong Lee, Dr. Xiaoqing Teng, Dr. Liang Xue, Dr. Li Zheng, Dr. Yuanli Bai, Dr. Carey Walters, Dr. Yaning Li, Ms. Allison Beese, Mr. Meng Luo, Mr. Matthieu Dunand, Ms. Danielle Issa, and Ms. Kirki Kofiani) for creating a cooperative working environment. My thanks are also extended to Ms. Sheila McNary for her administrative assistance.

Life at MIT would be much less interesting without several individuals: previous office-mates (Georgios, Emilio, Matt/Cara and Chris), Korean colleagues in CEE (Joonsang-hyung, Sungjune-hyung, Yunseung-nuna, Jungwuk-hyung, Phillseung-hyung, Sanghyun-hyung, Sangyoon-hyung, Hongchul-hyung and many others), and colleagues from the neighboring labs (Yeunwoo-hyung, Heejin, Hyunjoe-hyung and Shawn). It was a privilege to know all of you.

Finally, my deepest gratitude goes to my family: my wife, Eunkyung, for her constant support and encouragement; my son, Seohyun, for providing me with ineffable joy of life; and my parents and sister for their unconditional love and faith in me. Thank you very much.

Contents

1 Introduction **12**

1.1 Motivation 12

1.2 Objective and Tasks 14

1.3 Outline of Dissertation 14

2 Experimental Work **17**

2.1 Introduction 17

2.2 Experimental Procedures 19

2.2.1 Universal Testing Machine 19

2.2.2 Conventional SHPB Systems 20

2.2.3 Modified SHPB with Hydraulic Actuator 20

2.2.4 Determination of the Stress-Strain Curves 26

2.3 Experimental Results 27

2.3.1 Experiments using the Universal Testing Machine 27

2.3.2 Experiments Using Conventional SHPB Systems 29

2.3.3 Experiments Using the Modified SHPB Systems 33

2.3.4 Comment on the Signal Oscillations 34

2.4 Discussion 37

2.4.1 Experimental Results 37

2.4.2 Intermediate Strain Rate Testing Systems 38

2.5 Conclusion 41

3 Constitutive Modeling **42**

3.1 Introduction . . . 42

3.2 Experimental Investigation . . . 45

3.2.1 Material . . . 45

3.2.2 Relaxation Experiments . . . 45

3.2.3 Continuous Compression Experiments . . . 47

3.2.4 Stair Compression Experiments . . . 47

3.3 Constitutive Model . . . 49

3.3.1 Motivation . . . 49

3.3.2 Homogenization . . . 52

3.3.3 Constitutive Equations for Volumetric Deformation . . . 53

3.3.4 Maxwell Model for Isochoric Deformation . . . 54

3.3.5 Specialization of the Maxwell Model for *Network A* . . . 56

3.3.6 Specialization of the Constitutive Equations for *Network B* . . . 57

3.4 Identification of the Model Parameters . . . 58

3.4.1 Constitutive Equations for Uniaxial Loading . . . 59

3.4.2 Model Calibration . . . 61

3.5 Comparison of Simulation and Experiments . . . 65

3.5.1 Continuous Compression . . . 65

3.5.2 Stair Compression . . . 67

3.5.3 Relaxation . . . 70

3.5.4 Discussion . . . 70

3.6 Conclusions . . . 71

4 Validation Application **73**

4.1 Introduction . . . 73

4.2 Punch Experiments . . . 75

4.2.1 Specimens . . . 75

4.2.2 Experimental Procedure . . . 76

4.2.3 Experimental Results . . . 76

4.3 Constitutive Model . . . 79

4.3.1 Response of *Network A* 80
4.3.2 Response of *Network B* 82
4.3.3 Model Parameter Identification 83
4.4 Numerical Simulations of the Punch Experiments 85
4.5 Discussion on Unloading Behavior of Polyurea 87
4.6 Conclusion 93

5 Conclusion and Suggestions **95**
5.1 Summary of Main Results 95
5.2 Suggestions for Future Studies 96

A Identification of the Wave Propagation Coefficient for Viscoelastic Bars **98**

B List of Papers with Reference to Respective Chapters **100**

List of Figures

2-1 (a) Conventional and (b) Modified SHPB systems. 21

2-2 Identification of Poisson's ratio from the linear relationship between the logarithmic radial and axial strains 28

2-3 Test results from the universal testing machine: (a) True stress-strain curves, (b) True strain versus true strain curves 29

2-4 Propagation coefficient of aluminum bar (first row) and nylon bar (second row). (a)-(c) Longitudinal wave speed and (b)-(d) Attenuation coefficient. 30

2-5 Comparison of forces between input bar and output bar from SHPB tests from aluminum bar tests: (a) $3700/s$, (b) $2300/s$; and nylon bar tests: (c) $1200/s$, (d) $700/s$ 32

2-6 (a) True stress-strain curves, (b) True strain rate versus true strain curves. . . . 33

2-7 Comparison of forces between input bar and output bar from the modified SHPB tests: (a) $1000/s$, (b) $110/s$, (c) $36/s$ and (d) $10/s$ 35

2-8 Test results from the modified SHPB system: (a) True stress-strain curves, (b) True strain rate versus true strain curves. 36

2-9 Comparison of the results from the modified SHPB with those from other two testing methods: (a) True stress-strain curves, (b) True strain rate versus true strain curves. 37

2-10 True stress as a function of the strain rate at selected strain levels: (a) Results of the current study and a fit of Eq. (2.26) to the results from the present study. (b) Comparison of the results with previous studies. 38

3-1 Results of relaxation tests (left column) and corresponding simulations (right column). (a)-(b) True stress histories, (c)-(d) Relaxation moduli histories, (e)-(f) Isochronous stress-strain curves for different instants after the rapid strain loading. 46

3-2 Results of continuous loading/unloading experiments and corresponding simulations. (a) History of applied strain. Note that time in the x-axis is normalized by the total testing duration $|\varepsilon_0/\dot{\varepsilon}_0|$ where $\dot{\varepsilon}_0 = 10^{-3}$, 10^{-2}, 10^{-1}, 10^0, and $10^1/s$. (b) Stress-strain curves obtained from experiments and 48

3-3 Results for stair compression loading/unloading. (a) History of applied strain. Note that time in the x-axis is normalized by the total testing duration $|\varepsilon_0/\dot{\varepsilon}_0|$ where $\varepsilon_0 = 1$ and $\dot{\varepsilon}_0 = 10^{-3}$, 10^{-2}, 10^{-1}, 10^0, and $10^1/s$. (b) Stress-strain curves from experiments and (c) Corresponding simulations. (d) Comparison of results from continuous and stair-type loading/unloading experiments and (e) Corresponding simulations. 50

3-4 Estimation of the behavior of *Network A* using the equilibrium path concept for path concept for different strain rates: (a) $10^{-3}/s$, (b) $10^{-2}/s$, (c) $10^{-1}/s$, (d) $10^0/s$ and (e) $10^1/s$ 51

3-5 Proposed rheological model for polyurea composed of two Maxwell elements in parallel. 52

3-6 Material model parameter identification for *Network A*. (a) Estimated experimental stress-strain curve for *Network A*; (b) Equivalent Mandel stress as a function of the scalar deformation measure ζ; (c) Π_A as function of the equivalent viscous deformation rate $\bar{d}_A$ for the identification of the model parameters P_A and n_A through power-law fit. 63

3-7 Material model parameter identification for *Network B*. (a) Estimated experimental stress-strain curve for *Network B*; (b) Equivalent Mandel stress as a function of the scalar deformation measure ζ; (c) ζ_B as function of the equivalent viscous deformation rate $\bar{d}_B$; identification of the model parameters Q_B and n_B. 66

3-8 Comparison of simulation results and experiments for continuous loading-unloading cycles. (a) $10^{-3}/s$, (b) $10^{-2}/s$, (c) $10^{-1}/s$, (d) $10^{0}/s$ and (e) $10^{1}/s$ 68

3-9 Comparison of simulation results and experiments for stain loading/unloading. (a) $10^{-3}/s$, (b) $10^{-2}/s$, (c) $10^{-1}/s$, (d) $10^{0}/s$ and (e) $10^{1}/s$ 69

4-1 Photos of the experiments with (a) the small punch and (b) the large punch. The second row shows the set up for (c) free boundaries in all lateral directions and (d) for constrained boundary conditions in the width direction. 77

4-2 Applied loading profiles: (a) Applied velocity history; the velocity axis is normalized by the applied initial velocity of either $v_0 = 1mm/s$ or $100m/s$; the time axis is normalized by $|2u_0/v_0|$ with $u_0 = 7mm$; (b) Corresponding applied displacement history. 77

4-3 Measured load-displacement curves for experiments with (a) the small punch, (b) the large punch. 78

4-4 Rheological model of the rate dependent constitutive model for polyurea. 79

4-5 Comparison of simulation results and experiments for continuous loading-unloading cycles. (a) $10^{-3}/s$, (b) $10^{-2}/s$, (c) $10^{-1}/s$, (d) $10^{0}/s$, (e) $10^{1}/s$. 84

4-6 The contour plots of the logarithmic strain in thickness-direction from simulations with $v_0 = 100m/s$ at an indentation depth of $7mm$: (a) small hemispherical indenter, and (b) large hemispherical indenter. The detail in Figure 4-6a shows the locations for which the strain rates $\bar{d}_A$ and $\bar{d}_B$ are plotted in Figure 4-8. . . 86

4-7 Comparison of simulations and experiments. Force-displacement curves for (a) small punch with free lateral boundaries, (b) large punch with the free lateral boundaries, (c) large punch with constraint in the width direction. 88

4-8 Results from the small punch simulation with $v_0 = 100mm/s$ and free lateral boundary conditions at three different locations (labeled by $\boldsymbol{A}$, $\boldsymbol{B}$ and $\boldsymbol{C}$ in Figure 4-6(a): Histories of (a) the strain-like deformation measure, ζ, (b) the viscous strain rate of *Network A*, $\bar{d}_A$, (c) the viscous strain rate of *Network B*, $\bar{d}_B$. Note that the loading direction is reversed at $t = 0.14s$. 89

4-9 Stress-strain curves for a single loading-unloading cycle at $\dot{\varepsilon} = 10^{-2}/s$ as obtained from (a) experiments and (b) simulations. 90

4-10 Comparison of simulation results and experiments for continuous loading/unloading cycles at $\dot{\varepsilon} = 10^{-2}/s$. (a) $\varepsilon_f = -0.5$, (b) $\varepsilon_f = -1.0$, (c) $\varepsilon_f = -1.5$. 92

4-11 Illustration of the Mullins effect. Five compression loading and unlading cycles are performed at the constant strain rate of $10^{-2}/s$ up to the maximum strain of -1.0. The stress is zero between subsequent cycles for about five minutes. . . 93

Chapter 1

Introduction

1.1 Motivation

Polyurea has been generally used for coating purpose due to its good chemical properties such as fast setting time (few minutes or less) and good water/chemical/fire resistance. Polyurea is used on metallic substrates where it provides corrosion and abrasion resistance in harsh environments. Moreover, it has also good mechanical properties such as high toughness for its low density and high rate-sensitivity. Thus, its application is recently extended to structural purpose to form sandwich-type or multi-layered plates, which can be used for retrofitting of military vehicles, historic buildings, gas/oil pipelines and marine structures, absorbing energy during structural crash and holding metal/brick fragments even after structural failure. Like other elastomers, polyurea is viscous material so its mechanical properties are rate dependent. Especially under extreme loading conditions such as blast, projectile and explosive loadings, polyurea becomes very attractive; its lightness is good for operational purpose, and its mechanical strength is enhanced under extreme loading conditions. This structural purpose of polyurea under extreme loading conditions motivates our research on a wide range of strain rates up to large strains. In view of the simulation of blast and impact events, we limit our attention to the mechanical behavior of polyurea in its virgin state.

Limited experimental study of virgin polyurea has been published on the rate-sensitivity behavior for a wide range of strain rates. Polyurea shows a highly nonlinear viscoelastic behavior at finite strains (e.g. Amirkhizi et al., 2006, Bogoslovov and Roland, 2007, Roland

et al., 2007). The stress-strain response of most polymeric materials shows a pronounced strain rate sensitivity at low, intermediate and high strain rates. Various authors published experimental results on the strain rate sensitive response of amorphous glassy polymers (e.g. Chou et al., 1973, Boyce et al., 1988, Walley et al., 1989, Cady et al., 2003, Siviour et al., 2005, Mulliken and Boyce, 2006, Mulliken et al., 2006), crystalline glassy polymers (e.g. Chou et al., 1973, Bordonaro and Krempl, 1992, Cady et al.,2003, Siviour et al., 2005, Khan and Farrokh, 2006) and elastomers (e.g. Gray et al., 1997, Rao et al.,1997, Song and Chen, 2003, 2004, Hoo Fatt and Bekar, 2004, Shergold et al., 2006, Roland, 2006) including polyurea (e.g. Amirkhizi et al., 2006, Roland et al., 2007, Sarva et al., 2006). However, only few experimental studies deal with the intermediate strain rate behavior of elastomers at large deformations. Sarva et al. (2006) performed intermediate strain rate compression tests on polyurea for maximum strains greater than 100% but the strain rates were only $14 \sim 80/s$. The same research group also obtained test results for a strain rate of $800/s$ using a very long aluminum SHPB system. Roland et al. (2007) characterized the tensile behavior of polyurea over a strain rate range of $14 \sim 573/s$ and up to strains of more than 300%.

As for the experimental study on the rate-sensitivity of polyurea, little research has been reported on modeling of virgin polyurea under loading/unloading conditions for a wide range of strain rates. Finite viscoelasticity models of elastomers may be formulated using the so-called hereditary integral approach (Coleman and Noll, 1961, Bernstein et al., 1963, Lianis, 1963, McGuirt and Lianis, 1970, Leonov, 1976, Johnson et al., 1994, Haupt and Lion, 2002, Amirkhizi et al., 2006) but their validity is often limited to a narrow range of strain rates (Yang et al., 2000, Shim et al., 2004, Hoo Fatt and Ouyang, 2007). As an alternative to the hereditary integral approach, the framework of multiplicative decomposition of the deformation gradient (Kröner, 1960 and Lee, 1969) is frequently used in finite viscoelasticity (e.g. Sidoroff, 1974, Lubliner, 1985, Le Tallec et al., 1993, Reese and Govindjee, 1998, Huber and Tsakmakis, 2000). In that framework, the nonlinear viscoelasticity of elastomers is commonly described through a rheological spring-dashpot models of the Zener type (e.g. Roland, 1989, Johnson et al., 1995, Bergström and Boyce, 1998, Huber and Tsakmakis, 2000, Quintavalla and Johnson, 2004, Bergström and Hilbert, 2005, Qi and Boyce, 2005, Areias and Matous, 2008, Hoo Fatt and Ouyang, 2008, Tomita et al., 2008). As for the hereditary integral approach based

models, however, most multiplicative decomposition based models have been also experimentally validated for a narrow range of strain rates. Quintavalla and Johnson (2004) adopted the Bergström-Boyce model to describe the dynamic behavior of cis-(1,4) polybutadiene at high strain-rate of $3000/s$ to $5000/s$. Recently, Hoo Fatt and Ouyang (2008) proposed a thermodynamically consistent constitutive model with modified neo-Hookean rubber elastic springs to describe the steep initial stiffness of virgin butadiene rubber under tensile and compressive loading at intermediate strain rates ($76/s$ to $450/s$).

1.2 Objective and Tasks

The objective of the present dissertation is to develop a finite constitutive model of virgin polyurea for a wide range of strain rates under loading/unloading condition. The material is assumed to be isotropic, and the isothermal condition is considered at the room temperature. In order to achieve the objective, the following tasks are set:

- To characterize the mechanical properties of virgin polyurea at low, intermediate and high strain rates for large strains;
- To develop a finite constitutive model of virgin polyurea;
- To demonstrate the validity of the proposed constitutive model by performing dynamic punching tests and simulations.

1.3 Outline of Dissertation

This dissertation is composed of five chapters. Excluding Chapter 1 and Chapter 5, each chapter addresses one specific topic and it is self-contained because it has already been published or submitted for publications. A list of publications related to this dissertation is presented in Appendix B.

Chapter 2 presents experimental results on polyurea. The strain rate sensitivity of polyurea is characterized using a modified split Hopkinson pressure bar (SHPB) system. The device is composed of a hydraulic piston along with nylon input and output bars. In combination with an advanced wave deconvolution method, the modified SHPB system provides an unlimited

measurement time, and thus can be used to perform experiments at low, intermediate and high strain rates. A series of compression tests of polyurea is performed using the modified SHPB system. In addition, conventional SHPB systems as well as a universal hydraulic testing machine are employed to confirm the validity of the modified SHPB technique at low and high strain rates. The analysis of the data at intermediate strain rates shows that the strain rate is not constant due to multiple wave reflections within the input and output bars. It is demonstrated that intermediate strain rate SHPB experiments require either very long bars ($> 20m$) or very short bars ($< 0.5m$) in order to achieve an approximately constant strain rate throughout the entire experiment.

Chapter 3 is devoted to a constitutive model for polyurea based on the experimental results. Continuous loading and unloading experiments are performed at different strain rates to characterize the large deformation behavior of polyurea under compressive loading. In addition, uniaxial compression tests are carried out with stair-like strain history profiles. The analysis of the experimental data shows that the concept of equilibrium path may not be applied to polyurea. This finding implies that viscoelastic constitutive models of the Zener type are no suitable for the modeling of the rate dependent behavior of polyurea. A new constitutive model is developed based on a rheological model composed of two Maxwell elements. The soft rubbery response is represented by a Gent spring while nonlinear viscous evolution equations are proposed to describe the time-dependent material response. The eight material model parameters are identified for polyurea and used to predict the experimentally-measured stress-strain curves for various loading and unloading histories. The model provides a good prediction of the response under monotonic loading over wide range of strain rates, while it overestimates the stiffness during unloading. Furthermore, the model predictions of the material relaxation and viscous dissipation during a loading/unloading cycle agree well with the experiments.

Chapter 4 presents the validation application for the proposed constitutive model. Punch indentation experiments are performed on $10mm$ thick polyurea layers on a steel substrate. A total of six different combinations of punch velocity, punch size and the lateral constraint conditions are considered. Furthermore, the time integration scheme for a newly-developed rate-dependent constitutive material model is presented and used to predict the force-displacement response for all experimental loading conditions. The comparison of the simulations and the

experimental results reveals that the model is capable to predict the loading behavior with good accuracy for all experiments which is seen as a partial validation of the model assumptions regarding the pressure and rate sensitivity. As far as the unloading behavior is concerned, the model predicts the characteristic stiff and soft phases of unloading. However, the comparison of simulations and experiments also indicates that the overall model response is too stiff. The results from cyclic compression experiments suggest that the pronounced Mullins effect needs to be taken into account in future models for polyurea to improve the quantitative predictions during unloading.

Chapter 5 summarizes the main contributions of the dissertation, and presents suggestions for future studies.

Chapter 2

Experimental Work

2.1 Introduction

Polyurea is a special type of elastomer which is widely used as coating material. It features a fast setting time (few minutes or less) as well as good chemical and fire resistance. Polyurea is frequently used on metallic substrates where it provides corrosion and abrasion resistance in harsh environments. Applications include transportation vehicles, pipelines, steel buildings or marine constructions. More recently, polyurea is also considered for the blast protection of transportation vehicles because of its high toughness-to-density ratio, in particular at high strain rates. It is the objective of this work to characterize the mechanical properties of polyurea at low, intermediate and high strain rates.

The mechanical properties of most metallic engineering materials exhibit only a weak rate-dependence at strain rates below $100/s$. Therefore, metals are usually tested either at very low strain rates ($< 10^{-2}/s$) on universal testing machines or at high strain rates ($> 10^{2}/s$) on split Hopkinson pressure bar (SHPB) systems. The stress-strain response of most polymeric materials on the other hand shows a pronounced strain rate sensitivity at low, intermediate and high strain rates. At small strains, the viscoelastic properties of polymers are typically determined using dynamic mechanical analysis (e.g. McGrum et al. 1997). The characterization of the large deformation response of polymers at low and intermediate strain rates of up to $10/s$ can be performed on hydraulic testing systems (e.g. Yi et al. 2006, Song et al. 2007). As for metals, conventional SHPB systems are employed to characterize the large deformation response

of polymeric materials at high strain rates. However, as discussed by Gray and Blumenthal (2000), low impedance Hopkinson bars are recommended when testing soft polymeric materials (e.g. Zhao et al., 1997, Chen et al., 1999, Sharma et al., 2002). Hoo Fatt and Bekar (2004) developed a pulley system to perform large strain tensile tests on rubber sheets at intermediate and high strain rates. Inspired by this work, Roland et al. (2007) designed a pendulum impact tester to study the tensile properties of elastomers at strain rates of up to about $500/s$. In both testing systems, the issues related to the strain measurements under dynamic loading conditions are circumvented through the use of digital image correlation (DIC) based on high speed camera recordings.

Unlike for high strain rate experiments, the duration of the experiment poses a major challenge when using SHPB systems for intermediate strain rate testing. The experiment duration T_{exp} is given by the ratio of the strain $\varepsilon_{\max}$ at the end of the experiment and the average strain rate $\dot{\varepsilon}$, $T_{exp} = \varepsilon_{\max}/\dot{\varepsilon}$. In order to avoid the superposition of waves, the maximum duration of reliable measurements is limited to the input bar transit time. The input bar transit time is an intrinsic property of the input bar and can only be lengthened by increasing the bar length or by choosing a bar material of low wave propagation speed. In combination with two strain measurements on each Hopkinson bar, wave separation techniques may be used to overcome this limitation for elastic (e.g. Lundberg and Henchoz, 1977, Yanagihara, 1978, Park and Zhou, 1999) and viscoelastic bar systems (e.g. Zhao and Gary, 1997, Bacon 1999, Casem et al., 2003). However, Jacquelin and Hamelin (2001, 2003) as well as Bussac et al. (2002) have shown that so-called two-point measurement wave separation techniques are sensitive to noise. This finding led to the development of a mathematical framework for an advanced wave deconvolution technique which is based on redundant measurements (Bussac et al., 2002). Othman and Gary (2007) demonstrated the applicability of this testing technique to the intermediate strain rate testing of aluminum on a hydraulic actuator driven SHPB system. Othman et al. (2009) also employed this technique when using a $0.82m$ long bar to measure the axial forces in a modified servo-hydraulic machine. In the present work, we make use of a similar testing system as Othman and Gary (2007) to characterize the intermediate strain rate response of the elastomeric material polyurea under compressive loading.

Various authors published experimental results on the strain rate sensitive response of amor-

phous glassy polymers (e.g. Chou et al., 1973, Boyce et al., 1988, Walley et al., 1989, Cady et al., 2003, Siviour et al., 2005, Mulliken and Boyce, 2006, Mulliken et al., 2006), crystalline glassy polymers (e.g. Chou et al., 1973, Bordonaro and Krempl, 1992, Cady et al., 2003, Siviour et al., 2005, Khan and Farrokh, 2006) and elastomers (e.g. Gray et al., 1997, Rao et al., 1997, Song and Chen, 2003, 2004, Hoo Fatt and Bekar, 2004, Shergold et al., 2006, Roland, 2006) including polyurea (e.g. Amirkhizi et al., 2006, Roland et al., 2007, Sarva et al., 2007). However, only few experimental studies deal with the intermediate strain rate behavior of elastomers at large deformations. Sarva et al. (2007) performed intermediate strain rate compression tests on polyurea for maximum strains greater than 1.0, but the strain rates were only $14 \sim 80/s$. The same research group also obtained test results for a strain rate of $800/s$ using a very long aluminum SHPB system. Roland et al. (2007) characterized the tensile behavior of polyurea over a strain rate range of $14 \sim 573/s$ and up to strains of more than 3.0. In the present study, an attempt is made to cover a similar range of strain rates by using the modified SHPB system of Zhao and Gary (1997) in combination with the deconvolution method of Bussac et al. (2002) to perform compression experiments on polyurea.

This paper is organized as follows. Section 2.2 describes all experimental procedures, notably the conventional SHPB and the modified SHPB systems. The experimental results on polyurea are presented in Section 2.3, followed by a discussion of the limitations of the present testing system in Section 2.4.

2.2 Experimental Procedures

Three different testing systems are used to cover a wide range of strain rates: a universal testing machine, a conventional SHPB system, and a modified SHPB system with a hydraulic actuator. Throughout our presentation of the experimental methods, we use the hat symbol to denote the Fourier transforms $\hat{f}(\omega) = \int_{-\infty}^{\infty} f(t)\, e^{-i\omega t} dt$ of time-dependent functions $f(t)$.

2.2.1 Universal Testing Machine

A hydraulic universal testing machine (Model 8800, Instron, Canton MA) is used to perform compression tests at low and intermediate strain rates ($10^{-2} \sim 10/s$). The position of the

vertical actuator is controlled using the software MAX (Instron, Canton). The axial force $F(t)$ is measured using a low profile load cell of a maximum loading capacity of $10kN$ (MTS, Chicago, IL) that has been positioned at a distance of $25mm$ from the specimen. At the same time, the cross-head displacement is measured using an LVDT positioned at a distance of about $1300mm$ above the specimen (integrated in the actuator piston). A DIC system (Vic2D, Correlated Solutions, Columbia, SC) is employed to measure the displacements $u_{in}(t)$ and $u_{out}(t)$ of the top and bottom loading platens, respectively. Furthermore, we make use of the DIC system to quantify the Poisson's ratio of polyurea. Both a thin polymer layer (Teflon) and grease are used to minimize the frictional forces at the contact surface between the specimen and the loading platens.

2.2.2 Conventional SHPB Systems

Two distinct conventional SHPB systems are used in this study:

- The first is an aluminum bar system with a $1203mm$ long striker bar. Experiments of a maximum duration of $T_{exp} = 472\mu s$ can be performed on this system.
- The second SHPB system is composed of thermoplastic nylon bars with a $1092mm$ long striker bar. Thus, a maximum duration of $T_{exp} = 1255\mu s$ is achieved on that system.

Technical details of these systems are given in Table 2.1. The gages for strain history recordings are positioned near the center of the input bar and near the output bar/specimen interface (Table 2.1, Figure 2-1a). Using viscoelastic wave propagation theory (e.g. Zhao and Gary, 1997), we reconstruct the incident and reflected waves based on the input bar strain gage recordings to estimate the force $F_{in}(t)$ and displacement $u_{in}(t)$ at the input bar/specimen interface. Analogously, the force $F_{out}(t)$ and displacement $u_{out}(t)$ at the output bar/specimen interfaces are calculated after reconstructing the transmitted wave based on the output bar strain gage recording.

2.2.3 Modified SHPB with Hydraulic Actuator

The total duration of the loading pulse in an experiment on a conventional SHPB system is limited by the length of the striker bar. Thus, it is usually impossible to reach large strains at

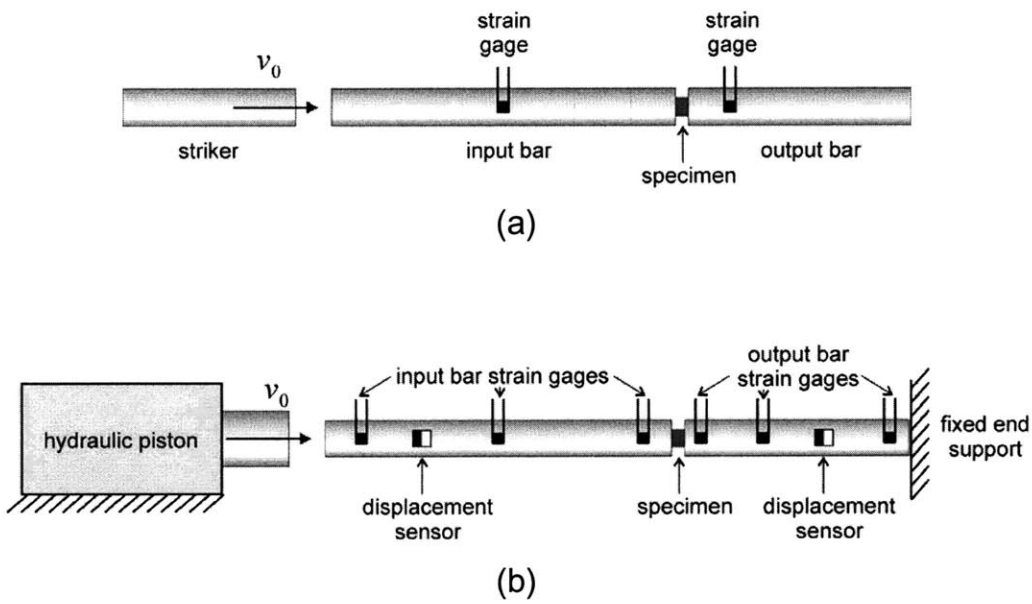

Figure 2-1: (a) Conventional and (b) Modified SHPB systems.

Table 2.1: Specifications of the conventional SHPB sytems

	Aluminum Bar System			Nylon Bar System		
	Striker	Input bar	Output bar	Striker	Input bar	Output bar
Length, L $[m]$	1.203	2.991	1.850	1.092	3.070	1.919
Radius, R $[m]$	20	20	20	16.5	20	20
Longitudinal wave speed, c_0 $(\omega = 0)$ $[m/s]$	5100	5100	5100	1740	1740	1740
Mass density, ρ $[kg/m^3]$	2820	2820	2820	1187	1162	1145
Distance between strain gauge and specimen/bar interface, d $[m]$	-	1.493	0.335	-	1.537	0.394

intermediate strain rates on conventional SHPB systems. To overcome this key limitation, we make use of the modified SHPB system proposed by Zhao and Gary (1997). By substituting the striker bar through a hydraulic actuator, almost infinite loading pulse durations may be achieved. Having this setting, the right end of the output bar needs to be fixed in space as its inertia is no longer sufficient to support the specimen (Figure 2-1b). In order to prevent the failure of the nylon bars under excessive loads (it can be difficult to stop the piston), a fixed end support system is designed such that the bars are released before elastic buckling occurs. Note that the wave superposition in the input and output bars can no longer be avoided when the test duration T_{exp} exceeds the transit time for waves traveling from one bar end to the other. Therefore, a wave separation technique is employed to reconstruct the rightward and leftward travelling waves in the bars based on strain gage measurements. Once both the rightward and leftward traveling waves in the bars are known, the interface forces and velocities may be calculated using the same equations as those for the input bar in a conventional SHPB system. Wave separation techniques in the time domain are efficient for non-dispersive bars (e.g. Lundberg and Henchoz, 1977), but these require more intense computations for waves in dispersive systems (e.g. Bacon, 1999). Here, we adopt the frequency domain based deconvolution technique of Bussac et al. (2002). In particular, displacement measurements are included in addition to strain gage recordings.

Suppose that a strain wave $\varepsilon(x,t)$ in a bar is composed of the rightward traveling wave $\varepsilon_R(x,t)$ and the leftward traveling wave $\varepsilon_L(x,t)$. In terms of Fourier transforms, we have the multiplicative decomposition of the frequency and spatial dependence,

$$\hat{\varepsilon}(x,\omega) = \hat{\varepsilon}_R(x_0,\omega)\, e^{-i\xi(\omega)(x-x_0)} + \hat{\varepsilon}_L(x_0,\omega)\, e^{i\xi(\omega)(x-x_0)} \tag{2.1}$$

where $\hat{\varepsilon}_R(x_0,\omega)$ and $\hat{\varepsilon}_L(x_0,\omega)$ denote the Fourier transform of the respective strain histories at some reference location x_0. Moreover, $\xi(\omega)$ is the frequency-dependent wave propagation coefficient for the respective bar system,

$$\xi(\omega) = \kappa(\omega) + i\bar{\alpha}(\omega) = \frac{\omega}{c(\omega)} + i\bar{\alpha}(\omega) \tag{2.2}$$

with the frequency dependent wave number $\kappa(\omega)$, the longitudinal wave propagation speed

$c(\omega) = \omega/\kappa(\omega)$, and the attenuation coefficient $\bar{\alpha}(\omega)$.

The simplest approach to determine the functions $\hat{\varepsilon}_R(x_0, \omega)$ and $\hat{\varepsilon}_L(x_0, \omega)$ is to measure the strain histories $\varepsilon(x_1, t)$ and $\varepsilon(x_2, t)$ associated with the wave $\varepsilon(x, t)$ at two distinct locations x_1 and x_2 (on the same bar). Subsequently, one can solve the linear system of equations

$$\mathbf{b} = \mathbf{A}\mathbf{x} \tag{2.3}$$

with the unknowns

$$\mathbf{x}(\omega) = \begin{bmatrix} \hat{\varepsilon}_R(x_0, \omega) \\ \hat{\varepsilon}_L(x_0, \omega) \end{bmatrix} \tag{2.4}$$

the measurements

$$\mathbf{b}(\omega) = \begin{bmatrix} \hat{\varepsilon}(x_1, \omega) \\ \hat{\varepsilon}(x_1, \omega) \end{bmatrix} \tag{2.5}$$

and the coefficient matrix

$$\mathbf{A}(\omega) = \begin{bmatrix} e^{-i\xi(\omega)(x_1 - x_0)} & e^{i\xi(\omega)(x_1 - x_0)} \\ e^{-i\xi(\omega)(x_2 - x_0)} & e^{i\xi(\omega)(x_2 - x_0)} \end{bmatrix} \tag{2.6}$$

However, the coefficient matrix becomes singular ($\det \mathbf{A} = \mathbf{0}$) if

$$\xi(\omega) = \frac{n\pi}{x_2 - x_1} \tag{2.7}$$

Bussac et al. (2002) propose an integration method in the complex domain to address this problem. However, the same authors have also shown that the noise in the recorded strain gage signals may still lead to erroneous solutions for $\mathbf{x}(\omega)$. In order to improve the solution of Eq. (2.3) under the presence of measurement noise, it is useful to introduce redundant measurements including force, velocity or displacement measurements. From Eq. (2.1), the Fourier transform of force, velocity and displacement can be expressed as

$$\hat{F}(x, \omega) = E^*(\omega) A \left[\hat{\varepsilon}_R(x_0, \omega) e^{-i\xi(\omega)(x - x_0)} + \hat{\varepsilon}_L(x_0, \omega) e^{i\xi(\omega)(x - x_0)}\right] \tag{2.8}$$

$$\hat{\dot{u}}(x, \omega) = c^*(\omega) \left[-\hat{\varepsilon}_R(x_0, \omega) e^{-i\xi(\omega)(x - x_0)} + \hat{\varepsilon}_L(x_0, \omega) e^{i\xi(\omega)(x - x_0)}\right] \tag{2.9}$$

$$\hat{u}(x,\omega) = l^*(\omega)\left[\hat{\varepsilon}_R(x_0,\omega)\, e^{-i\xi(\omega)(x-x_0)} - \hat{\varepsilon}_L(x_0,\omega)\, e^{i\xi(\omega)(x-x_0)}\right] \tag{2.10}$$

where

$$E^*(\omega) = \rho\left[\frac{\omega}{\xi(\omega)}\right]^2 \quad , \quad c^*(\omega) = \frac{\omega}{\xi(\omega)} \quad \text{and} \quad l^*(\omega) = \frac{i}{\xi(\omega)} \tag{2.11}$$

In the present work, we perform only strain and displacement measurements. Formally, we write

$$\mathbf{b}(\omega) = \begin{bmatrix} \hat{\varepsilon}(x_1,\omega) \\ \vdots \\ \hat{\varepsilon}(x_Q,\omega) \\ \hat{u}(x_{Q+1},\omega) \\ \vdots \\ \hat{u}(x_{Q+R},\omega) \end{bmatrix} \tag{2.12}$$

where the subscripts Q and R represent the number of measurements for strains and displacements, respectively, at the locations x_i $(i = 1, ..., Q+R)$ on the bar. The corresponding matrix $\mathbf{A}(\omega)$ reads

$$\mathbf{A}(\omega) = \begin{bmatrix} e^{-i\xi(\omega)(x_1-x_0)} & e^{i\xi(\omega)(x_1-x_0)} \\ \vdots & \vdots \\ e^{-i\xi(\omega)(x_Q-x_0)} & e^{i\xi(\omega)(x_Q-x_0)} \\ l^*(\omega)\, e^{-i\xi(\omega)(x_{Q+1}-x_0)} & -l^*(\omega)\, e^{i\xi(\omega)(x_{Q+1}-x_0)} \\ \vdots & \vdots \\ l^*(\omega)\, e^{-i\xi(\omega)(x_{Q+R}-x_0)} & -l^*(\omega)\, e^{i\xi(\omega)(x_{Q+R}-x_0)} \end{bmatrix} \tag{2.13}$$

For redundant measurements, the equation $\mathbf{b} = \mathbf{A}\mathbf{x}$ for the unknown $\mathbf{x}$ is over-determined, and cannot be solved exactly. Instead, an approximate solution is calculated by using the least squares method to minimize the scalar error, $e = \|\mathbf{b} - \mathbf{A}\mathbf{x}\|^2 = (\mathbf{b} - \mathbf{A}\mathbf{x})^H(\mathbf{b} - \mathbf{A}\mathbf{x})$. Thus, the approximate solution $\mathbf{x}$ minimizing the error must satisfy the equation $\mathbf{A}^H\mathbf{b} = \mathbf{A}^H\mathbf{A}\mathbf{x}$. As long as the columns of $\mathbf{A}$ are linearly independent, the matrix $\mathbf{A}^H\mathbf{A}$ is positive definite (e.g. Strang, 1985) and the unknown $\mathbf{x}$ can be determined as

$$\mathbf{x} = \left[\mathbf{A}^H\mathbf{A}\right]^{-1}\mathbf{A}^H\mathbf{b} \tag{2.14}$$

where the Hermitian $\mathbf{A}^H$ (complex conjugate and transpose of $\mathbf{A}$) corresponds to the transpose of $\mathbf{A}$ if $\mathbf{A}$ is real (e.g. Magnus and Neudecker, 1988). Note that a least squares solution of similar form has been presented by Hillström et al. (2000) in the context of complex modulus identification based on redundant strain measurements.

In order to rule out the linear dependence of the columns of $\mathbf{A}$, we modify the propagation coefficient $\xi(\omega)$ artificially. In other words, when calculating $\mathbf{A}$, $\xi(\omega)$ is substituted by the modified propagation coefficient $\tilde{\xi}(\omega)$

$$\tilde{\xi}(\omega) = \xi(\omega) + i\bar{\eta}\frac{d\xi(\omega)}{d\omega} \tag{2.15}$$

where $\bar{\eta}$ is a very small, but otherwise arbitrary, negative number; throughout our analysis, we used $\bar{\eta} = -10^{-7}$. The modified propagation coefficient $\tilde{\xi}(\omega)$ corresponds to the linear perturbation of the propagation coefficient $\tilde{\xi}(\omega)$ in the complex frequency domain. As a result, the propagation coefficient is always complex-valued, and thus the singularity condition in Eq. (2.7) can no longer be satisfied. Note that $\bar{\eta}$ introduces a very small artificial attenuation

$$\tilde{\xi}(\omega) = \left[\kappa(\omega) - \bar{\eta}\frac{d\bar{\alpha}(\omega)}{d\omega}\right] + i\left[\bar{\alpha}(\omega) + \bar{\eta}\frac{d\kappa(\omega)}{d\omega}\right] \tag{2.16}$$

As a result, even purely elastic materials ($\bar{\alpha}(\omega) = 0$) exhibit some artificial attenuation (i.e. non-zero imaginary value) which ensures the causality of the waves propagating in a bar (e.g. Bacon, 1999).

In the present study we make use of a modified SHPB system with nylon input and output bars. Table 2.2 summarizes the technical specifications of the testing system. Each bar is equipped with three strain gages and a high contrast grid for optical displacement measurements (Model 100H, Zimmer, Germany). After using Eq. (2.14) to determine the leftward and the rightward traveling waves $\varepsilon_L^{in}\left(x_0^{in}, t\right)$ and $\varepsilon_R^{in}\left(x_0^{in}, t\right)$, the displacement $u_{in}(t)$ and the force $F_{in}(t)$ at the input bar/specimen interface are:

$$\hat{u}_{in}(\omega) = l^*(\omega)\left[\hat{\varepsilon}_R^{in}\left(x_0^{in}, \omega\right)e^{i\xi(\omega)x_0^{in}} - \hat{\varepsilon}_L^{in}\left(x_0^{in}, \omega\right)e^{-i\xi(\omega)x_0^{in}}\right] \tag{2.17}$$

$$\hat{F}_{in}(\omega) = E^*(\omega)A\left[\hat{\varepsilon}_R^{in}\left(x_0^{in}, \omega\right)e^{i\xi(\omega)x_0^{in}} + \hat{\varepsilon}_L^{in}\left(x_0^{in}, \omega\right)e^{-i\xi(\omega)x_0^{in}}\right] \tag{2.18}$$

Table 2.2: Specifications of the modified nylon SHPB sytem

	Input bar	Output bar
Length, L $[m]$	3.123	3.045
Radius, R $[m]$	20	20
Longitudinal wave speed, $c_0\,(\omega = 0)$ $[m/s]$	1740	1740
Mass density, ρ $[kg/m^3]$	1150	1150
Distance between strain gauges and specimen/bar interface, d_{sg} $[m]$	0.61	0.825
	1.515	1.523
	2.623	2.582
Distance between displacement sensor and specimen/bar interface, d_{dm} $[m]$	0.953	2.183

Analogously, the displacement $\hat{u}_{out}(\omega)$ and the corresponding force $\hat{F}_{out}(\omega)$ at the output bar/specimen interface are determined from the output bar measurements.

2.2.4 Determination of the Stress-Strain Curves

The time histories of the displacements and forces at the specimen boundaries, $u_{in}(t)$, $u_{out}(t)$, $F_{in}(t)$ and $F_{out}(t)$ are obtained from applying the inverse Fourier transform $f(t) = \frac{1}{2\pi}\int_{-\infty}^{\infty}\hat{f}(\omega)\,e^{i\omega t}d\omega$ to $\hat{u}_{in}(\omega)$, $\hat{u}_{out}(\omega)$, $\hat{F}_{in}(\omega)$ and $\hat{F}_{out}(\omega)$, respectively. The input force $F_{in}(t)$ is considered as a redundant measurement; it is used to verify the condition of quasi-static equilibrium of a dynamically loaded specimen

$$F_{in}(t) - F_{out}(t) \simeq 0 \tag{2.19}$$

The spatial average of the logarithmic axial strain within the specimen reads

$$\varepsilon(t) = \ln\left(1 + \frac{u_{out}(t) - u_{in}(t)}{L_0}\right) \tag{2.20}$$

where L_0 denotes the initial length of the specimen. Using the output force measurement, we calculate the true stress

$$\sigma(t) = \frac{F_{out}(t)}{A_0} \exp\left[2\nu\varepsilon(t)\right] \tag{2.21}$$

where A_0 is the initial cross-sectional area, and ν is the elastic Poisson's ratio. In the present work, it is assumed that the Poisson's ratio is constant, i.e. it depends neither on the strain nor on the strain rate. The final true stress-strain curve is then found from the combination of the stress and strain history functions

$$\sigma(\varepsilon) = \sigma(t) \circ \varepsilon(t) \tag{2.22}$$

2.3 Experimental Results

All experiments are performed on polyurea. This rubber-like material has a mass density of $1.0g/cm^3$ and an elastic modulus of about $100MPa$.

2.3.1 Experiments using the Universal Testing Machine

Representative stress-strain curves for true strain rates of up to $10/s$ are determined from experiments on the universal testing machine using cylindrical specimens of diameter $D_0 = 10mm$ and length $L_0 = 10mm$. All experiments are carried out under displacement control up to a maximum true compressive strain of 1.0 (which corresponds to an engineering compressive strain of 0.63). In order to achieve a constant true strain rate $\dot{\varepsilon}_0$, a velocity profile $\dot{u}_{in}(t)$ of exponential shape is applied to the top of the specimen

$$\dot{u}_{in}(t) = -L_0\dot{\varepsilon}_0 \exp(\dot{\varepsilon}_0 t) \tag{2.23}$$

The Poisson's ratio is determined from the experiments performed at true compressive strain rates of up to $1/s$. Based on the DIC measurements of the specimen diameter $D = D(t)$, we

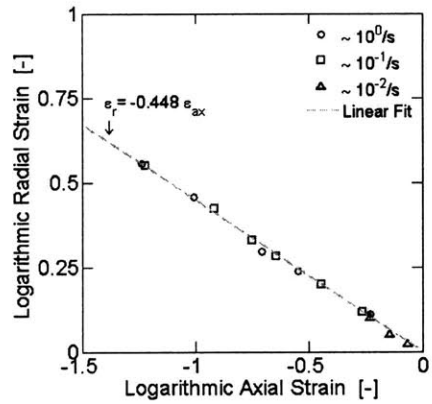

Figure 2-2: Identification of Poisson's ratio from the linear relationship between the logarithmic radial and axial strains

calculate the logarithmic radial strain ε_r,

$$\varepsilon_r = \ln\left(\frac{D}{D_0}\right) \tag{2.24}$$

where D_0 denotes the initial specimen diameter. The experimental data depicted in Figure 2-2 shows the linear relationship between the logarithmic radial strain and the logarithmic axial strain. Upon evaluation of the slope, we find a Poisson's ratio of $\nu = 0.448$.

The data acquisition rate of the DIC system is limited to about $7Hz$. Thus, we only use the DIC system for the slowest experiments and make use of the actuator position measurement (LVDT) to determine the effective axial displacement at higher strain rates. The comparison of the LVDT readout with the DIC measurement yields an overall stiffness of the testing frame of about $100kN/mm$. The measured true stress-strain curves are shown in Figure 2-3a for true strain rates of about $10^{-2}/s$, $10^{-1}/s$, $10^{0}/s$, and $10^{1}/s$. The corresponding true strain rate versus true strain curves are depicted in Figure 2-3b. For the slowest experiment ($\dot{\varepsilon}_0 \simeq 10^{-2}/s$), the slope of the stress-strain curve (Figure 2-3a) decreases significantly at a stress of about 0.1; subsequently, the stress-strain curve changes its shape from concave to convex at an axial strain of about 0.3. Due to the characteristic rubber chain locking behavior, the stress level increases monotonically throughout the entire experiment from $6MPa$ at $\varepsilon = 0.1$ to $13.5MPa$

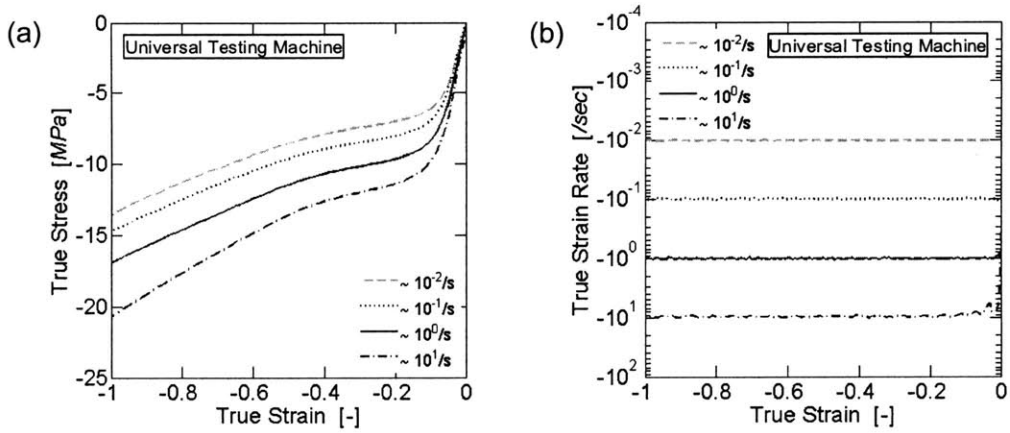

Figure 2-3: Test results from the universal testing machine: (a) True stress-strain curves, (b) True strain versus true strain curves

at $\varepsilon = 1.0$. For the next higher strain rate ($\dot{\varepsilon}_0 \simeq 10^{-1}/s$), the overall stress level is about 12% higher. Similarly, the shape of the stress-strain curve is preserved for strain rates of $10^0/s$ and $10^1/s$, but the stress level increases by 35% and 65%, respectively, compared to that at $10^{-2}/s$.

2.3.2 Experiments Using Conventional SHPB Systems

Appendix B outlines the identification of the frequency dependant coefficients $c(\omega)$ and $\bar{\alpha}(\omega)$ for both the aluminum and nylon bars. The results are presented in Figure 2-4 together with the Pochhammer-Chree solution (e.g. Graff, 1975). These experimentally obtained coefficients are used throughout our analysis of the waves in both the conventional and the modified SHPB systems.

Aluminum Bar System

Experiments at high strain rates are performed on the conventional aluminum SHPB system. Cylindrical polyurea specimens with $D_0 = 20mm$ and $L_0 = 5mm$ are used on the aluminum system. Average strain rates of $\dot{\varepsilon} \simeq 3700/s$ and $\dot{\varepsilon} \simeq 2300/s$ are achieved at striker velocities of $13m/s$ and $9m/s$, respectively. To verify the quasi-static equilibrium throughout the experiments, both the input and output force are depicted in Figures 2-5a and 2-5b. The poor

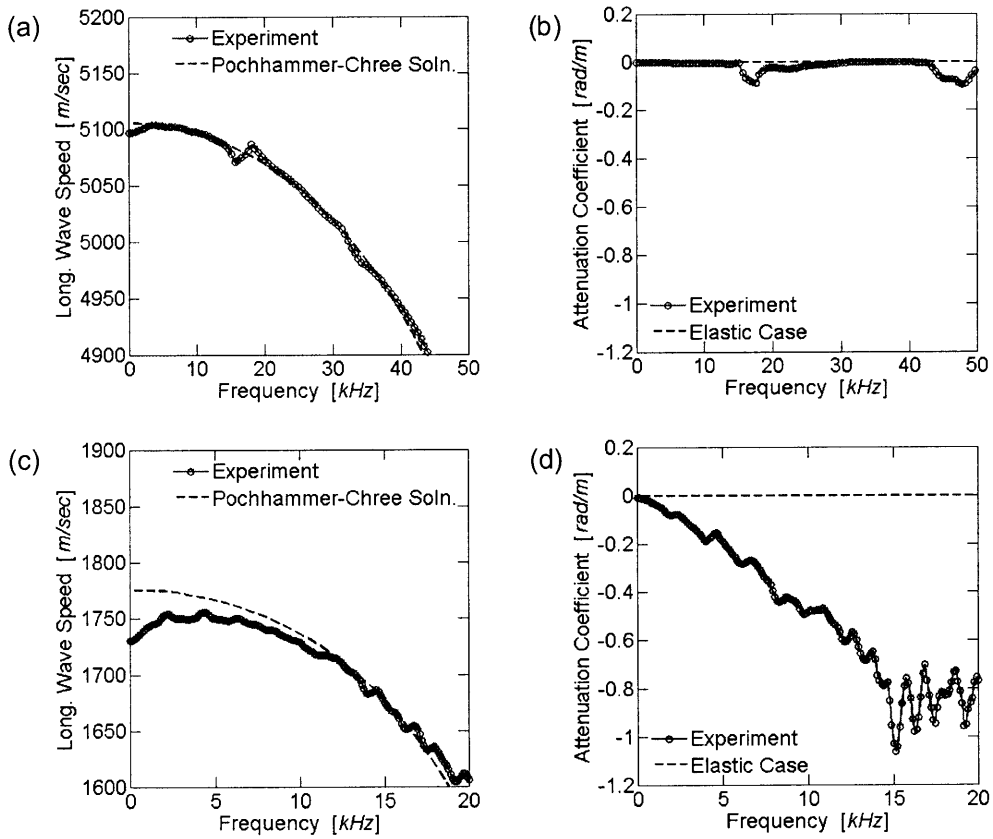

Figure 2-4: Propagation coefficient of aluminum bar (first row) and nylon bar (second row). (a)-(c) Longitudinal wave speed and (b)-(d) Attenuation coefficient.

agreement of the force measurements for $3700/s$ may be read as lack of equilibrium (e.g. Aloui et al., 2008). However, for the present experiments, this observation is attributed to the low signal-to-noise ratio for the input force measurements. Due to the pronounced mismatch between the force amplitude of the incident wave (e.g. $F_{inc} = A_{AL}\rho_{AL}c_{AL}V_{str}/2 \simeq 120kN$ for $13m/s$) and the specimen resistance ($F_{in} = A_{spc}\sigma_{spc} \simeq 15kN$ at $\varepsilon = 0.5$), most of the incident wave is reflected at the input bar/specimen interface which ultimately results in a poor input force measurement (see e.g. Grolleau et al. (2008) for details on the force measurement accuracy). The incident wave exhibits some Pochhammer-Chree oscillations due to the lateral inertia of the $40mm$ diameter aluminum bars. Consequently, we observe some non-monotonic behavior in the stress-strain curves for $3700/s$ and $2300/s$ in Figure 2-6a. The overall shape of the curve is very similar to that for static loading, but the stress level is almost three to four times higher.

Nylon Bar System

Another set of high strain rate experiments ($1200/s$ and $700/s$) are performed using smaller diameter specimens ($D_0 = 10mm$, $L_0 = 5mm$) on the nylon bar SHPB system. Recall that the main reason for changing from aluminum to nylon bars is to increase the maximum duration of the experiments from $T_{exp} = 472\mu s$ to $1255\mu s$. At the same time, the use of nylon significantly reduces the impedance mismatch between the bars and the polyurea specimen. This improves the force measurement accuracy, notably, that of the input force. Striker velocities of $8m/s$ and $6m/s$ are needed to obtain an average strain rate of $\dot{\varepsilon} \simeq 1200/s$ and $\dot{\varepsilon} \simeq 700/s$, respectively. Higher striker velocities would cause inelastic deformation in the bars upon striker impact. On the other hand, for a maximum loading duration of $1255\mu s$, lower striker velocities would not achieve the desired maximum true compressive strain of $\varepsilon = 1.0$.

There are less signal oscillations in the nylon than in the aluminum system because of its higher signal-to-noise ratio. Furthermore, due to the lower striker velocities and the wave attenuation in the nylon input bar, there are less severe Pochhammer-Chree oscillations in the incident wave signal as compared to the aluminum system (see Figure 2-55). Therefore, relatively smooth stress-strain curves are obtained from the dynamic experiments on the nylon bar system (Figure 2-6a). The exact evolution of the true strain rates as a function of the

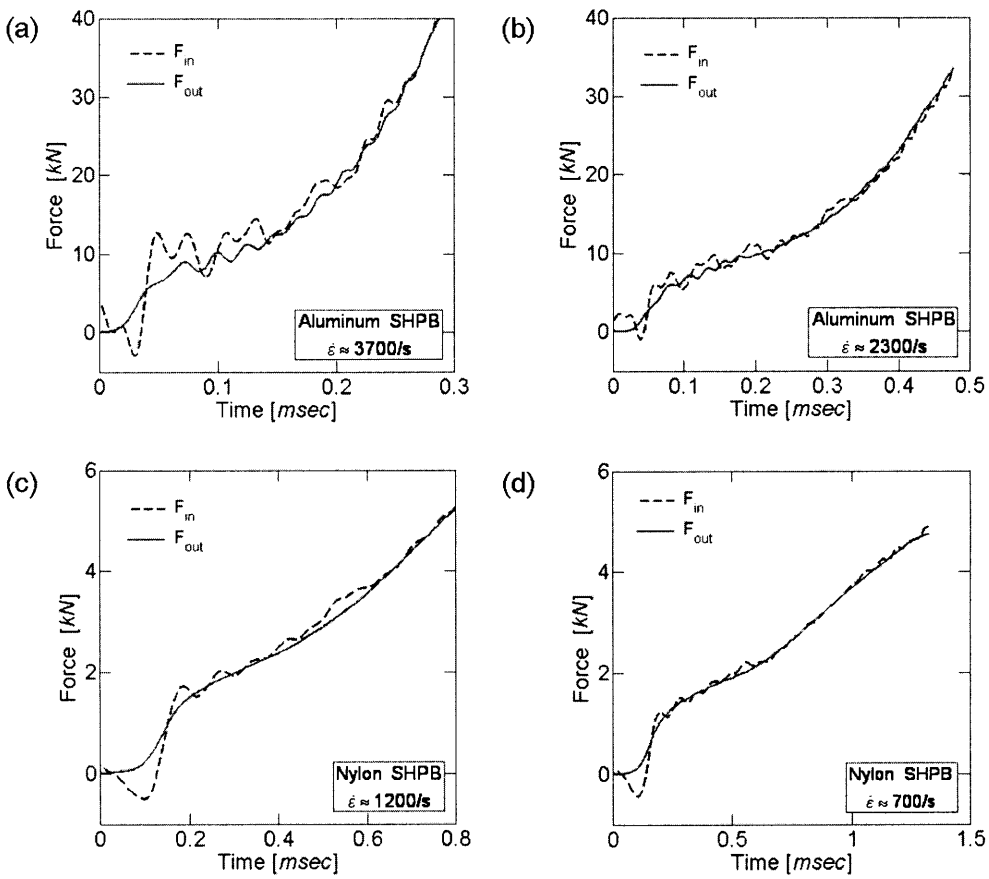

Figure 2-5: Comparison of forces between input bar and output bar from SHPB tests from aluminum bar tests: (a) $3700/s$, (b) $2300/s$; and nylon bar tests: (c) $1200/s$, (d) $700/s$

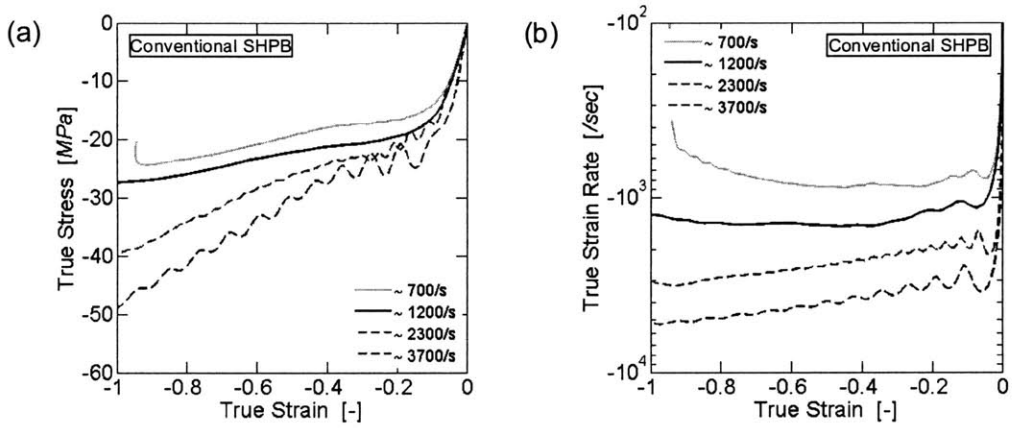

Figure 2-6: (a) True stress-strain curves, (b) True strain rate versus true strain curves.

true strain are shown in Figure 2-6b. Unlike for the experiments on the aluminum bar system, the true strain rate is no longer increasing in a monotonic manner. This is due to the lower amplitude of the incident force (e.g. for $F_{inc} = A_{AL}\rho_{AL}c_{AL}V_{str}/2 \simeq 7.6kN$ for $\dot{\varepsilon} \simeq 700/s$) which is now of the same order of magnitude as the specimen resistance ($F_{in} = A_{spc}\sigma_{spc} \simeq 2.5kN$). Thus, as the specimen resistance increases throughout the experiment, the magnitude of the reflected wave decreases; as a result, despite the logarithmic strain definition, the engineering strain rate no longer increases due to the decreasing interface velocity.

2.3.3 Experiments Using the Modified SHPB Systems

Experiments are performed on the modified nylon SHPB system using the hydraulic actuator in an open mode, which is different from the conventional closed loop mode of servo hydraulic testing machines. In this open loop mode, the user can preset the position of the inlet servo valve. Furthermore, the initial pressure of the in-flowing fluid may be controlled. However, the user has no active control of the actuator velocity throughout the experiment. Actuator piston velocities of up to $5m/s$ may be achieved in this mode of operation. Here, we perform experiments at $4m/s$, $1m/s$, $0.5m/s$, and $0.1m/s$ which resulted in average compressive strain rates of about $1000/s$, $110/s$, $36/s$ and $10/s$.

Three strain gages and one displacement measurement are taken into account (per bar) to

reconstruct the waves in either bar using the above deconvolution technique[1]. The comparison of the measured input and output force histories confirms the quasi-static equilibrium for $110/s$, $36/s$ and $10/s$ (Figure 2-7). The differences between the input and output force for $1000/s$ are associated with the poor quality of the deconvolution based estimate of the input force; the accuracy of the optical displacement measurement system decreases substantially at high loading velocities leading to severe oscillations in the input force history. However, considering that the higher velocity cases (Figure 2-5) show the good force agreement, the quasi-static equilibrium can also be assumed for the strain rate of $1000/s$. A significant force drop is found at $t \simeq 5ms$, $20ms$, and $60ms$ for the strain rates of $110/s$, $36/s$ and $10/s$, respectively. This force drop is due to the premature partial failure of the fixed end support of the output bar that causes a short unloading-reloading cycle. The same force drops are also found in the stress versus strain curve (Figure 2-8a) at strains of 0.55, 0.60 and 0.25 for strain rates of $110/s$, $36/s$ and $10/s$, respectively.

2.3.4 Comment on the Signal Oscillations

There are two characteristic time scales associated with the experiments on the modified SHPB system. The short time scale corresponds to the round trip time of an elastic wave traveling through the specimen, $T_{spc} \simeq 11\mu s$. The second time scale is much longer; it is associated with the round trip of an elastic wave traveling through the input bar, $T_{in} \simeq 3600\mu s$. The experiment at an average strain rate of $1000/s$ remains unaffected by the large time scale as the total duration of the experiment ($T_{exp} \simeq 10^3\mu s$) is still shorter than $T_{in} \simeq 3600\mu s$. However, already at a strain rate of $110/s$, the duration of the experiment ($T_{exp} \simeq 10^4\mu s$) exceeds $T_{in} \simeq 3600\mu s$. As a result, the shape and amplitude of the incident wave is not only determined by the velocity of the hydraulic actuator, but also by the leftward travelling wave that has been reflected by the specimen. Consequently, the incident wave changes with a periodicity of T_{in}. In the present experiments, the first reflected wave is a tensile wave which reduces the initial magnitude of the compressive incident wave. Hence, the rate of loading decreases before the rate of loading increases again after the next period of T_{in}. Therefore, this abrupt change of the loading rate

[1]The only exception is the input bar in the experiment at $110/s$ where one of the three strain gauge signals was not properly recorded. Therefore, only two strain gages and one displacement measurement were taken into account for that experiment.

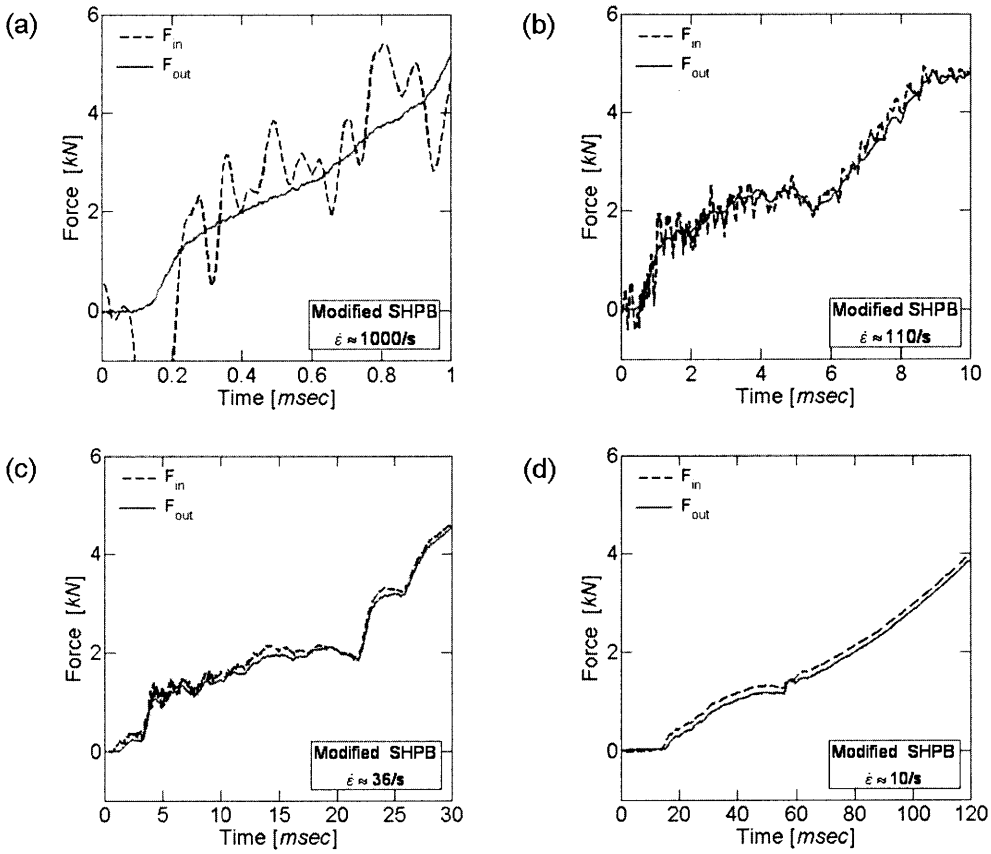

Figure 2-7: Comparison of forces between input bar and output bar from the modified SHPB tests: (a) $1000/s$, (b) $110/s$, (c) $36/s$ and (d) $10/s$

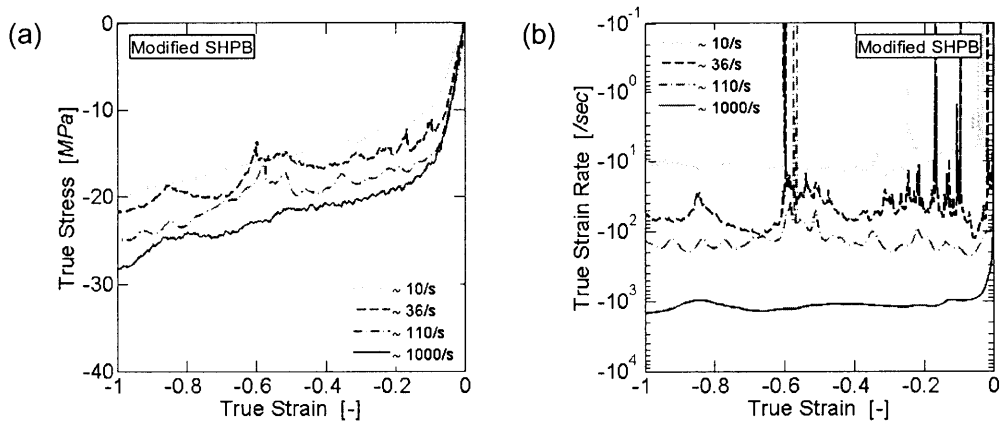

Figure 2-8: Test results from the modified SHPB system: (a) True stress-strain curves, (b) True strain rate versus true strain curves.

has a periodicity of T_{in}. The corresponding strain rate versus strain curve shows a pronounced decrease in strain rate; since the strain increases only little during a period of reduced loading rate, we observe sharp drops in the strain rate versus total strain curve. For lower average strain rates, this number of strain rate drops increases further. Formally, we may write

$$n \simeq \frac{|\varepsilon_{tot}/\dot{\varepsilon}_{ave}|}{T_{in}} \tag{2.25}$$

where n is the number of the expected drops in strain rate associated with the wave reflections in the input bar. This number is 2, 7, and 27 for the experiments at average strain rates of $110/s$, $36/s$ and $10/s$. In the limiting case of static loading, we have $n \rightarrow \infty$ which ultimately results in a constant strain-rate versus strain curve. In addition to loading velocity changes associated with wave reflections in the input bar, our experimental results are also affected by other sources of vibrations. These include wave reflections within the output bar as well as vibrations in the fixed end support system and the hydraulic actuator. Therefore, the exact identification of all strain rate drops in Figure 2-8b according to Eq. (2.25) has been omitted.

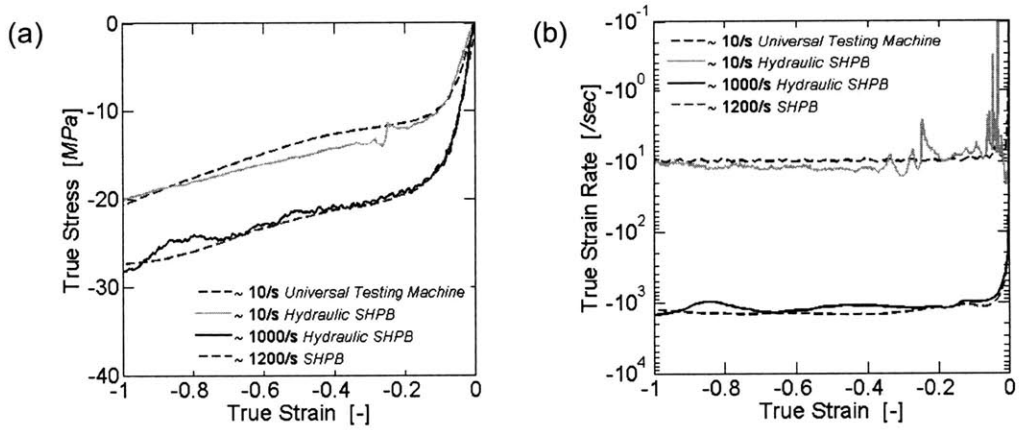

Figure 2-9: Comparison of the results from the modified SHPB with those from other two testing methods: (a) True stress-strain curves, (b) True strain rate versus true strain curves.

2.4 Discussion

2.4.1 Experimental Results

To validate our experimental data, we first checked the consistency among the results obtained from different testing methods. Figure 2-9 shows selected stress-strain curves obtained from the modified SHPB system (dashed lines) next to the results from the conventional SHPB (red solid line) and the universal testing machine (blue solid line). For $1000/s$, the modified SHPB result shows reasonably good agreement with the conventional SHPB curve for $1200/s$. Analogously, for the average strain rate of $10/s$, the stress-strain curve obtained from the modified SHPB test corresponds well to that obtained from the test on the universal testing machine. Recall that the perturbation of the stress-strain curve for the modified SHPB system at about 0.25 strain is due to the partial premature failure of the output bar end support system. The stress level from the modified SHPB is slightly higher after partial support failure which is attributed to differences in the strain rate.

The data in Figure 2-10a show the stress as a function of the strain rate for different levels of strain: 0.1, 0.5 and 0.9. The effect of strain rate is more pronounced at large strains. For instance, at a strain of 0.1, the stress level increases by 317% when increasing the strain rate from $\dot{\varepsilon} \simeq 10^{-2}/s$ to $\dot{\varepsilon} \simeq 3700/s$ (increase $6kN$ from to $19kN$); at a strain of 0.9, the stress level

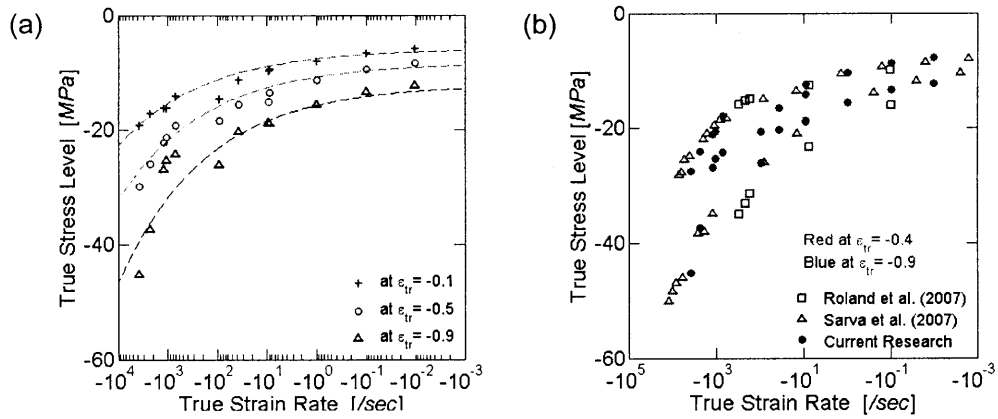

Figure 2-10: True stress as a function of the strain rate at selected strain levels: (a) Results of the current study and a fit of Eq. (2.26) to the results from the present study. (b) Comparison of the results with previous studies.

increases by 360% over the same range of strain rates (from $12.5kN$ at $\dot{\varepsilon} \simeq 10^{-2}/s$ to $45kN$ at $\dot{\varepsilon} \simeq 3700/s$). Using the separable form of strain and strain-rate effect, in the same figure, the following nonlinear empirical function has been fitted to the experimental data:

$$\begin{aligned} \sigma(\varepsilon, \dot{\varepsilon}) &= f(\varepsilon)\, g(\dot{\varepsilon}) \\ &= f(\varepsilon)\left[1 + A\left(\frac{\dot{\varepsilon}}{\dot{\varepsilon}_{ref}}\right)^{B}\right] \end{aligned} \tag{2.26}$$

where $f(\varepsilon)$ is the asymptotic stress-strain curve at infinitely slow loading conditions and $g(\dot{\varepsilon})$ represents the contribution of strain rate sensitivity. Here, the reference strain rate of $\dot{\varepsilon}_{ref} = 10^{-2}/s$ is chosen to be the lowest strain rate in the present experiments. In addition, $A = 0.0899$ is responsible for the amplitude of the strain rate contribution, and $B = 0.249$ represents the sensitivity of the strain rate.

2.4.2 Intermediate Strain Rate Testing Systems

The present experimental study confirms the high strain rate sensitivity of the polyurea material which has been reported in earlier studies. Roland et al. (2007) performed a series of tensile

tests using a custom-made pulley system in a drop tower to perform uniaxial tensile tests at intermediate and high strain rates. Sarva et al. (2007) used an enhanced universal testing machine to perform compression experiments at strain rates of up to $80/s$ while an aluminum SHPB system with a striker bar length of $3m$ has been used to perform experiments at strain rates above $800/s$. The comparison of the present experimental data with the results of Sarva et al. (2007) and Roland et al. (2007) confirms the validity of the measurements with the modified SHPB system (Figure 2-10b).

The implementation of the deconvolution technique by Bussac et al. (2002) leads to a stable algorithm that is convenient to use for the reconstruction of dispersive waves in bars based on redundant measurements. Thus, the theoretical limitation of the duration of experiments on SHPB systems is successfully overcome. In combination with a hydraulic actuator, the entire range of low to high strain rates could be covered using a single testing system. The comparison with conventional SHPB experiments at high strain rates and universal testing machine experiments at low strain rates has confirmed the validity of the modified SHPB technique. However, there are still two difficulties associated with our modified SHPB system which need to be addressed in the future:

- Displacement and/or velocity measurement accuracy: the accuracy of the deconvolution technique relies heavily on accurate displacement measurements (in particular at low strain rates). The present optical technique provided good results for loading velocities of up to $0.5m/s$, but significant errors became visible at larger loading velocities.

- Quality of the loading pulse at specimen interfaces. In order to achieve approximately constant strain rates, the ideal loading pulse should be such that the bar/specimen interfaces move at constant velocities.

The first difficulty may be resolved through the use of improved measurement equipment. Alternatively, the deconvolution technique for high loading velocities may also be applied using strain gage measurements only. However, it is very challenging to overcome the second difficulty. As an intermediate strain rate experiment takes much longer than a wave round trip in the input bar, the input bar/specimen interface velocity is not constant even if the hydraulic piston moves at a constant velocity. Simple wave analysis shows that a period of high velocity loading

is followed by a period of loading at a lower rate; the length of each period corresponds to the round trip time for a wave travelling in the input bar. The same holds true for the output bar/specimen interface velocity which is affected by the round trip time in the output bar. Consequently, the strain rate in our intermediate strain rate experiments was not constant.

For the desired maximum true compressive strain of $\varepsilon = 1.0$, the total duration of an intermediate strain experiment at $50/s$ is $T_{exp} = 20ms$ - irrespective of the specimen geometry. Conceptually, there exist several solutions to this problem:

- Conventional nylon SHPB system with a striker bar length of $1740 \times 0.02 \times 0.5 = 17.4m$ along with a $35m$ long input bar and a $17.5m$ long output bar. In this configuration, all strain gages can be positioned such that the rightward and leftward traveling waves do not superpose at the strain gage locations.

- Conventional nylon SHPB system with a $17.5m$ long striker bar and $17.5m$ long input and output bars. In this case, a deconvolution method needs to be used to reconstruct the waves in the input and output bars. However, the input bar is still sufficiently long to guarantee that the round trip time is greater than the duration of the experiment.

- Hydraulic nylon SHPB system with $17.5m$ long input and output bars. Based on the assumption that the hydraulic piston moves at a constant velocity, this system will provide the same capabilities as the previous system.

As an alternative to very long input and output bars, one may chose the opposite strategy. Note that the magnitude of the oscillations is proportional to the change in force level in the specimen over the time T_{in}. Thus, the shorter the input bar, the smaller the oscillation magnitude. One could therefore envision very short (e.g. $< 0.5m$) small diameter input and output bars. In this case, we have $T_{in} = 0.57ms$ and hence $T_{in} \ll T_{exp}$.

However, since the modified SHPB system requires two displacement measurement sensors (notably for low strain rate experiments), one can also use these sensors to measure directly the displacements of the respective bar/specimen interfaces. Hence the strain history can be measured without using the deconvolution algorithm. The bars would therefore only serve as load cell to measure the force history. Unless the quasi-static equilibrium needs to be verified

experimentally, a single force measurement is satisfactory. Moreover, it may be worth considering a piezoelectric sensor to measure the force, thereby completely eliminating the use of bars to perform the experiments at low, intermediate and high strain rates. As our hydraulic piston cannot provide a constant loading velocity above $0.5m/s$, a striker bar may also be used to load the specimen. The only unknown which is left in this system is the realization of the "fixed" boundary condition. Further research needs to be carried out to design a support point that does not introduce spurious oscillation into the testing system.

2.5 Conclusion

The modified SHPB system of Zhao and Gary (1997) has been used to perform compression tests on polyurea at low, intermediate and high strain rates. It is composed of nylon input and output bars, while the striker bar is substituted by a hydraulic actuator. Using the deconvolution technique by Bussac et al. (2002), the time limitation of conventional SHPB systems may be overcome, thereby enabling the use of the modified SHPB system for low and intermediate strain rate experiments of long duration. The experiments confirm the known strain rate sensitivity of polyurea. The measured stress levels correspond well to earlier results which have been obtained from tests on conventional SHPB systems with very long bars. Although the intrinsic time limitation of SHPB systems could be overcome, this study also shows that it is still not possible to perform experiments at reasonably constant strain rates with this technique. This is due to the finite length of the input and output bars which causes a periodic change in loading velocity. It is shown that intermediate strain rate SHPB experiments require either very long bars ($> 20m$) or very short bars ($< 0.5m$) in order to achieve an approximately constant strain rate throughout the entire experiment.

Chapter 3

Constitutive Modeling

3.1 Introduction

Polyurea is used to mitigate structural damage during impact loading because of its good damping performance. In addition, it is utilized by various industries because of its fast setting time as well as its good chemical and fire resistance. Polyurea has found applications in army vehicles for blast protection because of its high toughness-to-density ratio at high strain rates. Polyurea shows a highly nonlinear viscoelastic behavior at finite strains (e.g. Amirkhizi et al., 2006, Bogoslovov and Roland, 2007, Roland et al., 2007, Shim and Mohr, 2009a). The mechanical properties of linearly viscoelastic materials may be described by the relaxation modulus (or creep compliance) which is independent of strain magnitude. However, nonlinear viscoelasticity is characterized by a decrease (or increase) of the relaxation modulus (or creep compliance) with increasing strain or decreasing stress (e.g. Brinson and Brinson, 2008).

Most finite viscoelasticity models of elastomers are formulated using either (1) the so-called hereditary integral approach or (2) the framework of multiplicative decomposition of the deformation gradient. Motivated by linear viscoelastic models, hereditary integral models are formulated in terms of relaxation or memory functions (e.g. Lockett, 1972). Widely used single integral theories are the theory of Finite Linear Viscoelasticity (Coleman and Noll, 1961) and the BKZ theory (Bernstein et al., 1963); both make use of several relaxation/memory functions. Significant efforts have been made to improve these theories and to reduce the number of required material parameters (e.g. Lianis, 1963, McGuirt and Lianis, 1970, Leonov, 1976, Johnson

et al., 1994, Haupt and Lion, 2002). Nonlinear viscoelastic behavior is often considered as the superposition of a rate-independent nonlinear elastic response (so-called equilibrium part) and a viscosity-induced overstress contribution which is described through fading memory functions. Most nonlinear viscoelastic constitutive models have been experimentally validated at very low strain-rates of $0.1/s$ or less. Only few papers deal with the nonlinear viscoelastic behavior of elastomers at intermediate and high strain-rates ($1/s$ to $1000/s$). Using the hereditary integral approach, Yang et al. (2000) and Shim et al. (2004) proposed a phenomenological constitutive model to predict the behavior of silicon rubber at high strain rates ($900/s$ to $3000/s$). Hoo Fatt and Ouyang (2007) adopted the integral approach to model the response of butadiene rubber at strain rate ranging from $76/s$ to $450/s$. The validity of most hereditary integral approach based models is limited to a narrow range of strain rates due to the use of only one relaxation time period (Yang et al., 2000 and Shim et al., 2004) or a constant memory function (Hoo Fatt and Ouyang, 2007). In general, the hereditary integral approach is very useful in describing finite viscoelastic behavior, but its successful application to the real test data depends strongly on the effectiveness of the rather complex relaxation or memory function calibration procedures.

Compared to hereditary integral models, the multiplicative decomposition of the deformation gradient typically leads to models with material parameters that can be easily identified from experiments. The concept of the multiplicative decomposition of the deformation gradient (Kröner, 1960, and Lee, 1969) was initially applied to finite viscoelasticity by Sidoroff (1974) and further explored by others (e.g. Lubliner, 1985, Le Tallec, 1993, Reese and Govindjee, 1998, Huber and Tsakmakis, 2000). The nonlinear viscoelasticity is commonly described through a rheological spring-dashpot model that features a rate-independent equilibrium part and a rate-dependent viscous part. In particular, Zener models are widely used (e.g. Roland, 1989, Johnson et al., 1995, Bergström and Boyce, 1998, Huber and Tsakmakis, 2000, Quintavalla and Johnson, 2004, Bergström and Hilbert, 2005, Qi and Boyce, 2005, Tomita et al., 2008, Areias and Matous, 2008). Zener models are composed of a spring (rate-independent part) in parallel with a Maxwell element (rate-dependent part). The constitutive model of the time-dependent part includes an evolution equation for the viscous deformation. The simplest evolution equation is a linear viscous flow rule (e.g. Amin et al., 2002, Johlitz et al., 2007). However, experiments have shown that the viscosity at finite strains is a function of the driving

stress (e.g. Amin et al., 2006), the strain (e.g. Amin et al., 2006, Hoo Fatt and Ouyang, 2008) and/or the strain-rate (e.g. Khan et al., 2006). Thus, nonlinear viscous flows rules have been developed using a micro-mechanism inspired approach (e.g. Bergström and Boyce, 1998, Palm et al., 2006) or a purely phenomenological approach (e.g. Khan and Zhang, 2001, Colak, 2005, Amin et al., 2006, Khan et al., 2006, Hoo Fatt and Ouyang, 2008).

In order to represent the equilibrium contribution as the nonlinear elastic spring, rubber elasticity models are employed using the conventional material types such as Neo-Hookean (e.g. Johlitz et al., 2007), Mooney-Rivlin, (e.g. Huber and Tsakmakis, 2000), or Arruda and Boyce's (1993) eight-chain model (e.g. Bergström and Boyce, 1998, Tomita et al., 2008). Other research groups (e.g. Amin et al., 2002, 2006, Hoo Fatt and Ouyang, 2008) used modified conventional material models to describe the high initial stiffness and the subsequent strain hardening.

Although many researcher have recently reported on experimental behavior of various polymeric materials for a wide range of strain rates (e.g. Khan and Farrokh, 2006, Mulliken and Boyce, 2006, Sarva et al., 2007), little research has been reported on the modeling of elastomeric materials for loading and unloading for a wide range of strain rates. As for the hereditary integral approach based models, most multiplicative decomposition based models have been experimentally validated for a narrow range of strain rates. Quintavalla and Johnson (2004) adopted the Bergström-Boyce model to describe the dynamic behavior of cis-(1,4) polybutadiene at high strain-rate of $3000/s$ to $5000/s$. Recently, Hoo Fatt and Ouyang (2008) proposed a thermodynamically consistent constitutive model with modified neo-Hookean rubber elastic springs to describe the steep initial stiffness of virgin butadiene rubber under tensile and compressive loading at intermediate strain rates ($76/s$ to $450/s$).

The present work focuses on the modeling of the loading and unloading response of polyurea over a wide range of strain rates (from $10^{-3}/s$ to $10^{1}/s$) and at large compressive strains (up to 1.0). Using the framework of the multiplicative decomposition of the deformation gradient, the rheological concept of two parallel Maxwell elements is employed to develop a nonlinear viscoelastic finite strain constitutive model. Guided by similar developments in area of rate-dependent plasticity models for glassy polymers (e.g. Qi and Boyce, 2005, Anand and Ames, 2006, Anand et al., 2009, Ames et al., 2009, Ayoub et al., 2009), the high stiffness of elastomers at small deformations is modeled using Hencky's strain energy function. In view of the simula-

tion of blast and impact events, we limit our attention to the mechanical behavior of polyurea in its virgin state. After presenting all experimental results in Section 3.2, the constitutive model is detailed in Sections 3.3 and 3.4. A discussion of the comparison of simulations and experimental results for polyurea is given in Section 3.5.

3.2 Experimental Investigation

3.2.1 Material

The polyurea specimens used in the study are extracted from a $12.7mm$ thick polyurea DragonShield-HT Explosive Resistant Coating (ERC) layer on a steel armor plate. After separation from the plates, the polyurea specimens of diameter $D_0 = 10mm$ and length $L_0 = 10mm$ are machined using conventional milling procedures. The shelf life of the polyurea prior to testing was about 4 years. All experiments are performed on polyurea in its virgin state (condition after curing. no prior mechanical loading history).

3.2.2 Relaxation Experiments

The nonlinearity of the viscoelastic behavior of polyurea at low and intermediate strain rates is identified from relaxation tests. Using a hydraulic universal testing machine (Model 8800, Instron), the material is rapidly loaded to a prescribed strain level at the beginning of the experiment. The strain is subsequently kept constant while stress relaxation takes place. Nine relaxation tests are performed for true compressive strains ranging from $\varepsilon_0 = 0.048$ to 1.0. The engineering strain rate during the rapid loading phase was about $0.48/s$. In order to capture the short-term viscoelastic behavior, the sampling frequency of the data was $5kHz$; the stress is recorded for about 10 minutes to identify the long-term behavior. Figure 3-1a shows the recorded stress histories for various constant strain loadings. While the test duration was not long enough to observe the asymptotic long-term behavior (i.e. equilibrium modulus), the results indicate that the sampling frequency of $5kHz$ is high enough to capture the asymptotic short-term viscoelastic behavior (i.e. initial relaxation modulus).

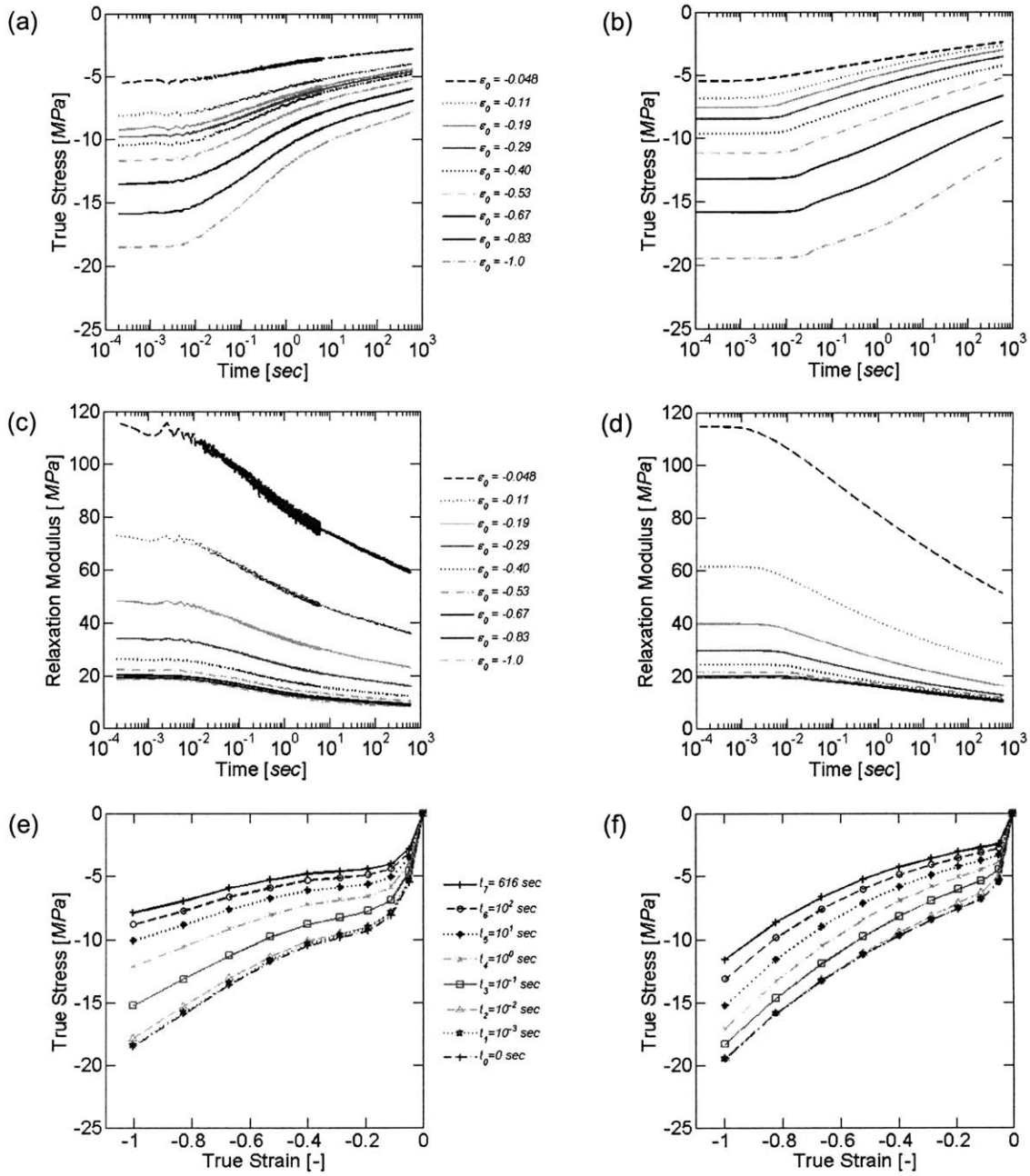

Figure 3-1: Results of relaxation tests (left column) and corresponding simulations (right column). (a)-(b) True stress histories, (c)-(d) Relaxation moduli histories, (e)-(f) Isochronous stress-strain curves for different instants after the rapid strain loading.

The relaxation moduli are computed using the definition

$$H(t) = \frac{\sigma(t)}{\varepsilon_0} \tag{3.1}$$

where $\sigma(t)$ is the time history of the measured true stress for a constant strain of ε_0 (Figure 3-1a). The corresponding relaxation modulus histories (Figure 3-1c) clearly demonstrate the nonlinear viscoelastic nature of the material response: the relaxation modulus decreases from $120MPa$ (at the strain of -0.048) to $20MPa$ (at the strain of -1.0) at the beginning of relaxation; after more than 10 minutes, the corresponding relaxation moduli are $60MPa$ and $10MPa$, respectively. The strong nonlinear nature of the viscoelastic behavior becomes also apparent when plotting the isochronous stress-strain curves (Figure 3-1e).

3.2.3 Continuous Compression Experiments

In addition to relaxation experiments, constant strain rate loading and unloading tests are performed at absolute true strain rates between 10^{-3} and $10^{1}/s$ (Figure 3-2a). The measured true stress versus logarithmic strain curves for five different strain rates are summarized in Figure 3-2b. At least two tests are performed at each strain rate to confirm the repeatability of the experimental results. During the loading phase, the observed stress level exhibits strong strain rate sensitivity. For example, the observed stress level for $10^{-3}/s$ is about twice as high as for $10^{1}/s$. However, during unloading, all the stress-strain curves seem to converge to the same curve regardless of the unloading strain rate.

3.2.4 Stair Compression Experiments

In order to investigate the stress relaxation behavior during loading and unloading, experiments are performed with stair-type strain history profiles. Figure 3-3a shows the applied strain history as a function of the normalized time $t\,|\dot{\varepsilon}/\varepsilon_0|$. The same maximum strain of $\varepsilon_0 = -1.0$ is chosen for all experiments. Experiments are performed for $|\varepsilon_0| = 10^{-3}/s$, $10^{-2}/s$, $10^{-1}/s$, $10^{0}/s$ and $10^{1}/s$. All measured stress-strain curves are depicted in Figure 3-3b. The results from the stair compression tests confirm the previous observation of high strain rate sensitivity during loading phase along with nearly rate independent behavior during unloading. Also the magnitude of

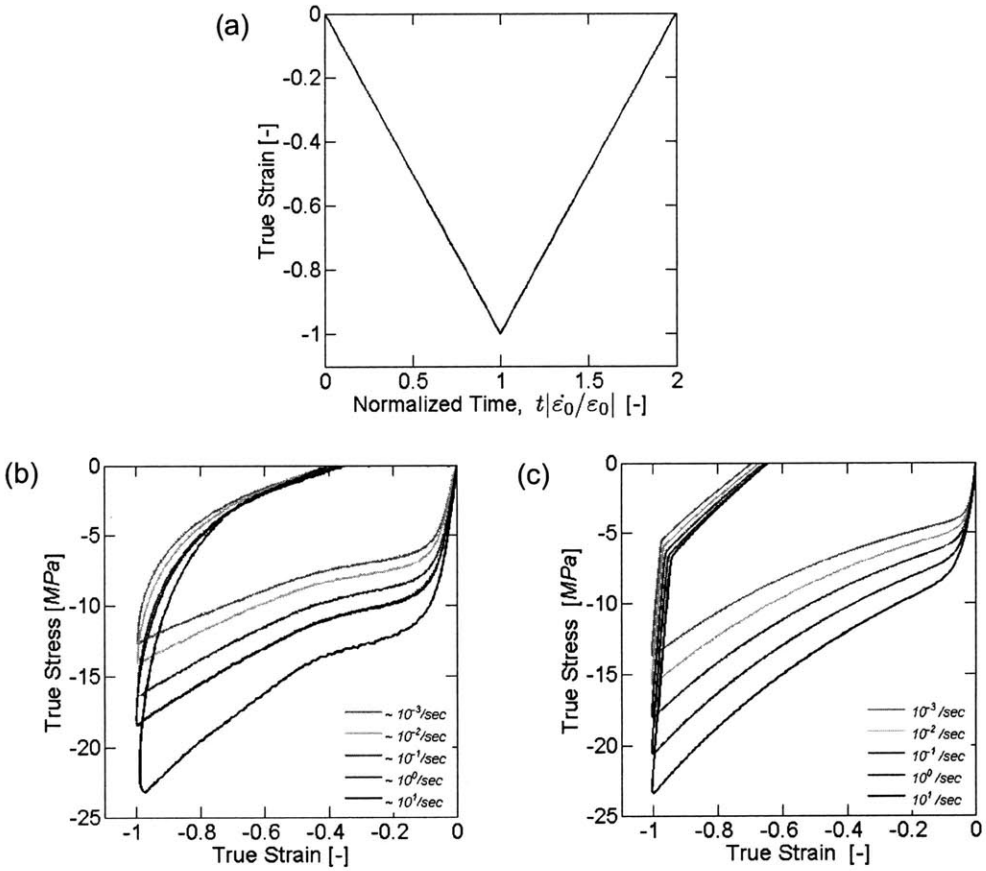

Figure 3-2: Results of continuous loading/unloading experiments and corresponding simulations. (a) History of applied strain. Note that time in the x-axis is normalized by the total testing duration $|\varepsilon_0/\dot{\varepsilon}_0|$ where $\dot{\varepsilon}_0 = 10^{-3}$, 10^{-2}, 10^{-1}, 10^{0}, and $10^{1}/s$. (b) Stress-strain curves obtained from experiments and

stress relaxation during the loading phase is found to be larger than that during unlading. The superposition of the results from the monotonic and stair compression experiments (Figure 3-3d) shows that the specimens recover the virgin state resistance (described by the curves from the monotonic tests) after each relaxation period in the stair compression experiment. The resistance recovery appears to be slower for large strains and high strain rates.

3.3 Constitutive Model

3.3.1 Motivation

In the framework of multiplicative decomposition of the deformation gradient, models of the Zener type (Maxwell element in parallel with a spring) are widely used since these can effectively represent the nonlinear viscoelastic behaviors of many elastomers. For Zener models, it is common to identify the equilibrium path and the over-stress contribution from the experimental stress-strain curves. The equilibrium path can be determined in an approximate manner from two alternative approaches: (1) taking the mid-path of stress-strain curves from the monotonic loading and unloading test (e.g. Bergström and Boyce, 1996), (2) connecting the stress relaxation mid-points between loading and unloading phase from the stair-type compression tests (e.g. Qi and Boyce, 2005). Figure 3-4 shows the equilibrium paths that have been identified from the continuous compression tests at different strain rates. The summary plot in Figure 3-66a clearly shows that the identified equilibrium paths are not identical, i.e. the identified equilibrium path depends on the strain rate. For instance, at a strain of -1.0, an equilibrium stress of $-10MPa$ is found from the experiment at $10^{-3}/s$ while an equilibrium stress of $-17MPa$ is obtained from the experiment at $10^{1}/s$. This important observation is confirmed by the stair-type compression tests. Recall from Figure 3-33b that the amount of stress relaxation is different for loading and unloading. Thus, it is concluded that the concept of equilibrium path breaks down in the case of polyurea. Consequently, rheological models of the Zener type will not be able to describe the nonlinear viscoelastic behavior of polyurea for both loading and unloading.

In models of the Zener type, the equilibrium part is represented by a spring element. Qi and Boyce (2005) explained in their paper on the micro-mechanism inspired constitutive modeling

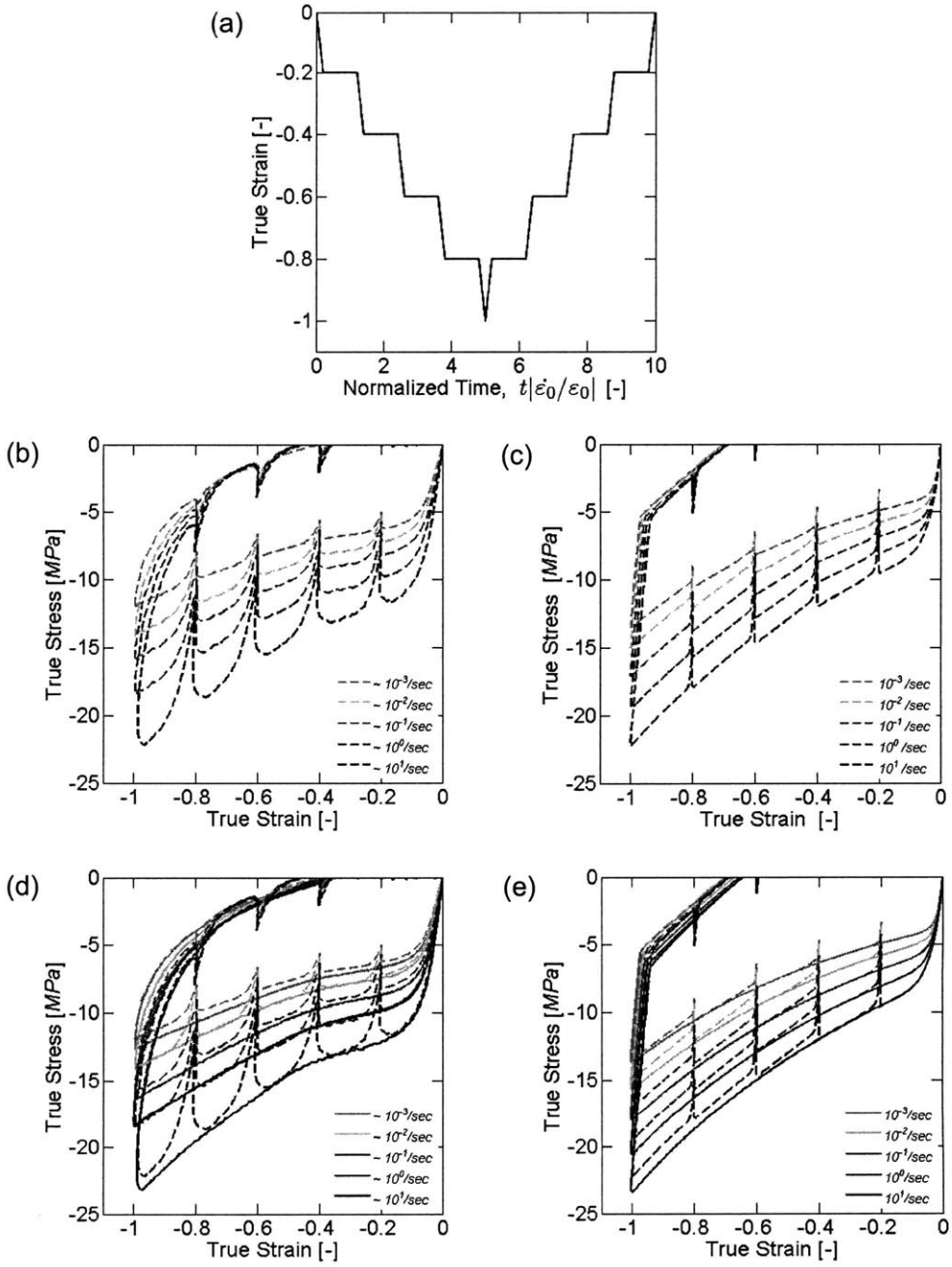

Figure 3-3: Results for stair compression loading/unloading. (a) History of applied strain. Note that time in the x-axis is normalized by the total testing duration $|\varepsilon_0/\dot{\varepsilon}_0|$ where $\varepsilon_0 = 1$ and $\dot{\varepsilon}_0 = 10^{-3}$, 10^{-2}, 10^{-1}, 10^{0}, and $10^{1}/s$. (b) Stress-strain curves from experiments and (c) Corresponding simulations. (d) Comparison of results from continuous and stair-type loading/unloading experiments and (e) Corresponding simulations.

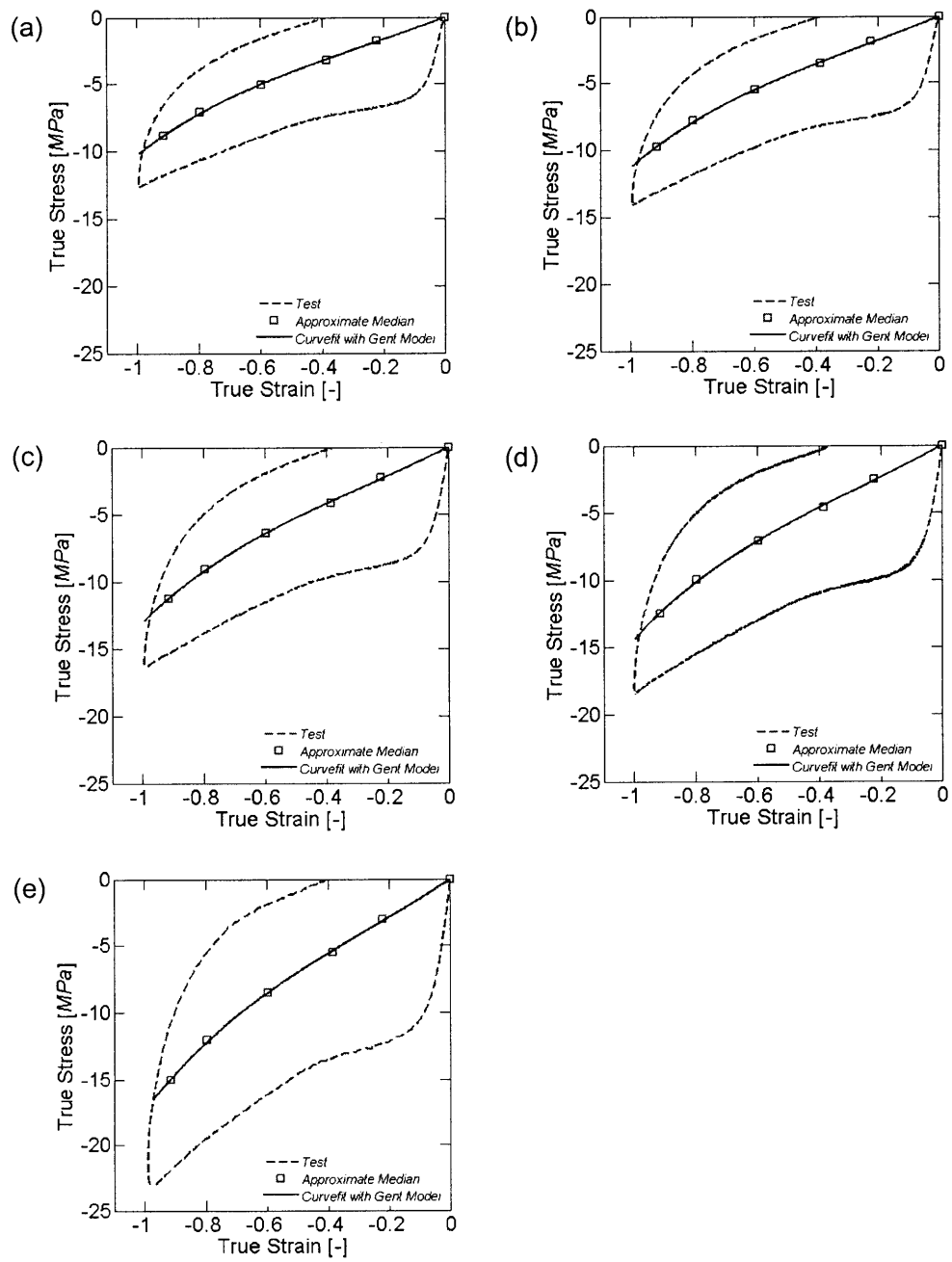

Figure 3-4: Estimation of the behavior of *Network A* using the equilibrium path concept for path concept for different strain rates: (a) $10^{-3}/s$, (b) $10^{-2}/s$, (c) $10^{-1}/s$, (d) $10^{0}/s$ and (e) $10^{1}/s$

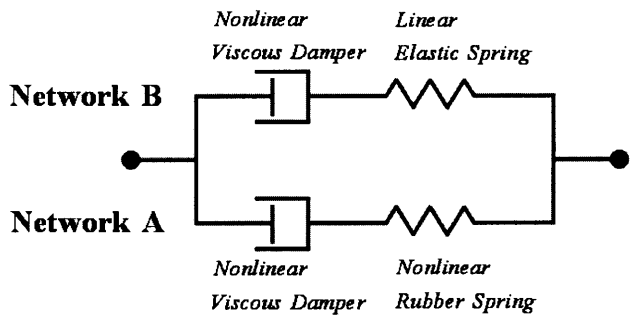

Figure 3-5: Proposed rheological model for polyurea composed of two Maxwell elements in parallel.

of thermoplastic polyurethanes that the spring element associated with the equilibrium path represents the entropic resistance of the soft domains in polyurethanes, while the rate dependent behavior of the hard part is represented by the Maxwell element of the Zener model. Due to the apparent rate dependency of the calculated equilibrium paths, we substitute the spring of the Zener model by another Maxwell element. The resulting rheological model, two Maxwell springs in parallel (Figure 3-5), has already been considered in the past by Boyce et al. (2000) and Dupaix and Boyce (2007) to describe the finite strain behavior of amorphous polymers. In the context of amorphous polymers near glass transition temperature, two Maxwell elements have been used to represent the rate-dependent inter- and intra-molecular network resistances under monotonic loading conditions.

In the following, we outline the constitutive equations for each of the four basic elements of our rheological model. Throughout our presentation, we refer to the Maxwell element that is predominantly associated with the deformation resistance of the soft domain of polyurea as "*Network A*", while the Maxwell element associated with the effect of the hard domain is referred to as "*Network B*".

3.3.2 Homogenization

The macroscopic deformation gradient $\mathbf{F}_{tot}$ is decomposed into a rotation free volumetric part $\mathbf{F}_{vol}$,

$$\mathbf{F}_{vol} = J^{1/3}\mathbf{1} \quad \text{with} \quad J = \det \mathbf{F}_{tot} \tag{3.2}$$

and an isochoric part $\mathbf{F}$

$$\mathbf{F} = J^{-1/3}\mathbf{F}_{tot} \tag{3.3}$$

The constitutive model for the stresses induced by isochoric deformation is developed with the Taylor assumption in mind, i.e. the isochoric deformation gradients within both networks, $\mathbf{F}_A$ and $\mathbf{F}_B$, equal the macroscopic isochoric deformation gradient

$$\mathbf{F} = \mathbf{F}_A = \mathbf{F}_B \tag{3.4}$$

while the deviatoric part of the macroscopic Cauchy stress $\mathbf{T}$ corresponds to the spatial average of the local stress fields

$$\mathrm{dev}\mathbf{T} = \frac{1}{\Omega}\left[\int_A \boldsymbol{\sigma} d\Omega_A + \int_B \boldsymbol{\sigma} d\Omega_B\right] \tag{3.5}$$

where $\boldsymbol{\sigma}$ describes the local deviatoric stress fields, Ω is the total volume of the representative volume element, and Ω_A and Ω_B are the corresponding volumes of *Networks* A and B, respectively. In the context of micromechanism-inspired polymer models, the role of the microstructure is typically neglected. Instead, the constitutive equations for the individual phases predict a weighted macroscopic Cauchy stress (in the present case the weighted deviator stresses $\mathbf{T}_A$ and $\mathbf{T}_B$) such that the macroscopic stress deviator can be written as

$$\mathrm{dev}\mathbf{T} = \mathbf{T}_A + \mathbf{T}_B \tag{3.6}$$

3.3.3 Constitutive Equations for Volumetric Deformation

The volume change of polyurea under mechanical loading is very small as compared to the magnitude of isochoric deformation. For simplicity, we assume a linear elastic relationship between the logarithmic volumetric strain and the hydrostatic part of the macroscopic Cauchy stress tensor

$$\frac{\mathrm{tr}\mathbf{T}}{3} = \kappa\frac{\ln J}{J} \tag{3.7}$$

where κ denotes the bulk modulus.

3.3.4 Maxwell Model for Isochoric Deformation

The responses of *Network A* and *Network B* are described through Maxwell models. In this subsection, we provide the general framework for the formulation of the constitutive equations for Maxwell models. In the Sections 3.3.5 and 3.3.6, we will then specialize our equations for the individual networks.

Kinematics

Consider a Maxwell element K subject to a isochoric deformation gradient $\mathbf{F}_K$ with $\det \mathbf{F}_K = 1$. In the context of finite strain, we assume that the total isochoric deformation gradient can be multiplicatively decomposed into an elastic part $\mathbf{F}_K^e$ and a viscous part $\mathbf{F}_K^v$,

$$\mathbf{F}_K = \mathbf{F}_K^e \mathbf{F}_K^v \tag{3.8}$$

Furthermore, we introduce the total, elastic and viscous rate of isochoric deformation tensors

$$\dot{\mathbf{F}}_K = \mathbf{L}_K \mathbf{F}_K \quad , \quad \dot{\mathbf{F}}_K^e = \mathbf{L}_K^e \mathbf{F}_K^e \quad \text{and} \quad \dot{\mathbf{F}}_K^v = \mathbf{L}_K^v \mathbf{F}_K^v \tag{3.9}$$

with the relationship

$$\mathbf{L}_K = \mathbf{L}_K^e + \mathbf{F}_K^e \mathbf{L}_K^v \mathbf{F}_K^{e-1} \tag{3.10}$$

It is assumed that both the elastic and viscous spins are zero for the deformation of the Maxwell elements. Formally, we write

$$\mathbf{D}_K^e := \mathbf{L}_K^e = \mathbf{L}_K^{eT} \quad \text{and} \quad \mathbf{D}_K^v := \mathbf{L}_K^v = \mathbf{L}_K^{vT} \tag{3.11}$$

Due to the spin-free elastic deformation, the rate of deformation tensor $\mathbf{D}_K^e$ may also be expressed as a function of the time derivative of the right Cauchy-Green tensor

$$\mathbf{D}_K^v = \frac{1}{2} \mathbf{F}_K^{e-T} \dot{\mathbf{C}}_K^e \mathbf{F}_K^{e-1} \tag{3.12}$$

In addition to the tensor description of the kinematics, we make use of the scalar deformation

measure

$$\zeta = \sqrt{\mathrm{tr}\mathbf{C} - 3} \tag{3.13}$$

in our model formulation. The strain-like variable ζ is zero in the undeformed configuration and always positive for deformed configurations.

Thermodynamics and Hyperelasticity

For isothermal conditions, the second law of thermodynamics for each Maxwell element reads

$$J\mathbf{T}_K : \mathbf{L}_K - \dot{\psi}_K \geq 0 \tag{3.14}$$

with the deviatoric Cauchy stress $\mathbf{T}_K$ and the free energy ψ_K (per unit initial volume). We impose the assumption of Green elasticity through the hyperelastic relationship (e.g. Ogden, 1984)

$$\mathbf{T}_K = \frac{2}{J}\mathrm{dev}\left\{\mathbf{F}_K^e \frac{\partial \psi_K}{\partial \mathbf{C}_K^e} \mathbf{F}_K^{eT}\right\} \tag{3.15}$$

where $\mathbf{C}_K^e = \mathbf{F}_K^{eT}\mathbf{F}_K^e$ denotes the right Cauchy-Green tensor of isochoric elastic deformation. Recall that we assume isochoric elastic deformation which implies $\det \mathbf{F}_K^e = 1$ and $\mathrm{tr}\mathbf{D}_K^e = 0$. Using Eq. (3.10) and Eq. (3.15) in Eq. (3.14) yields the thermodynamic constraint

$$J\mathbf{T}_K : \left(\mathbf{F}_K^e \mathbf{L}_K^v \mathbf{F}_K^{e-1}\right) = \left(J\mathbf{F}_K^{eT}\mathbf{T}_K\mathbf{F}_K^{e-T}\right) : \mathbf{D}_K^v \geq 0 \tag{3.16}$$

In the following, the Mandel stress

$$\mathbf{M}_K := J\mathrm{dev}\left\{\mathbf{F}_K^{eT}\mathbf{T}_K\mathbf{F}_K^{eT}\right\} \tag{3.17}$$

is used as the driving stress of viscous deformation while the viscoplastic constitutive equations are written such that

$$\mathbf{M}_K : \mathbf{D}_K^v \geq 0 \tag{3.18}$$

Flow Rule for Viscous Flow

The direction of viscous flow is supposed to be aligned with the direction of the driving Mandel stress. Formally, we write the flow rule

$$\mathbf{M}_K = \eta_K \mathbf{D}_K^v \tag{3.19}$$

with the deformation and rate dependent viscosity $\eta_K \geq 0$. The rate dependent viscosity is defined through the nonlinear relationship $\bar{m}_k = \bar{m}_k\left(\bar{d}_k\right)$ between the equivalent Mandel stress

$$\bar{m}_k = \sqrt{\frac{3}{2}\mathbf{M}_k : \mathbf{M}_k} \tag{3.20}$$

and the equivalent viscous strain rate

$$\bar{d}_k = \sqrt{\frac{3}{2}\mathbf{D}_k^v : \mathbf{D}_k^v} \tag{3.21}$$

Using Eq. (3.20) and Eq. (3.21) in Eq. (3.19), we obtain

$$\eta_K = \frac{2}{3}\frac{\bar{m}_k}{\bar{d}_k} \tag{3.22}$$

3.3.5 Specialization of the Maxwell Model for *Network A*

Network A represents the rubbery response of the soft domain which is modeled through a Maxwell element composed of a nonlinear elastic Gent spring and a nonlinear viscous damper that accounts for the apparent rate dependency of the theoretical equilibrium path.

Gent Elasticity of *Network A*

For isochoric deformation, Gent's (1996) free energy function may be written as

$$\psi_A = -\frac{1}{2}\mu_A J_A \ln\left(1 - \frac{\mathrm{tr}\mathbf{C}_A^e - 3}{J_A}\right) \tag{3.23}$$

with the material parameters $\mu_A > 0$ (initial modulus) and $J_A > 0$ (locking stretch). With this form of free energy, the Cauchy stress $\mathbf{T}_A$ in *Network A* reads:

$$\mathbf{T}_A = \frac{\mu_A}{J}\left(1 - \frac{\mathrm{tr}\mathbf{C}_A^e - 3}{J_A}\right)^{-1} \mathrm{dev}\mathbf{B}_A^e \tag{3.24}$$

where $\mathbf{B}_A^e = \mathbf{F}_A^e \mathbf{F}_A^{eT}$ denotes the right Cauchy-Green tensor of isochoric elastic deformation.

Nonlinear Viscous Response of *Network A*

Figure 3-6a suggests that the viscoelastic contribution to the stress of *Network A* increases monotonically as the deformation increases. Furthermore, the experimental results suggest a power-law relation between the viscosity η_A and the equivalent rate of viscous deformation. Thus, the nonlinear viscous evolution law for *Network A* is written as

$$\bar{m}_A = \frac{3}{2}\eta_A \bar{d}_A = P_A\left(\exp\zeta - 1\right)\left(\frac{\bar{d}_A}{d_{ref}}\right)^{n_A} \tag{3.25}$$

with the reference rate of deformation $d_{ref} = 1/s$, the viscosity constant $P_A > 0$, and the exponent $n_A > 0$ controlling the rate-sensitivity.

3.3.6 Specialization of the Constitutive Equations for *Network B*

Network B represents the response of the hard domain which is modeled through a Maxwell element composed of a linear elastic spring and a nonlinear viscous damper that accounts for the high stiffness at small strain and the rate sensitivity of hysteresis.

Hencky Elasticity of *Network B*

The stiffness of *Network B* governs the stiff macroscopic response of polyurea at small strains. Here, we make use of the isochoric part of Hencky's strain energy function

$$\psi_B = \frac{1}{2}\mu_B\left(\ln \mathbf{U}_B^e\right) : \left(\ln \mathbf{U}_B^e\right) \tag{3.26}$$

where the elastic stretch tensor $\mathbf{U}_B^e$ is found from the polar decomposition of the elastic deformation gradient, $\mathbf{F}_B^e = \mathbf{R}_B^e \mathbf{U}_B^e$ with $\mathbf{R}_B^{eT}\mathbf{R}_B^e = \mathbf{1}$. Upon evaluation, we obtain the deviatoric

part of the Cauchy stress acting on *Network B*

$$T_B = \frac{2\mu_B}{J}\mathbf{R}_B^e \left(\ln \mathbf{U}_B^e\right) \mathbf{R}_B^{eT} \tag{3.27}$$

Nonlinear Viscous Response of *Network B*

Figure 3-7a suggests that the overall viscoelastic response of *Network B* is similar to the linear viscoelastic response of a Maxwell model composed of a linear spring (of Young's modulus E) and a linear viscous damper (of viscosity η). The stress-strain ($\sigma - \varepsilon$) response of a Maxwell model with the linear components at a constant strain rate reads (e.g. Brinson and Brinson, 2008)

$$\sigma = E\tau\dot{\varepsilon}_0 \left[1 - \exp\left(-\frac{\varepsilon}{\tau\dot{\varepsilon}_0}\right)\right] \tag{3.28}$$

where $\tau = \eta/E$ is the relaxation time, and $\dot{\varepsilon}_0$ is the applied constant strain rate. Note that even though the Maxwell model is composed of only linear elements, the stress-strain response is nonlinear at constant strain rates. However, our experiments suggest that the stress-strain response of *Network B* is linear for small strains regardless of strain rate.

Inspired by the results for the one-dimensional Maxwell model with linear components (Eq. (3.28)), we propose a constitutive equation that guarantees a linear elastic response of *Network B* at small strains

$$\bar{m}_B = \sqrt{3}\mu_B Q_B \left(\frac{\bar{d}_B}{d_{ref}}\right)^{n_B} \left\{1 - \exp\left[-\frac{\zeta}{Q_B}\left(\frac{\bar{d}_B}{d_{ref}}\right)^{-n_B}\right]\right\} \tag{3.29}$$

where the dimensionless material constants Q_B and n_B characterize the viscous properties of *Network B*.

3.4 Identification of the Model Parameters

The proposed constitutive model comprises eight material parameters: four parameters (μ_A, J_A, P_A, n_A) for *Network A*, three parameters (μ_B, Q_B, n_B) for *Network B*, and one parameter (κ) describing the elastic volumetric response. The constitutive equations are detailed for uniaxial stress loading in order to identify all material parameters from the monotonic loading and

unloading compression experiments.

3.4.1 Constitutive Equations for Uniaxial Loading

Under uniaxial stress loading, the macroscopic stress tensor takes the form

$$\mathbf{T} = \sigma \mathbf{e}_1 \otimes \mathbf{e}_1 \tag{3.30}$$

where σ is the true stress (macroscopic Cauchy stress) while the macroscopic deformation gradient reads

$$\mathbf{F}_{tot} = \lambda_1 \mathbf{e}_1 \otimes \mathbf{e}_1 + \lambda_2 \left(\mathbf{e}_2 \otimes \mathbf{e}_2 + \mathbf{e}_3 \otimes \mathbf{e}_3\right) \tag{3.31}$$

$$J = \det \mathbf{F}_{tot} = \lambda_1 \left(\lambda_2\right)^2 \tag{3.32}$$

At the network level, the isochoric part of the deformation gradient may be expressed as a function of the stretch λ,

$$\mathbf{F} = \lambda \mathbf{e}_1 \otimes \mathbf{e}_1 + \frac{1}{\sqrt{\lambda}} \left(\mathbf{e}_2 \otimes \mathbf{e}_2 + \mathbf{e}_3 \otimes \mathbf{e}_3\right) \quad \text{with} \quad \lambda = \left(\frac{\lambda_1}{\lambda_2}\right)^{2/3} \tag{3.33}$$

The total stretch of a Maxwell element K can be decomposed further into its elastic part λ_K^e and the viscous part λ_K^v

$$\lambda = \lambda_K^e \lambda_K^v \tag{3.34}$$

Using this notation, the kinematic variables used in our constitutive equations may be expressed as a function of the elastic and viscous stretches and their respective time derivatives

$$\mathrm{tr}\mathbf{C}_K^e = (\lambda_K^e)^2 + \frac{2}{\lambda_K^e} \tag{3.35}$$

$$\mathrm{dev}\mathbf{B}_K^e = \frac{1}{3}\left[(\lambda_K^e)^2 - \frac{1}{\lambda_K^e}\right]\left(2\mathbf{e}_1 \otimes \mathbf{e}_1 - \mathbf{e}_2 \otimes \mathbf{e}_2 - \mathbf{e}_3 \otimes \mathbf{e}_3\right) \tag{3.36}$$

$$\ln \mathbf{U}_K^e = \frac{1}{2}\left(\ln \lambda_K^e\right)\left(2\mathbf{e}_1 \otimes \mathbf{e}_1 - \mathbf{e}_2 \otimes \mathbf{e}_2 - \mathbf{e}_3 \otimes \mathbf{e}_3\right) \tag{3.37}$$

$$\zeta = \sqrt{\lambda^2 + \frac{2}{\lambda} - 3} \tag{3.38}$$

$$\bar{d}_k = \frac{\left|\dot{\lambda}_K^v\right|}{\lambda_K^v} \tag{3.39}$$

The deviatoric stress tensors $\mathbf{T}_K$ acting on the Maxwell elements are written as

$$\mathbf{T}_K = \frac{\sigma_K}{3}\left(2\mathbf{e}_1 \otimes \mathbf{e}_1 - \mathbf{e}_2 \otimes \mathbf{e}_2 - \mathbf{e}_3 \otimes \mathbf{e}_3\right) \tag{3.40}$$

while

$$\sigma = \sigma_A + \sigma_B \tag{3.41}$$

σ_A and σ_B are true stresses acting on *Networks* A and B, respectively.

Using expressions Eq. (3.30) to Eq. (3.41), we obtain the simplified constitutive equations for uniaxial loading:

- Volumetric deformation induced linear elasticity with the model parameter κ

$$\sigma = 3\kappa\frac{\ln J}{J} \tag{3.42}$$

- Gent elasticity of *Network* A with the model parameters J_A and μ_A

$$\sigma_A = \frac{\mu_A}{J}\left[(\lambda_A^e)^2 - \frac{1}{\lambda_A^e}\right]\left\langle 1 - \frac{1}{J_A}\left[(\lambda_A^e)^2 + \frac{2}{\lambda_A^e} - 1\right]\right\rangle^{-1} \tag{3.43}$$

- Nonlinear viscous response of *Network* A with the model parameters P_A and n_A

$$|\sigma_A| = \frac{P_A}{J}\left(\exp\zeta - 1\right)\left(\frac{\bar{d}_A}{d_{ref}}\right)^{n_A} \tag{3.44}$$

- Hencky elasticity of *Network* B with the model parameter μ_B

$$\sigma_B = \frac{3\mu_B}{J}\ln\lambda_B^e \tag{3.45}$$

- Nonlinear viscous response of *Network* B with the model parameters and ,

$$|\sigma_B| = \frac{\sqrt{3}\mu_B Q_B}{J}\left(\frac{\bar{d}_B}{d_{ref}}\right)^{n_B}\left\{1 - \exp\left[-\frac{\zeta}{Q_B}\left(\frac{\bar{d}_B}{d_{ref}}\right)^{-n_B}\right]\right\} \tag{3.46}$$

Table 3.1: Summary of material parameters indentified from monotonic loading/unloading tests under five different strain rates.

Isochoric Part of *Network A*	Rubber Spring	μ_A	$7.00MPa$
		J_A	10.7
	Viscous Damper	P_A	$4.42MPa$
		n_A	0.0646
Isochoric Part of *Network B*	Linear Spring	μ_B	$82.3MPa$
	Viscous Damper	Q_A	0.0447
		n_A	0.0755
Volumetric Part		κ	$829MPa$

3.4.2 Model Calibration

The 1-D calibration process is composed of two steps: the seven parameters (i.e. μ_A, J_A, P_A, n_A, μ_B, Q_B and n_B) relating to isochoric deformation are identified assuming material incompressibility ($J = 1$), before the bulk modulus κ is estimated based on the Lamé moduli and the Poison's ratio. A summary of all identified material parameters is given in Table 1.

Material Parameters of *Network A* (μ_A, J_A, P_A, n_A)

The model is calibrated such that the response of *Network A* describes the rate dependency of the hypothetical equilibrium path in the continuous compression experiments. As discussed in Section 3.3.1 (see also Figure 3-6a), the hypothetical equilibrium path $\sigma_A = \sigma_A\left(\lambda, \bar{d}_A\right)$ for a given strain rate amplitude $\bar{d}_A$ is approximated by the average of the measured loading and unloading stress-strain curves at a total strain rate $\dot{\varepsilon}$

$$\sigma_A\left(\lambda, \bar{d}_A\right) \simeq \frac{1}{2}\left[\sigma_A\left(\lambda, \bar{d}_A\right) + \sigma_A\left(\lambda, -\bar{d}_A\right)\right] \quad \text{with} \quad \bar{d}_A \simeq |\dot{\varepsilon}| \tag{3.47}$$

The material parameters for *Network A* are calibrated in an iterative manner:

1. Assuming $\lambda_A^e(t) \simeq \lambda(t)$, we estimate (μ_A, J_A) from the best fit of Eq. (3.4344) to the experimentally obtained stress-strain curve for the highest strain rate case (here, $|\dot{\varepsilon}| \simeq 10^1/s$).

2. For the remaining strain rates, we calculate $\lambda_A^e(t)$ based on Eq. (3.43) using (μ_A, J_A).

3. Using the relationship $\lambda_A^v(t) = \lambda(t)/\lambda_A^e(t)$, we calculate $|\sigma_A|$ as a function of the strain-like variable ζ for each experiment (Figure 3-6b); in the figure, the curve labels indicate the average effective viscous strain rate $\bar{d}_A$.

4. The parameters P_A and n_A are then obtained from the approximation Eq. (3.44) of the curves shown in Figure 3-6c.

5. It is useful to evaluate the term $\Pi_A := |\sigma_A| / (\exp\zeta - 1)$ from each experimental curve. Π_A is a function of the effective viscous strain rate $\bar{d}_A$ only and independent of the total strain. In other words, each curve shown in Figure 3-6b reduces to a single data point in Figure 3-6c. The subsequent curve fit $\Pi_A = (P_A/J)\left(\bar{d}_A/d_{ref}\right)^{n_A}$ of the data points in Figure 3-6c yields the model parameters P_A and n_A.

After completing Steps 1 to 5, we obtain:

$$\begin{aligned} \mu_A &= 6.85MPa \quad , \quad J_A = 11.0 \\ P_A &= 4.44MPa \quad , \quad n_A = 0.0648 \end{aligned} \tag{3.48}$$

A second calibration loop is performed, starting with $\lambda_A^e(t) = \lambda(t)/\lambda_A^v(t)$ in Step 1, where $\lambda_A^v(t)$ is the viscous deformation predicted by the model parameters Eq. (3.48). Subsequent evaluation yields:

$$\begin{aligned} \mu_A &= 7.00MPa \quad , \quad J_A = 10.7 \\ P_A &= 4.42MPa \quad , \quad n_A = 0.0646 \end{aligned} \tag{3.49}$$

The calibration procedure has been stopped at this point as additional iterations did not improve the accuracy of the curve fit.

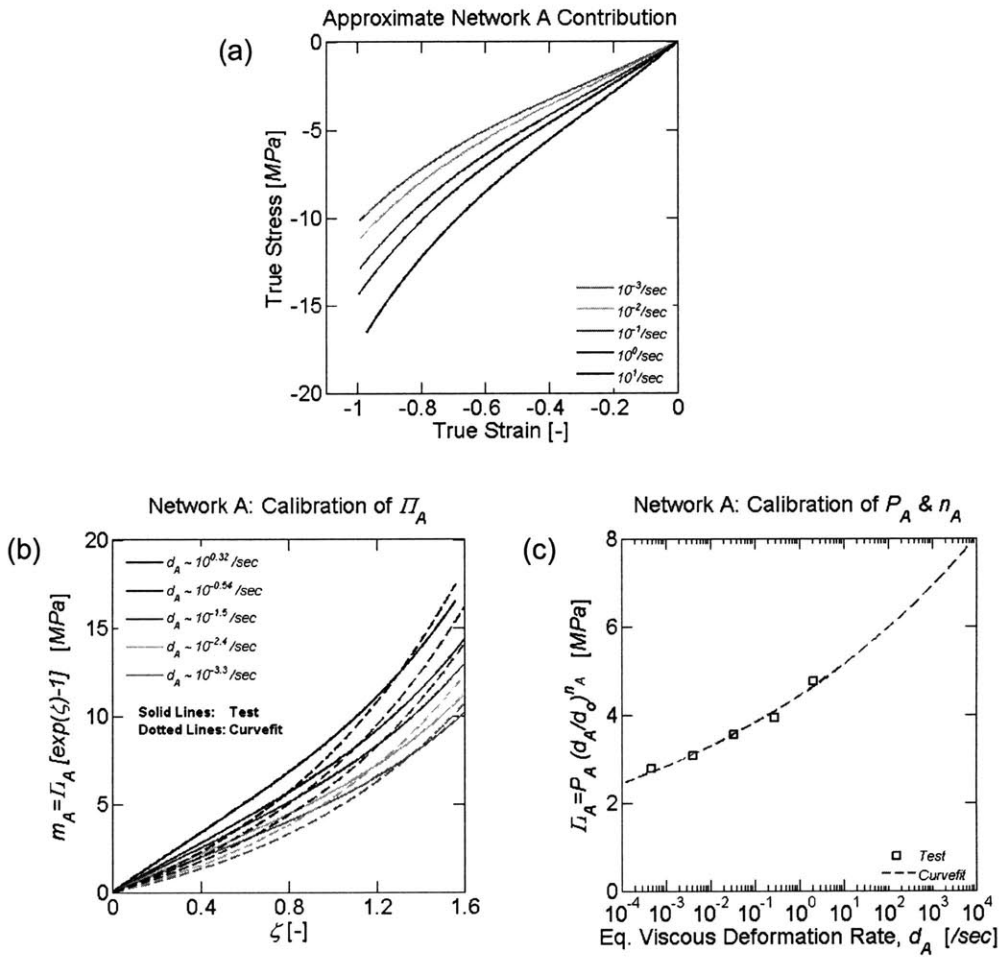

Figure 3-6: Material model parameter identification for *Network A*. (a) Estimated experimental stress-strain curve for *Network A*; (b) Equivalent Mandel stress as a function of the scalar deformation measure ζ; (c) Π_A as function of the equivalent viscous deformation rate $\bar{d}_A$ for the identification of the model parameters P_A and n_A through power-law fit.

Material Parameters of *Network B* (μ_B, Q_B, n_B)

The stress contribution of *Network B* is obtained by subtracting the identified stress contribution of *Network A* (using the parameters Eq. (3.49) in Eq. (3.44)) from the original stress-strain curve for each strain rate

$$\sigma_B(\lambda, \dot{\varepsilon}) = \sigma(\lambda, \dot{\varepsilon}) - \sigma_A(\lambda, \bar{d}_A) \tag{3.50}$$

where $\bar{d}_A$ corresponds to the average viscous strain rates that have been determined throughout the calibration of *Network A*. Figure 3-7 shows the corresponding results for different strain rates. According the proposed rheological model, viscoelastic behavior of *Network B* should be symmetric with respect to the stress, i.e. $\sigma_B(\lambda, -\dot{\varepsilon}) = -\sigma_B(\lambda, \dot{\varepsilon})$. However, the curves in Figure 3-7 illustrate that this symmetry assumption holds only approximately true when using the calibrated analytical expression Eq. (3.44) for *Network A*. In close analogy with the calibration procedure for *Network A*, we identify the model parameters associated with *Network B*:

1. We assume $\lambda_B^e(t) \simeq \lambda(t)$ for the highest strain rate case (i.e. strain rate of $10^1/s$).

2. Determine μ_B from the best curve fit for the experimental stress-strain curve for the loading phase using Eq. (3.45).

3. Using μ_B, we can then calculate $\lambda_B^e(t)$ and $\lambda_B^v(t) = \lambda(t)/\lambda_B^e(t)$ for the other experiments. The corresponding $|\sigma_B|$ versus ζ curves are shown in Figure 3-7b. According to Eq. (3.46), we have
$$|\sigma_B| = \frac{\sqrt{3}\mu_B}{J}\zeta_B\left[1 - \exp\left(-\frac{\zeta}{\zeta_B}\right)\right] \tag{3.51}$$
where $\zeta_B := Q_B\left(\bar{d}_B/d_{ref}\right)^{n_B}$ is a function of the strain rate only. Thus, we determine ζ_B from the approximation of Eq. (3.51) to the $|\sigma_B|$ vs. ζ curves.

4. Subsequently, the material constants Q_B and n_B are found from plotting ζ_B as a function of the effective viscous strain rate $\bar{d}_B$.

A second parameter identification loop is performed using $\lambda_B^e(t) = \lambda(t)/\lambda_B^v(t)$ leading to:

$$\begin{aligned} \mu_B &= 82.3MPa \\ Q_B &= 0.0447 \quad , \quad n_A = 0.0755 \end{aligned} \tag{3.52}$$

Bulk Modulus of Material (κ)

The initial shear modulus for the proposed model is the sum of the shear modulus of each network, i.e., $\mu = \mu_A + \mu_B = 89.3MPa$. Experiments revealed that the Poisson's ratio of $\nu = 0.45$ is nearly rate-independent throughout the deformation up to the strain of 1.0 (Shim and Mohr, 2009a). Since the free energy for the volumetric deformation is based on the linear elastic model, we can determine the bulk modulus using the relation between the elastic moduli

$$\kappa = \frac{2\mu(1+\nu)}{3(1-2\nu)} = 8.29MPa \tag{3.53}$$

3.5 Comparison of Simulation and Experiments

The constitutive model has been programmed as a user material subroutine for the finite element software ABAQUS/Explicit. Using the identified material model parameters, we perform the simulations of all experiments described in Section 3.2.

3.5.1 Continuous Compression

Figure 3-2c summarizes the numerically predicted stress-strain curves for different strain rates. Similarly to the experiments (Figure 3-2b), the simulation results exhibit a high strain rate sensitivity during the loading phases. In addition, the characteristic convergence of the stress-stain curves for different loading velocities is also captured by the simulations. The comparisons of experiment and simulation for individual strain rates are shown in Figures 3-8a to 3-8e. The stress-strain curves show a better agreement during loading than during unloading. The loading portions typically feature the largest error for small strains (less than 0.2) while good predictions are achieved for large strains. The predicted response during unloading is too stiff for all strain rates, i.e. the simulations reach a stress of zero at larger compressive strains than measured in

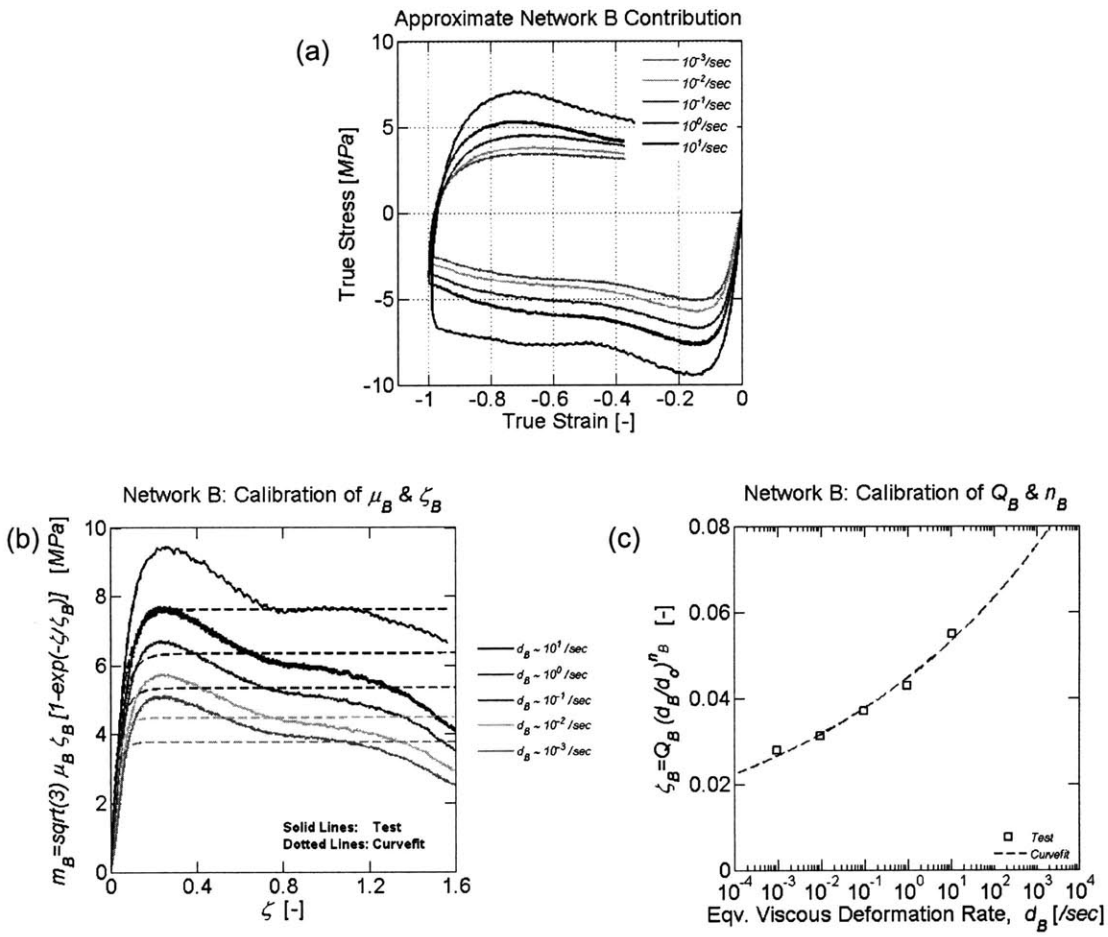

Figure 3-7: Material model parameter identification for *Network B*. (a) Estimated experimental stress-strain curve for *Network B*; (b) Equivalent Mandel stress as a function of the scalar deformation measure ζ; (c) ζ_B as function of the equivalent viscous deformation rate $\bar{d}_B$; identification of the model parameters Q_B and n_B.

the experiments. From an energetic point of view, it is worth noting that the differences during the loading phase underestimate the mechanical work, while the work is overestimated during unloading. However, these two errors compensate each other when calculating the viscous energy dissipation for the entire loading/unloading cycle. In other words, despite small errors in the stress level during loading and unloading, the overall energy dissipation is well predicted over a wide range of strain rates.

The graphs in Figure 3-8 also depict the predicted individual contributions of *Network A* (dotted blue line) and *Network B* (dashed green line). During the model calibration, we assumed that the effective viscous strain rate $\bar{d}_A$ is the same during loading and unloading, which implies that *Network A* exhibits the same stress-strain response during loading and unloading. However, since the total viscous strain λ_A^v keeps on decreasing during unloading (the driving stress for *Network A* is compression during both loading and unloading) even though λ increases, the decrease of the stress level is faster during unloading than the corresponding increase during loading (hysteresis behavior of a Maxwell element). The differences between the loading and unloading portion for *Network A* (blue dashed curves) illustrate this behavior.

The model's symmetric response of *Network B* (the green dashed curves show only the loading portion) is characterized by a plateau over a wide range of strains. Since the elastic strains in *Network B* are small, the driving stress of viscous deformation in *Network B* changes rapidly from compression during loading to tension during unloading. As a result, the effective rate of viscous deformation $\bar{d}_B$ is the same during loading and unloading which is consistent with the assumptions made during calibration. Thus, it is concluded that the differences between the experiments and model predictions are associated with the response of *Network A*.

3.5.2 Stair Compression

Figure 3-3c provides an overview on the simulation results for all loading cases next to the experimentally-measured stress-strain curves from stair compression tests. A direct comparison of the experimental and the simulation results for each loading velocity is shown in Figure 3-9a to 3-9e. Overall, we observe the same model accuracy as for the monotonic loading and unloading experiments, i.e. the model slightly underestimates the stress level for small strains and predicts a faster decrease in stress level after reversal of the loading direction.

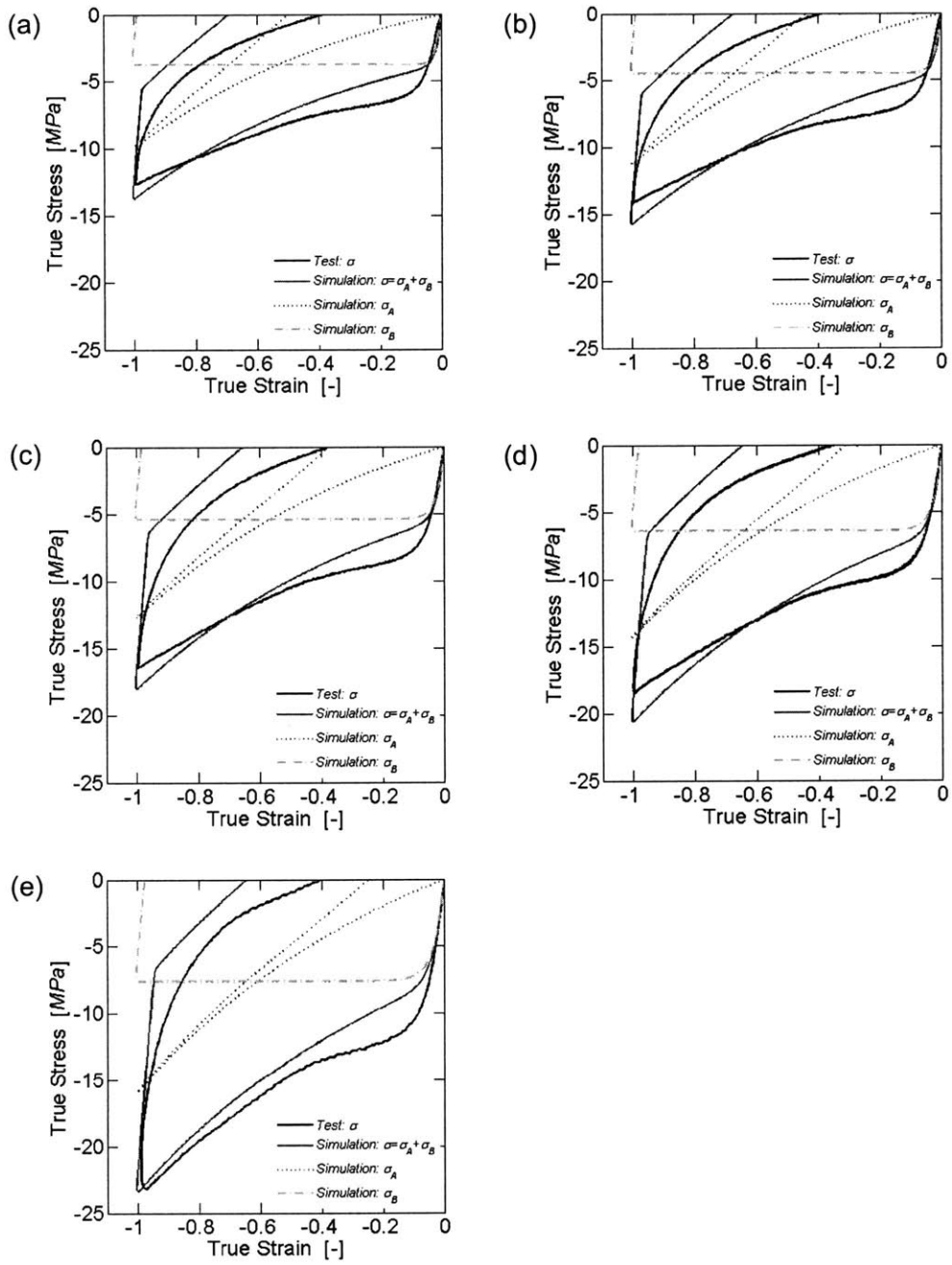

Figure 3-8: Comparison of simulation results and experiments for continuous loading-unloading cycles. (a) $10^{-3}/s$, (b) $10^{-2}/s$, (c) $10^{-1}/s$, (d) $10^{0}/s$ and (e) $10^{1}/s$

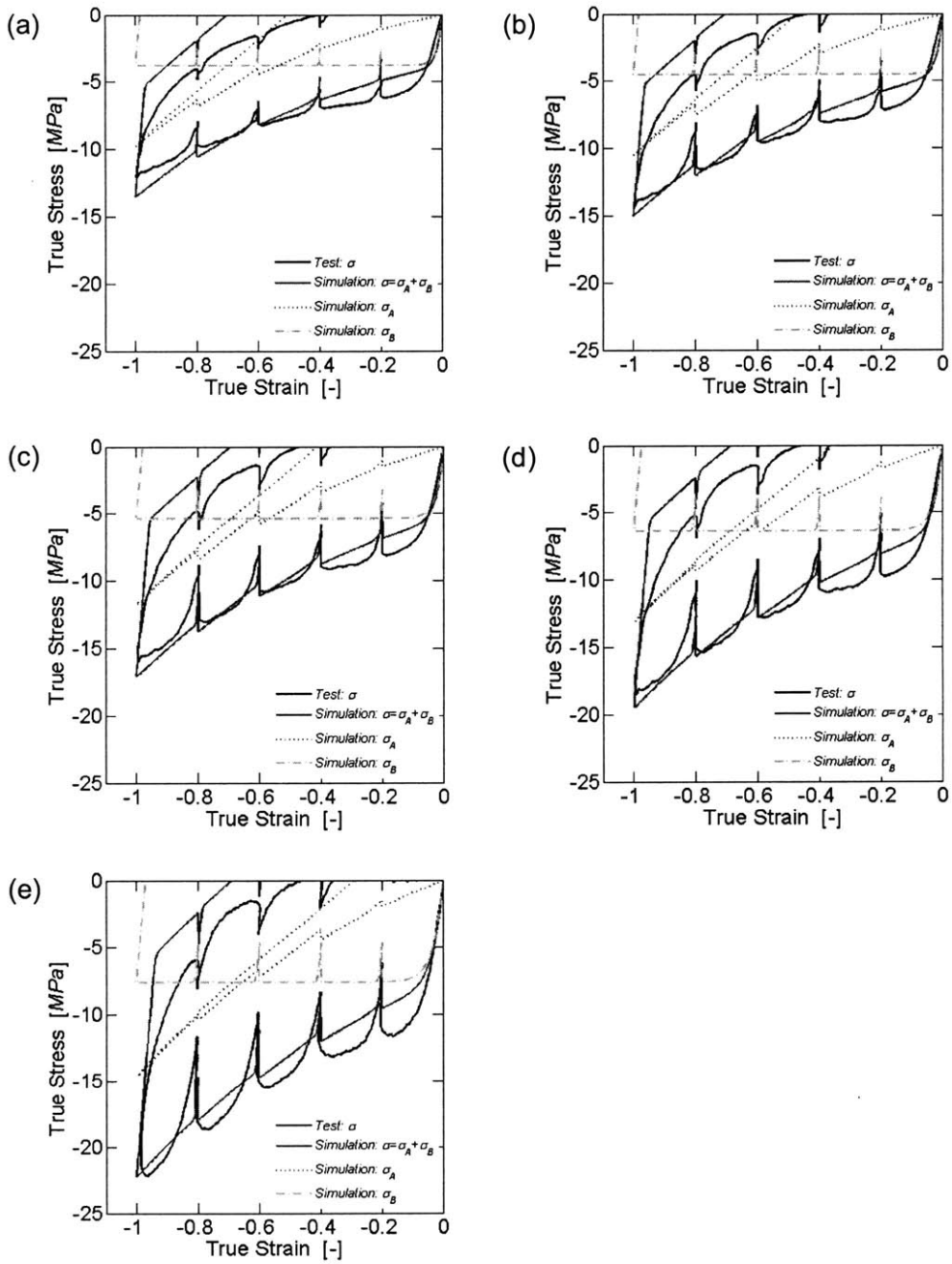

Figure 3-9: Comparison of simulation results and experiments for stain loading/unloading. (a) $10^{-3}/s$, (b) $10^{-2}/s$, (c) $10^{-1}/s$, (d) $10^{0}/s$ and (e) $10^{1}/s$

The relaxation behavior of *Network B* is symmetric for loading and unloading (green dashed lines in Figure 3-9). Conversely, the stress-strain curves for *Network A* (blue dotted lines in Figure 3-9) reveal that stress relaxation is more pronounced during the loading phase, while unloading is mainly elastic. This non-symmetric feature of *Network A* is also visible at the macroscopic level where the model predicts the experimental observation of a faster relaxation during loading than during unloading. The model provides accurate estimates of the relaxation-induced stress decrease (jump) for small strains during the loading phase, while this decrease is underestimated at large strains. This is attributed to the fact that the stress contribution of *Network B* reaches its plateau level at small strains; as a result, the amplitude of stress relaxation within *Network B* is very similar for small and large strains.

3.5.3 Relaxation

Figure 3-1b shows the predicted stress histories for all relaxation experiments. In addition, the histories of the relaxation modulus are presented in Figure 3-1d. The relaxation modulus histories are well predicted for the entire range of strains. However, the comparison of the true stress versus time curves indicates that the model predicts slower stress relaxation than observed in the experiments. Similar conclusions may be drawn from the comparison of the experimental and simulated isochronous stress-strain curves. Observe that the instantaneous stress-strain curves agree well with the test results, while the long-term behavior (e.g. blue curves for $616s$) predicted by the model overestimates the stress level at large strains.

3.5.4 Discussion

The model is able to predict the strain rate dependent loading and relaxation behavior polyurea with reasonable accuracy. Furthermore, the model provides good estimates of the rate dependent viscous dissipation throughout the loading/unloading cycles. In the present rheological framework of two parallel Maxwell elements, the identification of the behavior of *Network A* is important. Here, the response of *Network A* has been defined through the "rate-dependent equilibrium path" concept; the mechanical response of *Network A* is identical throughout compressive loading and compressive unloading. Furthermore, in the particular case of polyurea, this imaginary equilibrium path depends on the absolute value of the total true strain rate. The

response of the calibrated constitutive model illustrates that the assumption of a Maxwell model does not lead to an exact description of the material behavior for both loading and unloading. The hysteresis behavior for loading and unloading at a constant total strain rate is an inherent feature of Maxwell models. Consequently, the rate dependency of the conceptual equilibrium path (which is hysteresis free) cannot be represented accurately by a Maxwell model. An attempt has been made to calibrate the material model parameters using a numerical parameter identification scheme (minimization of the error between the experiments and simulations). In other words, the equilibrium path concept based separation of the contributions of *Network A* and *Network B* has been omitted throughout the material model parameters identification. However, the identified model response was not more satisfactory as improvements on the unloading response could only be obtained at the expense of the quality of the loading curve prediction.

In order to come up with an improved constitutive model, one may consider a different rheological model for *Network A*, but to the best of the authors' knowledge, no thermodynamically consistent model has been published in the open literature that can model the apparent elastic (same loading and unloading curve), but yet strain rate dependent behavior of *Network A*. Thus, alternative modeling approaches need to be explored in the future. One thermodynamically consistent option is the introduction of loading and unloading conditions for viscous evolution. However, more research is needed at the microstructural (i.e. molecular) level to justify such loading and unloading conditions from a mechanism point of view.

3.6 Conclusions

The large strain compression response of polyurea is investigated for strain rates ranging $10^{-3}/s$ from to $10^{1}/s$. Continuous and stair-like loading and unloading experiments are performed in addition to simple relaxation tests. The experimental results reveal that the so-called equilibrium path concept breaks down in the case of polyurea. In contradiction with the definition of the equilibrium path, the identified average stress-strain curves in continuous loading/unloading experiments depend on the rate of loading. Thus, as an alternative to the equilibrium path based rheological models of the Zener type, a new constitutive model is formulated assuming

two parallel Maxwell elements. The finite strain constitutive equations are outlined in detail. Subsequently, the eight material model constants are calibrated to describe the mechanical behavior of polyurea. The model predictions are in good agreement with the experimental results. The characteristic convergence of the unloading paths for different strain rates is successfully captured by the model. Furthermore, the rate dependent viscous dissipation throughout a loading/unloading cycle is described with reasonable accuracy. The predicted unloading behavior is too stiff which is associated with the limitations of the Maxwell model that describes the soft domain of polyurea.

Chapter 4

Validation Application

4.1 Introduction

Polyurea is a highly viscoelastic rubber material that is used for the impact protection of vehicle structures. It is considered for the armor protection and retrofitting of military vehicles that are exposed to the blast loading of improvised explosive devices. The anticipated effect of polyurea coatings on the blast resistance of steel plates is twofold. Firstly, the polyurea can directly absorb a portion of the blast energy as it undergoes large deformations. Secondly, the onset of ductile fracture of a steel plate may be retarded through the use of a polyurea coating, thereby increasing the energy absorption of the steel structure.

As discussed by Xue and Hutchinson (2008), necking occurs under uniaxial tension when the average true stress becomes equal to the overall tangent hardening modulus (Considere criterion). In the case of a coated ductile substrate, a high strain hardening coating material can increase the effective hardening modulus of the bilayer material such that necking is retarded with respect to the Considere strain of the uncoated material. The bifurcation analysis of Guduru et al. (2006) reveals that an added surface layer can increase the resistance of a structural element to fragmentation. Moreover, their results show that the addition of a soft coating with high strain hardening can improve the weight specific energy absorption of the structural element. Xue and Hutchinson (2008) demonstrate that the ratio of the elastomer modulus to the flow strength of the substrate controls the effect of necking retardation. McShane et al. (2008) performed tension and bulge tests on copper/polyurethane bilayers under

static and dynamic conditions. Their experimental measurements indicate that coatings do not provide dynamic performance benefits on an equal mass basis. While the total blast resistance increases, the weight specific energy absorption of the structure may actually decrease through the application of a polymer coating. Dynamic ring expansion experiments have been performed by Zhang et al. (2009) on polyurea coated aluminum $6061 - O$ and copper 101 at very high strain rates $(4000 - 15000/s)$. Their experimental results show that there is no significant effect of the polyurea coating on the strain at the onset of localization.

It appears that the neck retardation effect in coated ductile substrates is difficult to achieve when using polyurea in combination with typical engineering materials. However, as pointed out by McShane et al. (2008), polyurea coatings may still be seen as a practical solution for enhancing the blast resistance of metallic structures because of the ease of applying polyurea on existing structures (retrofitting). Even though the performance of the steel substrate may remain unaffected, a very thick polyurea layer can still increase the energy absorption in absolute terms. The impulsive loading experiments of Amini et al. (2009a) reveal that polyurea coatings have a strong effect on the energy transfer to the steel plate. In particular, they demonstrate that the positioning of polyurea on the impact side promotes failure of the steel plate under shock loading while a polyurea layer on the back of the plate attenuates the shock. In the present paper, we deal with the prediction of the large deformation behavior of polyurea in structural applications. Xue and Hutchinson (2008) made use of a Mooney-Rivlin model for the polymer coating in their numerical analysis of the polymer/metal bilayers. Zhang et al. (2009) modeled the behavior of polyurea using a nonlinear hyperelastic material model. However, both uniaxial compression and tension tests have demonstrated that the mechanical response of polyurea is highly strain-rate dependent (e.g. Amirkhizi et al., 2006, Roland et al., 2007, Sarva et al., 2007, Shim and Mohr, 2009a). Amini et al. (2009b) make use of the temperature-, rate- and pressure-sensitive constitutive model by Amirkhizi et al. (2006) to provide supporting simulation results of their direct pressure pulse experiments.

Finite viscoelasticity models of elastomers may be formulated using the so-called hereditary integral approach (Coleman and Noll, 1961, Bernstein et al., 1963, Lianis, 1963, McGuirt and Lianis, 1970, Leonov, 1976, Johnson et al., 1994, Haupt and Lion, 2002, Amirkhizi et al., 2006) but their validity is often limited to a narrow range of strain rates (Yang et al., 2000, Shim et al.,

2004, Hoo Fatt and Ouyang, 2007). As an alternative to the hereditary integral approach, the framework of multiplicative decomposition of the deformation gradient (Kröner, 1960 and Lee, 1969) is frequently used in finite viscoelasticity (e.g. Sidoroff, 1974, Lubliner, 1985, Le Tallec et al., 1993, Reese and Govindjee, 1998, Huber and Tsakmakis, 2000). In that framework, the nonlinear viscoelasticity of elastomers is commonly described through a rheological spring-dashpot models of the Zener type (e.g. Roland, 1989, Johnson et al., 1995, Bergström and Boyce, 1998, Huber and Tsakmakis, 2000, Quintavalla and Johnson, 2004, Bergström and Hilbert, 2005, Qi and Boyce, 2005, Areias and Matous, 2008, Hoo Fatt and Ouyang, 2008, Tomita et al., 2008).

In the present work, we present the time integration scheme for a newly developed rate-dependent constitutive model for polyurea (Shim and Mohr, 2009b). After implementing the model as a user material subroutine into a commercial finite element software, the model is used to predict the mechanical response of thick polyurea layers under punch loading. Experiments are performed on 10mm thick polyurea layers for different punch velocities and different hemispherical punch radii. It is found that the model provides an accurate description of the loading phase, which validates the assumptions made with respect to strain-rate and pressure sensitivity. However, the predicted response deviates from the experimental result during unloading which is discussed in detail.

4.2 Punch Experiments

4.2.1 Specimens

The polyurea specimens used in the study are extracted from a steel armor plate with a $12.7mm$ thick layer of polyurea DragonShield-HT Explosive Resistant Coating (ERC). Rectangular samples of $46 \times 40mm$ are cut from the coated armor plate using conventional machining. The coated polyurea is not separated from the steel as the steel serves as specimen support throughout the punching experiments. However, to guarantee a uniform layer thickness for all specimens, the outer surface of the polyurea is machined down to a final polyurea thickness of $10mm$. All experiments are performed on polyurea in its virgin state (no prior loading) after a shelf life of about four years.

4.2.2 Experimental Procedure

The specimens are clamped on the table of a hydraulic testing machine (Model 8080, Instron). The specimens are loaded through hemispherical indenters that are attached to the moving actuator of the upper crosshead. Two hemispherical indenters of different size are employed: $D = 12.7mm$ and $D = 44.45mm$ (see Figures 4-1a and 4-1b). In addition, we consider two different types of lateral boundary conditions: (1) free in all lateral directions, and (2) constrained in the width direction (Figures 4-1c and 4-1d). For the latter case, the polyurea specimen is placed between two steel blocks which prevents bulging in the width direction, but does not prevent possible shrinking of the specimen in width direction. The friction at the interface between the indenters and the polyurea is reduced by grease and multiple $0.1mm$ thick Teflon layers (which are partially torn apart during the test). The experiments are performed under displacement control at constant deceleration using the control software MAX (Instron, Canton). Starting with an initial velocity v_0, the velocity-time profile decreases linearly until the experiment is stopped at a velocity of $-v_0$ (Figure 4-2). The initial position of the actuator is chosen such that the loading direction is reversed (point $v_0 = 0$) when the punch depth reaches $7mm$. Experiments are performed for $v_0 = 1mm/s$ and $v_0 = 100mm/s$. Throughout all experiments, the punch force is measured using a $50kN$ load cell. The punch displacement is measured using an LVDT that is integrated in the actuator. The overall stiffness of the testing frame of about $100kN/mm$ has obtained from the comparison of the LVDT readout with optical displacement measurements (Shim and Mohr, 2009a). All displacements reported in the following have been corrected by the deformation associated with the finite machine stiffness.

4.2.3 Experimental Results

Figure 4-3a summarizes the results for the experiments with the small hemispherical indenter ($D = 12.7mm$). The measured force-displacement curves are monotonically increasing up to the point of load reversal. During unloading, the force reaches zero at a displacement of about $3.2mm$. Beyond that point, the punch moves faster than the surface of the creeping polyurea specimen. The force level is about 40% higher in a punch test at $v_0 = 100mm/s$ than that at $v_0 = 1mm/s$ which is mostly due to the rate dependent material behavior. Note that the

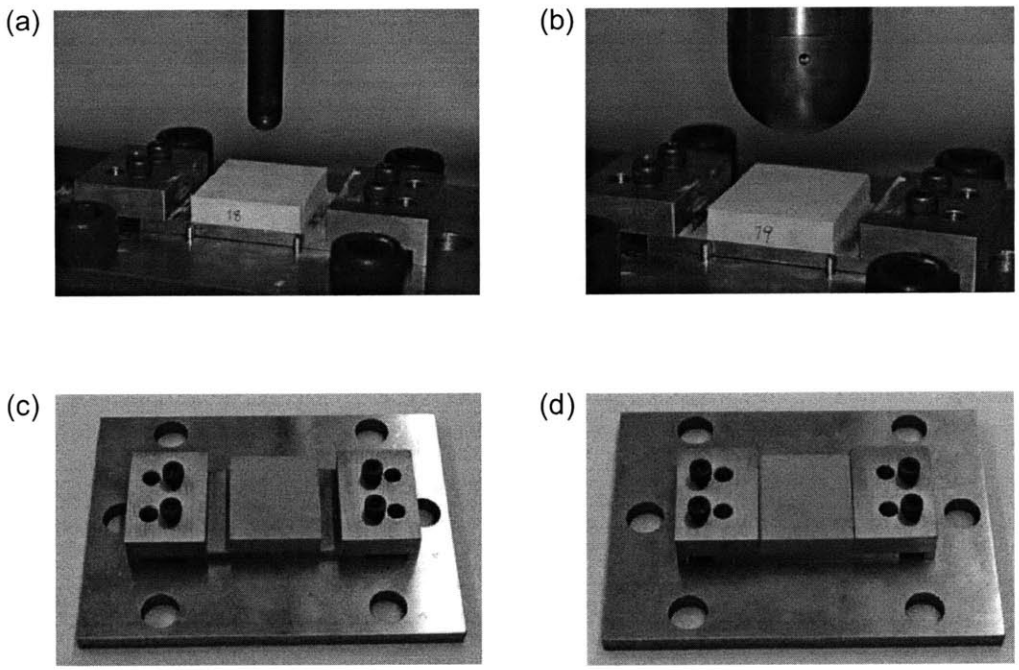

Figure 4-1: Photos of the experiments with (a) the small punch and (b) the large punch. The second row shows the set up for (c) free boundaries in all lateral directions and (d) for constrained boundary conditions in the width direction.

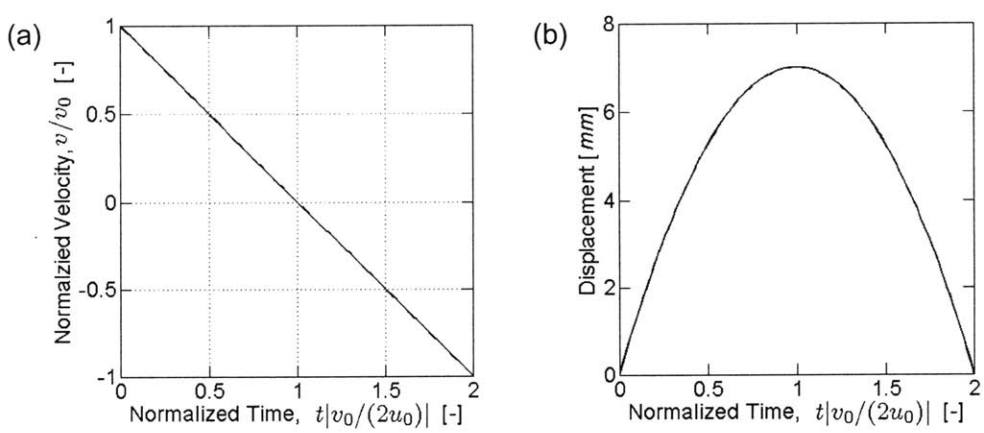

Figure 4-2: Applied loading profiles: (a) Applied velocity history; the velocity axis is normalized by the applied initial velocity of either $v_0 = 1mm/s$ or $100m/s$; the time axis is normalized by $|2u_0/v_0|$ with $u_0 = 7mm$; (b) Corresponding applied displacement history.

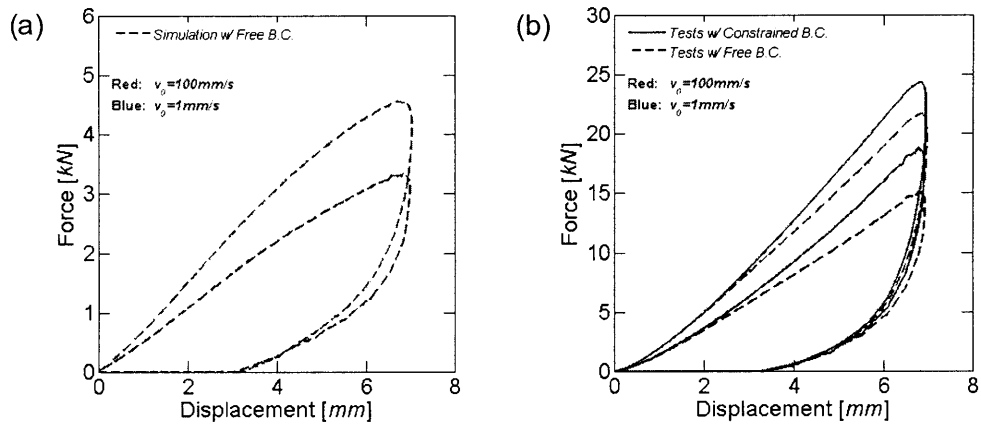

Figure 4-3: Measured load-displacement curves for experiments with (a) the small punch, (b) the large punch.

loading conditions are of quasi-static nature since the speed of elastic waves is polyurea (of the order of $10^6 mm/s$) is much faster than the loading velocities. It is interesting to observe the convergence of the force-displacement curves for both velocities upon unloading which is consistent with the results from uniaxial compression experiments (Shim and Mohr, 2009b). The results with and without constraint in the width direction are almost identical. Thus, Figure 4-3a presents the results for free lateral boundary conditions only.

In close analogy with the results from the small punch, the measured force-displacement curves for the large hemispherical punch experiments are loading velocity sensitive and show a higher force level for the high loading velocity (Figure 4-3b). Moreover, the large punch experiments also show the characteristic convergence of the force-displacement curves during unloading. For the large punch, the force level is zero at a punch displacement of $3.4mm$. The effect of the boundary condition in width direction becomes apparent when using the large hemispherical punch ($D = 44.45mm$); the force level with the constraint (solid lines) is higher than that with the free lateral boundary conditions (dotted lines). Regardless of the applied velocity profiles, the constraint in the width direction increases the force level by about $3kN$ at the maximum punching depth. Subtracting the force level with $v_0 = 1mm/s$ from the force level from $v_0 = 100mm/s$ for the corresponding displacement magnitude, one can find that the

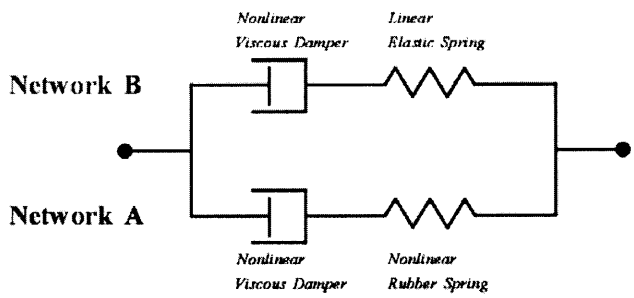

Figure 4-4: Rheological model of the rate dependent constitutive model for polyurea.

effect strain rate during loading phase results in the increase of force level up to $7kN$ about at the punching depth of $7mm$.

4.3 Constitutive Model

In the following, we present the algorithmic version of a recently-developed constitutive model for polyurea. The reader is referred to Shim and Mohr (2009b) for details on the differential formulation and the underlying physical arguments for specific constitutive equations. The algorithm is implemented as a user material subroutine for the finite element software Abaqus/explicit. The constitutive equations are based on a rheological model of two Maxwell elements that act in parallel (Figure 4-4). The first Maxwell element represents the soft part ($Network\ A$) of polyurea and is composed of a nonlinear viscous damper and a nonlinear Gent spring. The hard part ($Network\ B$) is represented by another nonlinear viscous damper and a Hencky spring. The equations are cast in a framework of finite strains with multiplicative Kröner-Lee decomposition (Kröner, 1960, and Lee, 1969) of the deformation gradient for each Maxwell element. The specific evolution laws for individual model components are given in algorithmic form below. The Euler forward numerical integration method is employed within the subroutine for the effectiveness of the implementation, because of numerical challenges associated with Euler backward integration schemes for Maxwell model with nonlinear rubber spring and nonlinear dashpot (e.g. Areias and Matous, 2008).

The material model comprises the viscous deformation gradients of $Networks\ A$ and B, $\mathbf{F}^v_A$

and $\mathbf{F}_B^v$, as internal state variables. We consider the strain driven time integration problem, where the variables at time $\tau = t + \Delta t$ are calculated based on the solution at time t. In other words, given the total deformation gradient $\mathbf{F}_{tot}(\tau)$ and the internal state variables $\mathbf{F}_A^v(t)$ and $\mathbf{F}_B^v(t)$, we evaluate the total Cauchy stress $\mathbf{T}(\tau)$ along with the updated state variables $\mathbf{F}_A^v(\tau)$ and $\mathbf{F}_B^v(\tau)$. The hydrostatic part of the Cauchy stress tensor is directly related to the change in total volume,

$$J(\tau) = \det \mathbf{F}_{tot}(\tau) \tag{4.1}$$

$$\frac{\mathrm{tr}\mathbf{T}(\tau)}{3} = \kappa \frac{\ln J(\tau)}{J(\tau)} \tag{4.2}$$

where κ denoting the bulk modulus. The deviatoric part of the macroscopic stress tensor corresponds to the sum of the deviatoric stresses $\mathbf{T}_A$ and $\mathbf{T}_B$ acting on *Network A* and *Network B*, respectively,

$$\begin{aligned} \mathbf{T}(\tau) &= \mathrm{dev}\mathbf{T}(\tau) + \frac{\mathrm{tr}\mathbf{T}(\tau)}{3}\mathbf{1} \\ &= \mathbf{T}_A(\tau) + \mathbf{T}_B(\tau) + \frac{\mathrm{tr}\mathbf{T}(\tau)}{3}\mathbf{1} \end{aligned} \tag{4.3}$$

For the evaluation of the stresses and internal variables in *Networks A* and *B*, it is useful to define the isochoric deformation gradient

$$\mathbf{F}(\tau) = [J(\tau)]^{-1/3}\mathbf{F}_{tot}(\tau) \tag{4.4}$$

as well as the strain-like deformation measure

$$\zeta(\tau) = \sqrt{\mathrm{tr}\{\mathbf{F}^T(\tau)\mathbf{F}(\tau)\} - 3} \tag{4.5}$$

4.3.1 Response of *Network A*

The viscous gradient is calculated from the Euler forward form

$$\mathbf{F}_A^v(\tau) = [\mathbf{1} + \Delta t\, \mathbf{D}_A^v(t)]\,\mathbf{F}_A^v(t) \tag{4.6}$$

where $\mathbf{D}_A^v(t)$ is the rate of viscous deformation at time t. Subsequently, we have the isochoric deformation gradient of elastic deformation in *Network A*

$$\mathbf{F}_A^e(\tau) = \mathbf{F}_A(t)\left[\mathbf{F}_A^v(t)\right]^{-1} \tag{4.7}$$

Using $\mathbf{F}_A^e(\tau)$, we determine the deviatoric Cauchy stress for *Network A* based on Gent's (1996) free energy function

$$\mathbf{T}_A(\tau) = \frac{\mu_A}{J(\tau)}\left(1 - \frac{\operatorname{tr}\left\{\mathbf{F}_A^{eT}(\tau)\,\mathbf{F}_A^e(\tau)\right\} - 3}{J_A}\right)^{-1} \operatorname{dev}\left\{\mathbf{F}_A^e(\tau)\,\mathbf{F}_A^{eT}(\tau)\right\} \tag{4.8}$$

with the material parameters $\mu_A > 0$ (initial modulus) and $J_A > 0$ (locking stretch).

The viscous rate of deformation tensor $\mathbf{D}_A^v(\tau)$ is obtained from the nonlinear viscous evolution law. For this, we calculate the driving Mandel stress

$$\mathbf{M}_A(\tau) = J(\tau)\operatorname{dev}\left\{\mathbf{F}_A^{eT}(\tau)\,\mathbf{T}_A(\tau)\,\mathbf{F}_A^{e-T}(\tau)\right\} \tag{4.9}$$

along with the corresponding equivalent stress

$$\bar{m}_A(\tau) = \sqrt{\frac{3}{2}\mathbf{M}_A(\tau) : \mathbf{M}_A(\tau)} \tag{4.10}$$

The equivalent rate of viscous deformation $\bar{d}_A(\tau)$ is then given by the power-law

$$\bar{d}_A(\tau) = d_{ref}\left\langle \frac{\bar{m}_A(\tau)}{P_A\left[\exp\zeta(\tau) - 1\right]}\right\rangle^{1/n_A} \tag{4.11}$$

with the reference rate of deformation $d_{ref} = 1/s$ and the material properties $P_A > 0$ (viscosity constant) and the exponent $n_A > 0$ (constant for rate sensitivity). The flow rule assumes that the rate of viscous deformation tensor $\mathbf{D}_A^v$ is aligned with the driving Mandel stress $\mathbf{M}_A$

$$\mathbf{D}_A^v(\tau) = \frac{3}{2}\frac{\bar{d}_A(\tau)}{\bar{m}_A(\tau)}\mathbf{M}_A(\tau)$$

4.3.2 Response of *Network B*

In close analogy with the procedure for *Network A*, the constitutive equations for *Network B* are solved numerically. We have

$$\mathbf{F}_B^v(\tau) = [\mathbf{1} + \Delta t\, \mathbf{D}_B^v(t)]\, \mathbf{F}_B^v(t) \tag{4.12}$$

and

$$\mathbf{F}_B^e(\tau) = \mathbf{F}_B(t)\, [\mathbf{F}_B^v(t)]^{-1} \tag{4.13}$$

The stiff elastic response of *Network B* is described by Hencky's strain energy function. Thus, elastic right stretch tensor $\mathbf{U}_B^e(\tau)$ and the rotation tensor $\mathbf{R}_B^e(\tau)$ are calculated from the polar decomposition of the elastic deformation gradient,

$$\mathbf{F}_B^e(\tau) = \mathbf{R}_B^e(\tau)\, \mathbf{U}_B^e(\tau) \quad \text{with} \quad \mathbf{R}_B^{eT}(\tau)\, \mathbf{R}_B^e(\tau) = \mathbf{1} \tag{4.14}$$

before calculating the deviatoric Cauchy stress

$$\mathbf{T}_B(\tau) = \frac{2\mu_B}{J(\tau)} \mathbf{R}_B^e(\tau)\, [\ln \mathbf{U}_B^e(\tau)]\, \mathbf{R}_B^{eT}(\tau) \tag{4.15}$$

with the shear modulus μ_B.

Subsequently, we write

$$\mathbf{M}_B(\tau) = J(\tau)\, \mathrm{dev}\left\{\mathbf{F}_B^{eT}(\tau)\, \mathbf{T}_B(\tau)\, \mathbf{F}_B^{e-T}(\tau)\right\} \tag{4.16}$$

$$\bar{m}_B(\tau) = \sqrt{\frac{3}{2}\mathbf{M}_B(\tau) : \mathbf{M}_B(\tau)} \tag{4.17}$$

The rate of viscous deformation is approximated by

$$\bar{d}_B(\tau) = d_{ref} \left\langle \frac{\bar{m}_B(\tau)}{\sqrt{3}\mu_B Q_B} \left\{1 - \exp\left[-\frac{\zeta(\tau)}{Q_B}\left(\frac{\bar{d}_B(t)}{d_{ref}}\right)^{-n_B}\right]\right\}^{-1}\right\rangle^{1/n_B} \tag{4.18}$$

where Q_B and n_B are material model parameters that control the rate sensitivity of *Network B*. As for *Network A*, the rate of viscous deformation tensor $\mathbf{D}_B^v$ is aligned with the driving Mandel

Table 4.1: Summary of material parameters indentified from monotonic loading/unloading tests under five different strain rates.

Isochoric Part of *Network A*	Rubber Spring	μ_A	$7.00MPa$
		J_A	10.7
	Viscous Damper	P_A	$4.42MPa$
		n_A	0.0646
Isochoric Part of *Network B*	Linear Spring	μ_B	$82.3MPa$
	Viscous Damper	Q_A	0.0447
		n_A	0.0755
Volumetric Part		κ	$829MPa$

stress $\mathbf{M}_B$

$$\mathbf{D}_B^v(\tau) = \frac{3}{2}\frac{\bar{d}_B(\tau)}{\bar{m}_B(\tau)}\mathbf{M}_B(\tau) \tag{4.19}$$

4.3.3 Model Parameter Identification

The constitutive model requires the identification of eight material parameters: four parameters (μ_A, J_A, P_A, n_A) for *Network A*, three parameters (μ_B, Q_A, n_A) for *Network B*, and one parameter (κ) describing the elastic volumetric response. All model parameters have been identified based on the results from uniaxial compression experiments at five different strain rates between $10^{-3}/s$ and $10^1/s$ up to a true strain of -1.0. Details on the parameter identification procedure are given in Shim and Mohr (2009b). Table 4.1 summarizes the identified material parameters which are used in the present structural validation study. The comparison of the measured and predicted stress-strain curves for uniaxial compression is shown in Figure 4-5. It is noted that the present choice of material model parameters provides a good description of the initial monotonic loading response of polyurea, while the model predictions are systematically too stiff during unloading.

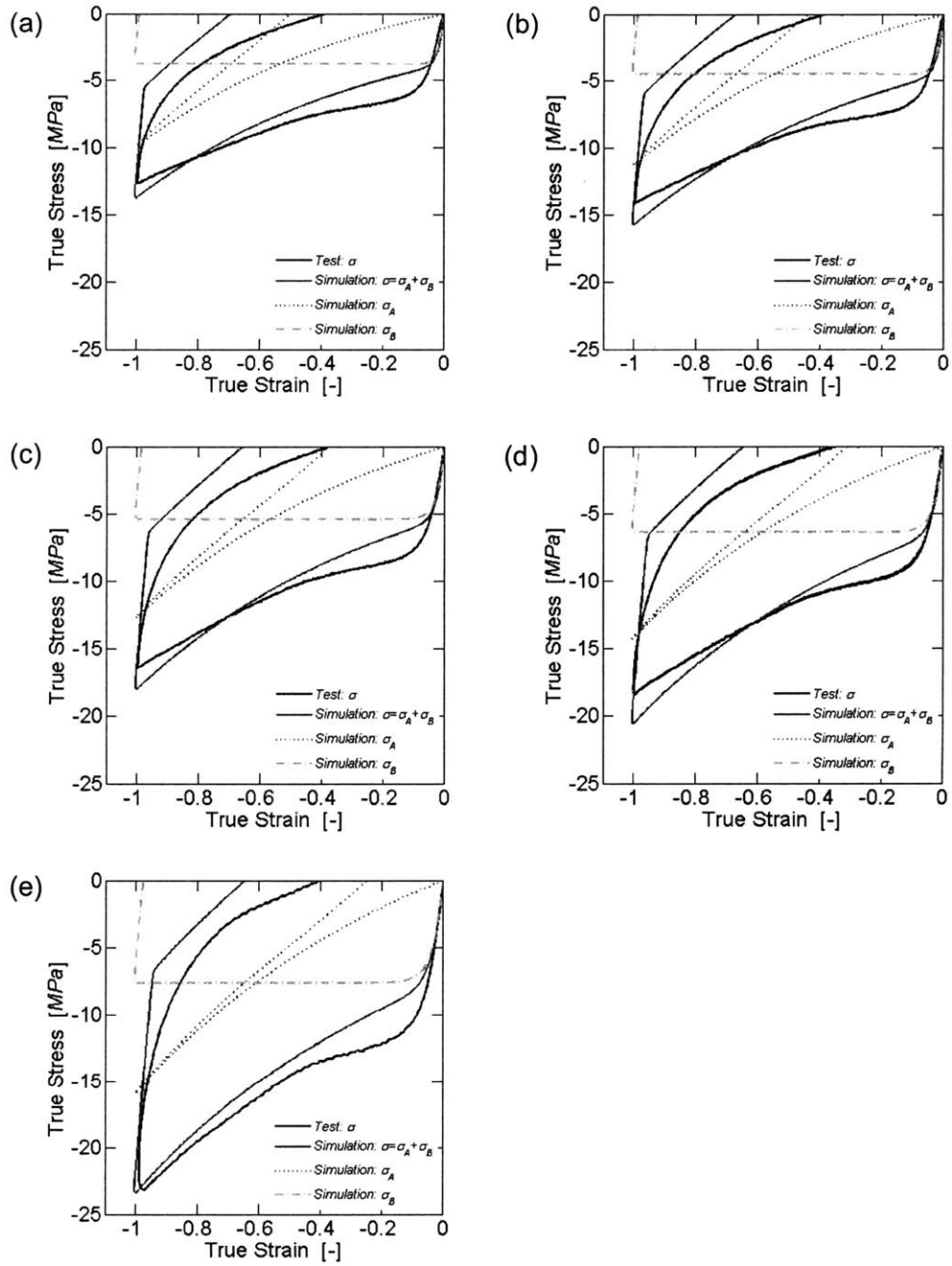

Figure 4-5: Comparison of simulation results and experiments for continuous loading-unloading cycles. (a) $10^{-3}/s$, (b) $10^{-2}/s$, (c) $10^{-1}/s$, (d) $10^{0}/s$, (e) $10^{1}/s$.

4.4 Numerical Simulations of the Punch Experiments

Finite element simulations are performed of all punch experiments. We make use of the symmetry of the mechanical system by using a quarter model. The polyurea block is meshed with eight-node reduced integration solid elements (type C3D8R of the Abaqus element library) while using the user material option to describe the constitutive behavior. The punches are modeled using rigid elements. The meshes comprise eight elements in thickness direction and a small bias in the horizontal plane providing a smaller element size near the center than at the specimen boundaries. Frictionless interface conditions are assumed between the punch and the polyurea. The motion of all nodes at the bottom of the polyurea (which corresponds to the interface with the steel substrate in the experiment) is set to zero. We applied the same punch velocity histories as in the experiments and omitted addition of bulk viscosity.

The deformed meshes at the point of maximum penetration ($u_0 = 7mm$) are shown in Figure 4-6 for the simulation without lateral constraint along the width direction. The comparison of Figures 4-6a and 4-6b clearly shows that the bulging effect, i.e. the lateral expansion of the polyurea block is more pronounced for the large than for the small punch. In the latter case, we observe a small lateral displacement of about $0.5mm$. The bulging has little effect in the load-displacement curves for the small punch and we found nearly the same force-displacement curve for free and constrained lateral boundary conditions.

The predicted force-displacement curves for the small punch are shown in Figure 4-7a. The simulations results are in good agreement with the measured force-displacement curves during the loading phase. A similar conclusion may be drawn from comparing the simulations and experiments for the large punch (Figure 4-7b and 4-7c). The comparison shows that the numerical model can predict (a) the effect of the punch size, (b) the effect of the lateral boundary constraint, and (c) the effect of loading velocity on the force-displacement curve during loading. Figure 4-8 shows the histories of the strain-like variable, ζ, and the viscous rates, $\bar{d}_A$ and $\bar{d}_B$, for the simulation of a small punch with $v_0 = 100mm/s$ (the corresponding locations are highlighted in Figure 4-6a). The profiles elucidate the strong variations in local strain rate during the punch experiments. It is interesting to see that the local viscous rate can be as high as $30/s$ which is close to the strain rate of the fastest calibration experiment (Figure 4-5e). However, unlike for the calibration experiments, the strain rates are non-constant throughout

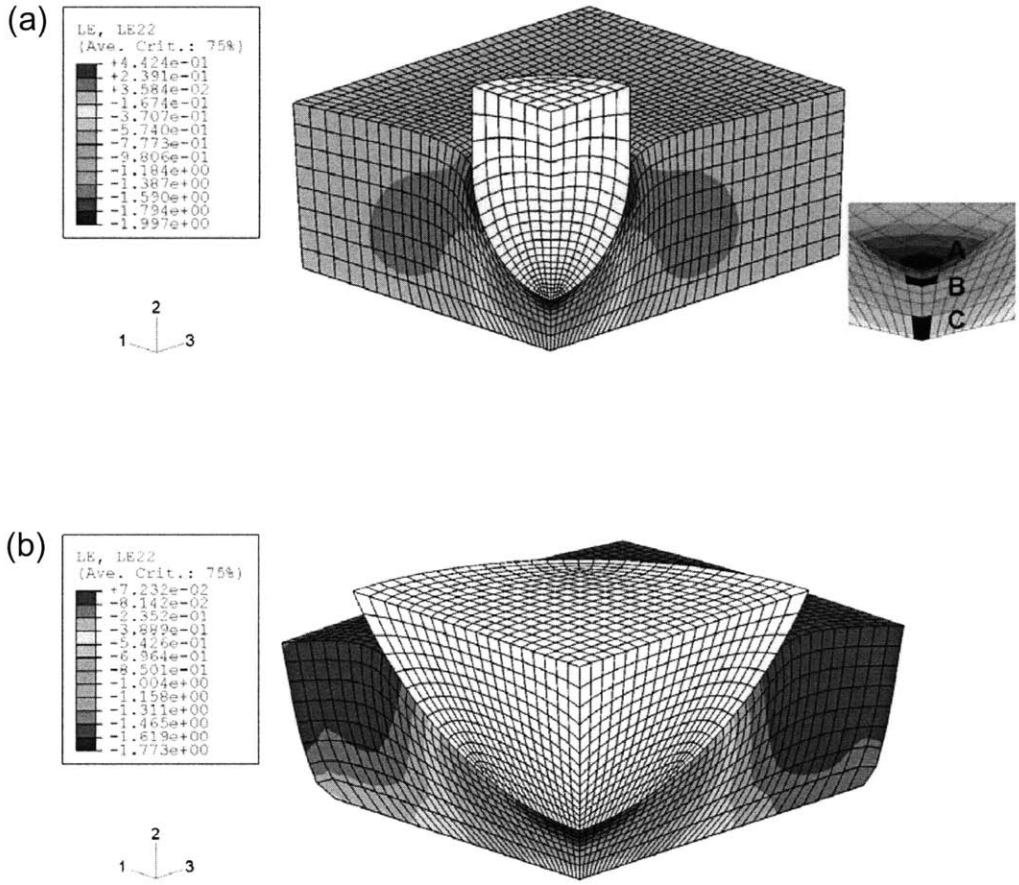

Figure 4-6: The contour plots of the logarithmic strain in thickness-direction from simulations with $v_0 = 100m/s$ at an indentation depth of $7mm$: (a) small hemispherical indenter, and (b) large hemispherical indenter. The detail in Figure 4-6a shows the locations for which the strain rates $\bar{d}_A$ and $\bar{d}_B$ are plotted in Figure 4-8.

a punch tests which is seen as an important validation of the model assumptions with respect to the effect of strain rate. At a punching depth of $7mm$, the simulation results overestimate the force level by about $0.5kN$ in the case of the small punch and $2.5kN$ in the case of the large punch. This overestimation (which corresponds to less than 10% of the current force level) is consistent with the model calibration results. Recall from Figure 4-5 that the model systematically overestimates the stress level at very large compressive strains.

The model predictions during unloading deviate from the experimentally-measured force-displacement responses. The simulations predict the characteristic convergence of the load-displacement curves, but the predicted response during unloading is too stiff for both velocities and both punch sizes. Consequently, the instantaneous residual displacement at zero force is overestimated in the simulations. This deviation is again consistent with the calibration experiments, indicating an inherent shortcoming of the model formulation for unloading.

4.5 Discussion on Unloading Behavior of Polyurea

The loading response of the model agrees well with the test results except for an overestimation of the force at large punch displacements. The simulation results indicate that the material is subject to strains of up to -2.0 as the punching depth reaches $7mm$ (see Figure 4-6). Since this is twice as high as in the experiments for the material model parameter identification, we performed additional material tests at a strain rate of $10^{-2}/s$. Figure 4-9a shows the resulting stress-strain curve from three different experiments. Each virgin-state specimen is subject to a single loading-unloading cycle up to a maximum strain of -0.5, -1.0 and -1.5, respectively. The corresponding simulations (Figure 4-9b) reveal that the numerically-predicted locking behavior is more severe than that observed in the experiments.

The unloading path in the stress-strain curves comprises two characteristic regimes: a stiff part at the beginning of unloading followed by a soft part as the stress approaches zero. Both the experiments and the numerical simulations exhibit this feature. The numerical model does not show the smooth transition between these two regimes, but this is seen as an acceptable engineering approximation of the physical behavior. However, the apparent main deficiency of the current model is its inability to capture the increase of the hysteresis loop width as the strain

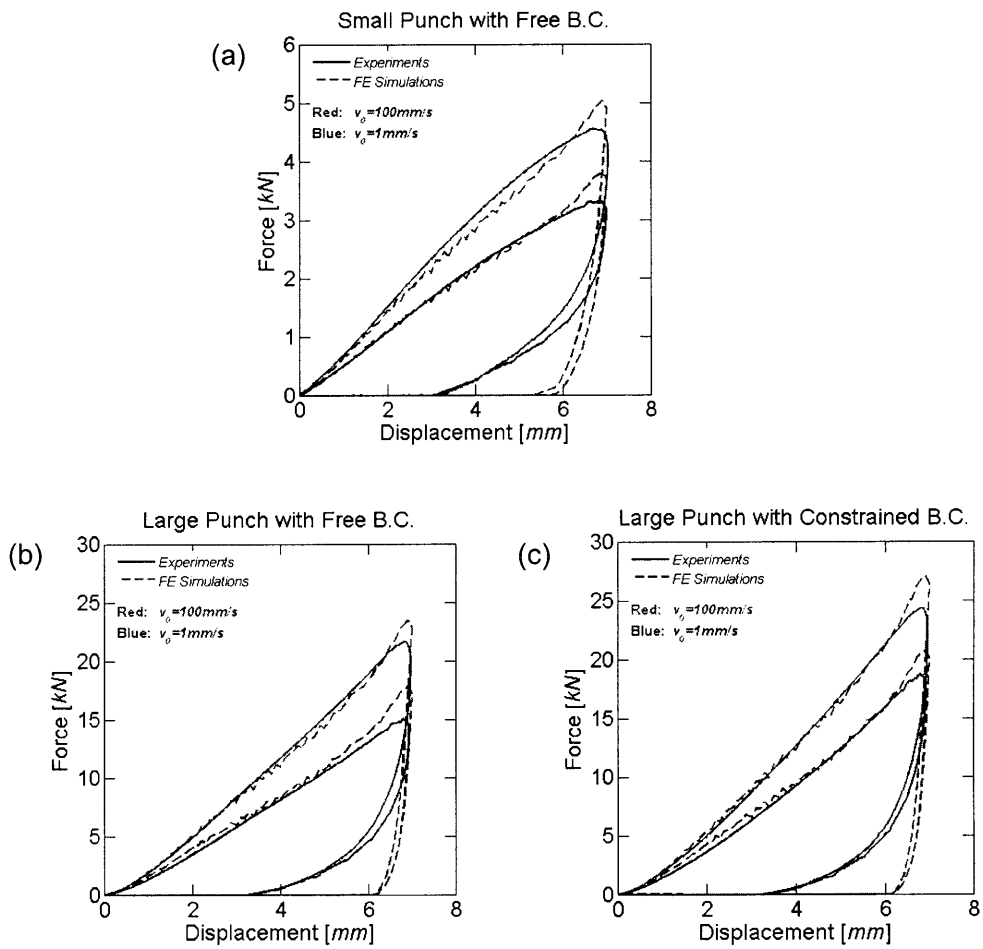

Figure 4-7: Comparison of simulations and experiments. Force-displacement curves for (a) small punch with free lateral boundaries, (b) large punch with the free lateral boundaries, (c) large punch with constraint in the width direction.

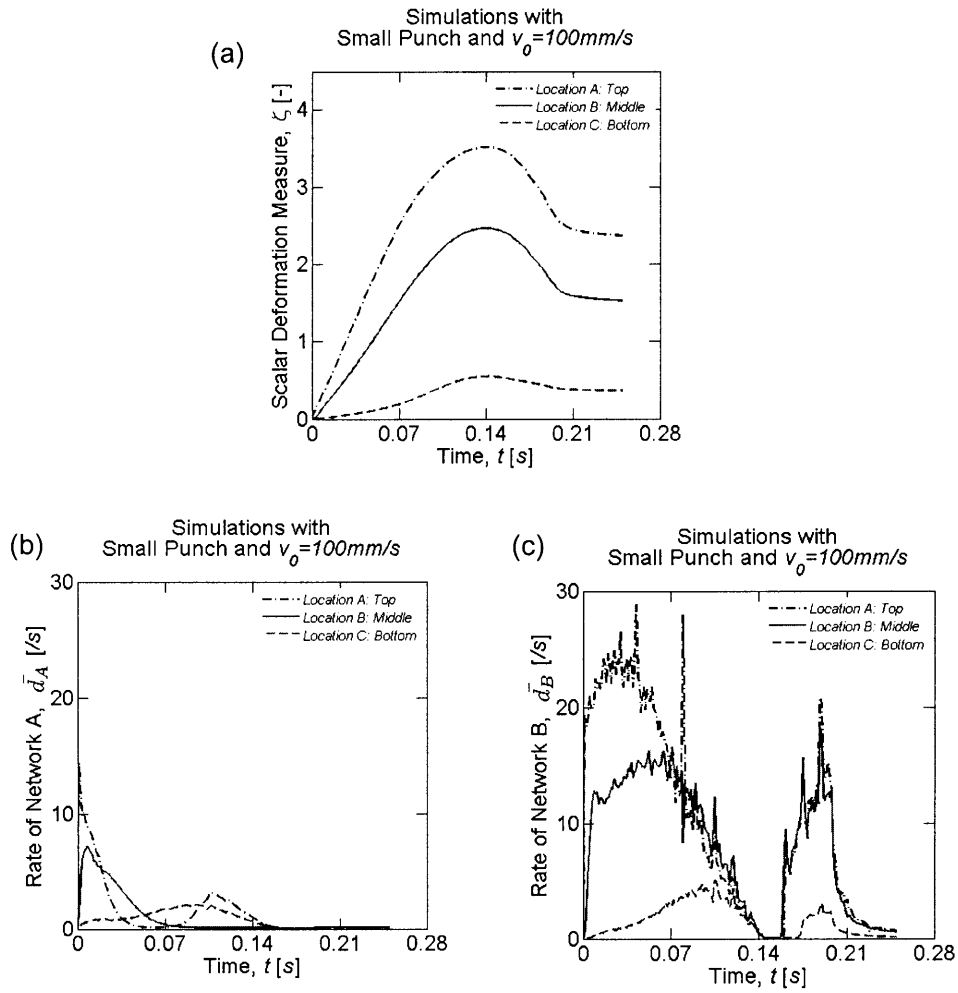

Figure 4-8: Results from the small punch simulation with $v_0 = 100mm/s$ and free lateral boundary conditions at three different locations (labeled by $\boldsymbol{A}$, $\boldsymbol{B}$ and $\boldsymbol{C}$ in Figure 4-6(a): Histories of (a) the strain-like deformation measure, ζ, (b) the viscous strain rate of $Network\ A$, $\bar{d}_A$, (c) the viscous strain rate of $Network\ B$, $\bar{d}_B$. Note that the loading direction is reversed at $t = 0.14s$.

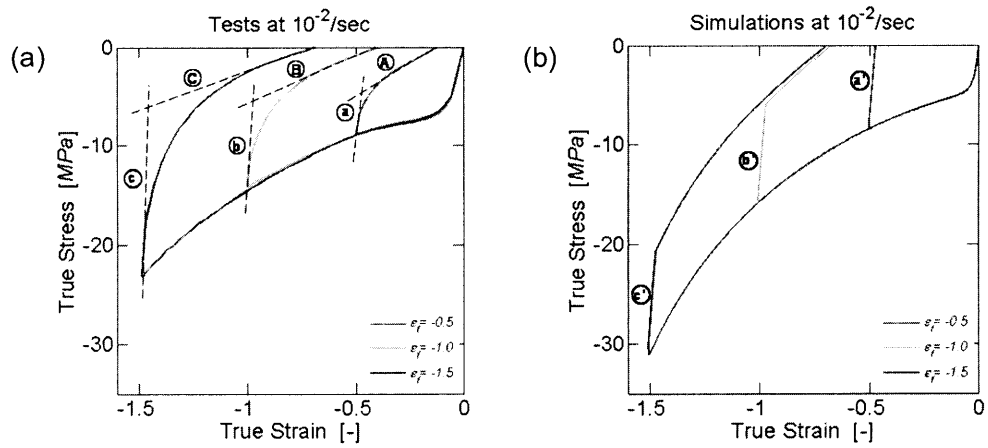

Figure 4-9: Stress-strain curves for a single loading-unloading cycle at $\dot{\varepsilon} = 10^{-2}/s$ as obtained from (a) experiments and (b) simulations.

increases. As the applied maximum strain increases, the simulations predict almost constant stress drops (marked by $\boldsymbol{a}'$, $\boldsymbol{b}'$ and $\boldsymbol{c}'$ in Figure 4-9b) while the experiments show a substantial increase in the magnitude of the stress drops as a function of strain (marked by $\boldsymbol{a}$, $\boldsymbol{b}$ and $\boldsymbol{c}$ in Figure 4-9a).

Recall that *Network A* in the current constitutive model is mainly responsible for the rubbery behavior while *Network B* describes the high initial stiffness and the time-dependent hysteresis. The contributions of *Networks A* and *B* are in opposite direction as far as the hysteresis width is concerned. To shed more light on this particular feature, Figure 4-10 shows a direct comparison of the model response and the experiments. In addition, we plotted the individual contributions of *Network A* and *Network B* to the stress-strain curve (dashed curves in Figure 4-10). Note that the magnitude of the stress contribution of *Network B* depends on the compressive strain only, while its sign changes from compression to tension upon unloading. The contribution of *Network A* on the other hand is a compressive stress irrespective of the loading direction. Thus, as the compressive strain increases, *Network B* makes the hysteresis wider while the opposite holds true for *Network A*. In order to replicate the experimental observation of a hysteresis width increase as a function of the maximum compressive strain (Figure 4-9a), the contribution of *Network B* should be dominant. Moreover, the contribution

of *Network B* would need to increase as the compressive strain increases. However, due to the specific choice of the viscous evolution law for *Network B*, the stress contribution of *Network B* is more or less constant once the compressive strain has exceeded -0.1 (see the stress plateau in the response curves for *Network B* in Figure 4-10). An attempt was made to change the calibration of the response of *Network B* using the present modeling framework, but the subsequent simulation results were no longer satisfactory for the phase of loading.

A constitutive model with a different rheological composition needs to be used to improve the predictions for unloading. A previous study (Shim and Mohr, 2009b) has shown that models of the Zener-type (spring in parallel with a single Maxwell element) cannot describe the large deformation behavior of polyurea over a wide range of strain rates. The present results indicate that the assumption of two Maxwell elements in parallel provides an accurate description for monotonic loading only. It can describe the two characteristic stiff and soft regimes during unloading over a wide range of strain rates, but the model predictions are only in poor quantitative agreement during unloading.

Throughout our model development, we focused on a single loading-unloading cycle on virgin-state specimens. However, even though the loading of the material in its virgin state appears to be the most important with respect to the real-life applications of polyurea, the material response to cyclic loading may be instructive as far as the choice of the rheological model is concerned. Figure 4-11 shows the stress-strain curve for polyurea for five consecutive loading-unloading cycles. After each loading-unloading cycle at a constant true strain rate of $10^{-2}/s$, we let the specimen creep at zero stress for about $300s$ before applying the subsequent loading-unloading cycle. The significant difference between the first and subsequent loading cycles illustrates the Mullins effect for polyurea. The stress-strain curve for the first loading is characterized by the high initial stiffness and the high peak stress marked as $\boldsymbol{A}$. After the first loading-unloading cycle, however, the shape of the loading path changes noticeably while nearly the same unloading path is observed. Additional loading-unloading cycles create very little changes in both loading and unloading. This observation suggests that the constitutive model should comprise an internal variable that reflects the amount of "microstructural damage" associated with the Mullins effect. The Mullins effect has been investigated by many research groups using either damage-based constitutive models (e.g., Simo, 1987, Govindjee and Simo,

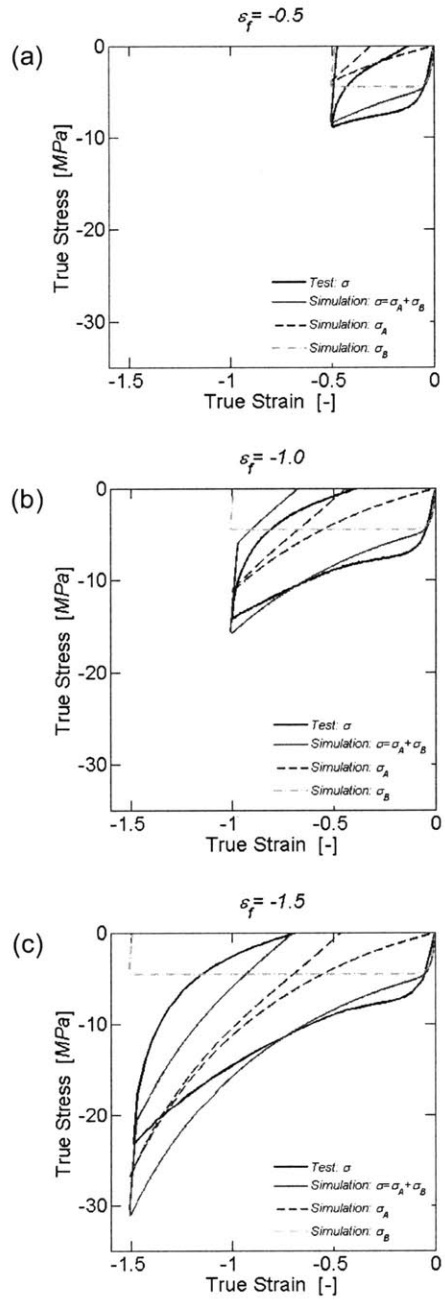

Figure 4-10: Comparison of simulation results and experiments for continuous loading/unloading cycles at $\dot{\varepsilon} = 10^{-2}/s$. (a) $\varepsilon_f = -0.5$, (b) $\varepsilon_f = -1.0$, (c) $\varepsilon_f = -1.5$.

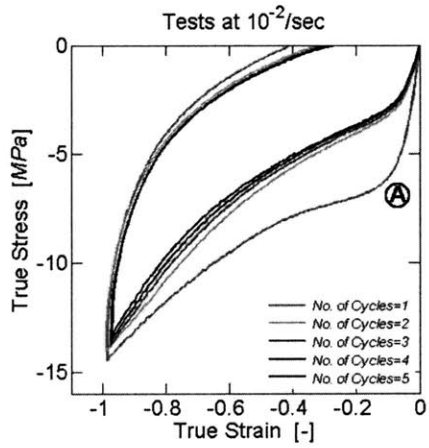

Figure 4-11: Illustration of the Mullins effect. Five compression loading and unlading cycles are performed at the constant strain rate of $10^{-2}/s$ up to the maximum strain of -1.0. The stress is zero between subsequent cycles for about five minutes.

1991, 1992, Lion, 1996, 1997, Miehe and Keck, 2000) or the concept of hard/soft domain reorganization (e.g. Johnson and Beatty, 1993a, 1993b, Beatty and Krishnaswamy, 2000, Qi and Boyce, 2004, 2005). Here, the explicit account of the Mullins effect is deferred to future work since further experimental data is needed to analyze the effect of loading velocity over a wide range of strain rates.

4.6 Conclusion

Punch experiments have been performed on $10mm$ thick polyurea samples at punch velocities of up to $100mm/s$ which resulted in maximum local viscous strain rates of up to $30/s$ inside the polyurea layers. A newly-developed rate-dependent constitutive model for polyurea has been implemented into a finite element program and used to predict the experimentally-measured force-displacement curves for different punch sizes and velocities. Furthermore, the effect of lateral constraints has been investigated. The model provides accurate predictions of the loading response for all six test configurations which is interpreted as a partial validation of the assumptions made with respect to strain-rate and pressure sensitivity. During unloading, the

model exhibits the characteristic stiff and soft responses of polyurea; however, it systematically overestimates the depth of the quasi-instantaneous residual punch imprint after unloading.

Chapter 5

Conclusion and Suggestions

5.1 Summary of Main Results

The main results of this dissertation can be summarized twofold: experiments and constitutive modeling. First, the effect of strain rate on polyurea are experimentally quantified for a wide range of strain rates, i.e. $10^{-3}/s \sim 4000/s$. The modified SHPB system of Zhao and Gary (1997) has been used to perform compression tests on polyurea at low, intermediate and high strain rates ($10/s \sim 1000/s$). It is composed of nylon input and output bars, while the striker bar is substituted by a hydraulic actuator. Using the deconvolution technique by Bussac et al. (2002), the time limitation of conventional SHPB systems may be overcome, thereby enabling the use of the modified SHPB system for low and intermediate strain rate experiments of long duration. The experiments confirm the known strain rate sensitivity of polyurea. The measured stress levels correspond well to earlier results which have been obtained from tests on conventional SHPB systems with very long bars.

Second, a new constitutive model is proposed to capture the rate-sensitivity for a wide range of strain rates and the characteristic high stiffness behavior of virgin polyurea at small strains. Various types of loading conditions are tested for the purpose of validation, and their results are well compared with the model predictions in loading phases. The large strain compression response of polyurea is investigated for strain rates ranging $10^{-3}/s$ from to $10^{1}/s$. Continuous and stair-like loading and unloading experiments are performed in addition to simple relaxation tests. The experimental results reveal that the so-called equilibrium path concept breaks down

in the case of polyurea. In contradiction with the definition of the equilibrium path, the identified average stress-strain curves in continuous loading/unloading experiments depend on the rate of loading. Thus, as an alternative to the equilibrium path based rheological models of the Zener type, a new constitutive model is formulated assuming two parallel Maxwell elements. The finite strain constitutive equations are outlined in detail, and it has been implemented into a finite element program. Subsequently, the eight material model constants are calibrated to describe the mechanical behavior of polyurea. The model predictions are in good agreement with the experimental results. The characteristic convergence of the unloading paths for different strain rates is successfully captured by the model. Furthermore, the rate dependent viscous dissipation throughout a loading/unloading cycle of uniaxial conditions is described with reasonable accuracy. For the validation of the proposed model, punch experiments have been performed on $10mm$ thick polyurea samples at punch velocities of up to $100mm/s$ which resulted in maximum local viscous strain rates of up to $30/s$ inside the polyurea layers. The proposed constitutive model is used to predict the experimentally-measured force-displacement curves for different punch sizes and velocities. Furthermore, the effect of lateral constraints has been investigated. The model provides accurate predictions of the loading response for all six test configurations which is interpreted as a partial validation of the assumptions made with respect to strain-rate and pressure sensitivity.

5.2 Suggestions for Future Studies

The following topics can be suggested for future studies:

- *Constant strain rates from the hydraulic SHPB*: Although the intrinsic time limitation of SHPB systems could be overcome, this study also shows that it is still not possible to perform experiments at reasonably constant strain rates with this technique. This is due to the finite length (i.e. $3m$ in this study) of the input and output bars which causes a periodic change in loading velocity. It is shown that intermediate strain rate SHPB experiments require either very long bars ($> 20m$) or very short bars ($< 0.5m$) in order to achieve an approximately constant strain rate throughout the entire experiment.

- *Improvement in the fixed boundary conditions in the hydraulic SHPB*: In order to prevent

the failure of the nylon bars under excessive loads, a fixed end support system in the hydraulic SHPB of the current study is designed such that the bars are released before elastic buckling occurs. However, with the current design of the fixed end, significant force drops are found during tests due to the premature partial failure of the fixed end support of the output bar. A new design of the fixed end support can be investigated to prevent the elastic buckling of the bars and to resist the specimen strength at the same time.

- *Improvement in the unloading prediction of the constitutive model*: From various tests with different loading conditions, the model exhibits the characteristic stiff and soft responses of polyurea during unloading. However, the predicted unloading behavior is too stiff, and the model systematically overestimates the depth of the quasi-instantaneous residual strain/displacement after unloading. A new rheological model can be investigated to improve the prediction of unloading behavior and to capture the Mullins effect for polyurea.

Appendix A

Identification of the Wave Propagation Coefficient for Viscoelastic Bars

The complex-valued propagation coefficient $\xi(\omega)$ is a function of both the geometric and material properties of the bars. If the complex modulus of the viscoelastic bar material is known, $\xi(\omega)$ may be calculated from solving Pochhammer-Chree's frequency equation (Zhao and Gary, 1995). As an alternative, we make use of an experimental method that considers both geometric dispersion and viscous attenuation within the framework of the 1-D wave theory (e.g. Bacon, 1998, Lundberg and Blanc, 1988) to determine $\xi(\omega)$. Recall the solution of the one-dimensional wave equation for viscoelastic bars,

$$\hat{\varepsilon}(x,\omega) = \hat{\varepsilon}_R(\omega)\, e^{-i\xi(\omega)x} + \hat{\varepsilon}_L(\omega)\, e^{i\xi(\omega)x} \tag{A.1}$$

where $\hat{\varepsilon}_R(x,\omega)$ and $\hat{\varepsilon}_L(x,\omega)$ are the rightward and the leftward traveling strain waves. Here, $\xi(\omega)$ is the propagation coefficient of the bars defined by

$$\xi(\omega) = \kappa(\omega) + i\bar{\alpha}(\omega) = \frac{\omega}{c(\omega)} + i\bar{\alpha}(\omega) \tag{A.2}$$

where $\kappa(\omega)$ is the wave number, $c(\omega)$ is the frequency-dependant longitudinal wave propagation speed, and $\bar{\alpha}(\omega) \leq 0$ represents the attenuation coefficient. Note that $c(\omega)$ and $\bar{\alpha}(\omega)$ are even functions of ω while $\kappa(\omega)$ is an odd function in the frequency space.

After performing an impact test on a single bar, we measure the incident and reflected strain histories (i.e. $\varepsilon_{inc}(x=0,t)$ and $\varepsilon_{ref}(x=0,t)$) at $x=0$ within in the bar. In order to determine the transfer function of the bar, we use the two facts from the impact test:

- The rightward and the leftward travelling strain waves are equal to the measured incident and reflected strain histories, respectively:

$$\hat{\varepsilon}_R(\omega) = \hat{\varepsilon}_{inc}(x=0,\omega) \tag{A.3}$$

$$\hat{\varepsilon}_L(\omega) = \hat{\varepsilon}_{ref}(x=0,\omega) \tag{A.4}$$

- The normal force is zero at the free end of the bar (i.e. the opposite end to the impacting end of the bar):

$$\hat{\varepsilon}_R(\omega)\, e^{-i\xi(\omega)d} + \hat{\varepsilon}_L(\omega)\, e^{i\xi(\omega)d} = 0 \tag{A.5}$$

  where $x=d$ is the distance between the strain gage location and the free end of the bar.

Now, the transfer function of the bar $H(\omega)$ is experimentally determined from

$$H(\omega) = -\frac{\hat{\varepsilon}_{ref}(x=0,\omega)}{\hat{\varepsilon}_{inc}(x=0,\omega)} = e^{-2i\xi(\omega)d} \tag{A.6}$$

From Eq. (A.6), two components of the propagation coefficient can be identified using the relations

$$\kappa(\omega) = -\frac{\arg[H(\omega)]}{2d} \tag{A.7}$$

$$\bar{\alpha}(\omega) = \frac{\ln[|H(\omega)|]}{2d} \tag{A.8}$$

Appendix B

List of Papers with Reference to Respective Chapters

The following papers are published or submitted for publication with reference to the respective chapters.

Chapter 2

Shim, J. and Mohr, M. (2009) "Using split Hopkinson pressure bars to perform large strain compression tests on polyurea at low, intermediate and high strain rates," *International Journal of Impact Engineering*, **36**:1116-1127.

Chapter 3

Shim, J. and Mohr, M. (2009) "Finite strain constitutive model of polyurea for a wide range of strain rates," *(submitted for publication, September 2009).*

Chapter 4

Shim, J. and Mohr, M. (2009) "Punch indentation of polyurea at different loading velocities: Experiments and numerical simulations," *(submitted for publication, October 2009).*

Bibliography

[1] Aloui, S., Othman, R., Poitou, A., Guégan, P. and El-Borgi, S. (2008) "Non-parametric identification of the non-homogeneous stress in high strain-rate uni-axial experiments," *Mechanics Research Communications*, **35**:392–397.

[2] Ames, N.M., Srivastava, V., Chester, S.A. and Anand, L. (2009) "A thermo-mechanically coupled theory for large deformations of amorphous polymers. Part II: Applications," *International Journal of Plasticity*, **25**:1495-1539.

[3] Amin, A.F.M.S., Alam, M.S. and Okui, Y. (2002) "An improved Hyperelasticity relation in modeling viscoelasticity response of natural and high damping rubbers in compression: Experiments, parameter identification and numerical verification," *Mechanics of Materials*, **34**:75-95.

[4] Amin, A.F.M.S., Lion, A., Sekita, S. and Okui, Y. (2006) "Nonlinear dependence of viscosity in modeling the rate-dependent response of natural and high damping rubbers in compression and shear: Experimental identification and numerical verification," *International Journal of Plasticity*, **22**:1610-1657.

[5] Amini, M.R., Isaacs, J. and Nemat-Nasser, S. (2009a) "Investigation of effect of polyurea on response of steel plates to impulsive loads in direct pressure-pulse experiments," *Mechanics of Materials*, in press, doe: 10.1016/j.mechmat.2009.09.008.

[6] Amini, M.R., Simon, J. and Nemat-Nasser, S. (2009b) "Numerical modeling of effect of polyurea on response of steel plates to impulsive loads in direct pressure-pulse experiments," *Mechanics of Materials*, in press, doe: 10.1016/j.mechmat.2009.09.009.

[7] Amirkhizi, A.V., Isaacs, J., McGee, J. and Nemat-Nasser, S. (2006) "An experimentally-based viscoelastic constitutive model for polyurea, including pressure and temperature effects," *Philosophical Magazine*, **86**:5847–5866.

[8] Anand, L. and Ames, N.M. (2006) "On modeling the micro-indentation response of an amorphous polymer," *International Journal of Plasticity*, **22**:1123-1170.

[9] Anand, L., Ames, N.M., Srivastava, V. and Chester, S.A. (2009) "A thermo-mechanically coupled theory for large deformations of amorphous polymers. Part I: Formulation," *International Journal of Plasticity*, **25**:1474-1494.

[10] Areias, P. and Matous, K. (2008) "Finite element formulation for modeling nonlinear viscoelastic elastomers," *Computational Methods in Applied Mechanical Engineering*, **197**:4702-4717.

[11] Arruda, E.M. and Boyce, M.C. (1993) "A 3-dimensional constitutive model for the large stretch behavior of rubber elastic materials," *Journal of the Mechanics and Physics of Solids*, **41**:389-412.

[12] Ayoub, C., Zaïri F., Naït-Abdelaziz, M. and Gloaguen, J.M. (2009) "Modelling large deformation behaviour under loading-unloading of semicrystalline polymers: Application to a high density polyethylene," *International Journal of Plasticity*, in press, doi:10.1016/j.ijplas.2009.07.005.

[13] Bacon, C. (1998) "An experimental method for considering dispersion and attenuation in a viscoelastic Hopkinson bar," *Experimental Mechanics*, **38**:242–249.

[14] Bacon, C. (1999) "Separation of waves propagating in an elastic or viscoelastic Hopkinson pressure bar with three-dimensional effects," *International Journal of Impact Engineering*, **22**:55–69.

[15] Beatty, M.F. and Krishnaswamy, S. (2000) "A theory of stress-softening in incompressible isotropic materials," *Journal of the Mechanics and Physics of Solids*, **48**:1931-1965.

[16] Bergström, J.S. and Boyce, M.C. (1998). "Constitutive modeling of the large strain time-dependent behavior of elastomers," *Journal of the Mechanics and Physics of Solids*, **46**:931-954.

[17] Bergström, J.S. and Hilbert, L.B. (2005) "A constitutive model of predicting the large deformation thermomechanical behavior of fluoropolymers," *Mechanics of Materials*, **37**:899-913.

[18] Bernstein, B., Kersley, E.A. and Zapas, L.J. (1963) "A study of stress relaxation with finite strain," *Transaction of the Society of Rheology*, **7**:391-410.

[19] Bogoslovov, R.B. and Roland, C.M. (2007) "Viscoelastic effects on the free retraction of rubber," *Journal of Applied Physics*, **102**:063531.

[20] Bordonaro, C.M. and Krempl, E. (1992) The effect of strain rate on the deformation and relaxation behavior of 6/6 nylon," *Polymer Engineering and Science*, **32**:1066–1072.

[21] Boyce, M.C., Parks, D.M. and Argon, A.S. (1988) "Large inelastic deformation of glassy polymers. Part I: Rate dependent constitutive model," *Mechanics of Materials*, **7**:15–33.

[22] Boyce, M.C., Socrate, S. and Llana, P.G. (2000) "Constitutive model for the finite deformation stress-strain behavior of poly(ethylene terephthalate) above the glass transition," *Polymer*, **41**:2183-2201.

[23] Brinson, H.F. and Brinson, L.C. (2008) *Polymer Engineering Science and Viscoelasticity: An Introduction*, New York, NY, Springer Science+Business Media, LLC, p327.

[24] Bussac, M.N., Collet, P., Gary, G. and Othman, R. (2002) "An optimization method for separating and rebuilding one-dimensional dispersive waves form multi-point measurements. Application to elastic or viscoelastic bars," *Journal of the Mechanics and Physics of Solids*, **50**:321–349.

[25] Cady, C.M., Blumenthal, W.R., Gray, G.T. and Idar, D.J. (2003) "Determining the constitutive response of polymeric materials as a function of temperature and strain rate," *Journal de Physique IV*, **110**:27–32.

[26] Casem, D.T., Fourney, W. and Chang P. (2003) "Wave separation in viscoelastic pressure bars using single point measurements of strain and velocity," *Polymer Testing*, **22**:155–164.

[27] Chen, W., Zhang, B. and Forrestal M.J. (1999) "A split Hopkinson bar technique for low impedance materials," *Experimental Mechanics*, **39**:81–85.

[28] Chou, S.C., Roberstson, K.D. and Rainey, J.H. (1973) "The effect of strain rate and heat developed during deformation on the stress–strain curve of plastics," *Experimental Mechanics*, **13**:422–432.

[29] Colak, O.U. (2005) "Modeling deformation behavior of polymers with viscoplasticity theory based on overstress," *International Journal of Plasticity*, **21**:145-160.

[30] Coleman, B.D. and Noll, W. (1961) "Foundations of linear viscosity," *Reviews of Modern Physics*, **33**:239-249.

[31] Dupaix, R.B. and Boyce, M.C. (2007) "Constitutive modeling of the finite strain behavior of amorphous polymers in and above the glass transition," *Mechanics of Materials*, **39**:39-52.

[32] Gent, A.N. (1996) "A new constitutive relation for rubber," *Rubber Chemistry and Technology*, **69**:59-61.

[33] Govindjee, S. and Simo, J. (1991) "A micro-mechanically based continuum damage model for carbon black-filled rubbers incorporating Mullins effect," *Journal of the Mechanics and Physics of Solids*, **39**: 87-112.

[34] Govindjee, S. and Simo, J. (1992) "Mullins effect and the strain amplitude dependence of the storage modulus," *International Journal of Solids and Structures*, **29**:1737-1751.

[35] Graff, K.F. (1975) *Wave Motion in Elastic Solids*, Mineola, NY, Dover Publications, Inc., p470.

[36] Gray, G.T. and Blumenthal, W.R. (2000) "Split-Hopkinson pressure bar testing of soft materials," *ASM Handbook Volume 8: Mechanical Testing and Evaluation*, **8**:488–496.

[37] Gray, G.T., Blumenthal, W.R., Trujillo, C.P. and Carpenter, R.W. (1997) "Influence of temperature and strain rate on the mechanical behavior of Adiprene L-100," *Journal de Physique IV*, **7**:523–528.

[38] Grolleau, V., Gary, G. and Mohr, D. (2008) "Biaxial testing of sheet materials at high strain rates using viscoelastic bars," *Experimental Mechanics*, **48**:293–306.

[39] Guduru, P.R., Bharath, M.S. and Freund, L.B. (2006) "The influence of a surface coating on the high-rate fragmentation of a ductile material," *International Journal of Fracture*, **137**:89-108.

[40] Haupt, P. and Lion, A. (2002) "On finite linear viscoelasticity of incompressible isotropic materials," *Acta Mechanica*, **159**:87-124.

[41] Hillström, L., Mossberg, M. and Lundberg, B. (2000) "Identification of complex modulus from measured strains on an axially impacted bar using least squares," *Journal of Sound and Vibration*, **230**:689–707.

[42] Hoo Fatt, M.S. and Bekar, I. (2004) "High-speed testing and material modeling of unfilled styrene butadiene vulcanizates at impact rates," *Journal of Materials Science*, **39**:6885–6899.

[43] Hoo Fatt, M.S. and Ouyang, X. (2007) "Integral-based constitutive equation for rubber at high strain rates," *International Journal of Solids and Structures*, **44**:6491-6506.

[44] Hoo Fatt, M.S. and Ouyang, X. (2008) "Three-dimensional constitutive equations for styrene butadiene rubber at high strain rates," *Mechanics of Materials*, **40**:1-16.

[45] Huber, N. and Tsakmakis, C. (2000) "Finite deformation viscoelasticity laws," *Mechanics of Materials*, **32**:1-18.

[46] Jacquelin, E. and Hamelin, P. (2001) "Block-bar device for energy absorption analysis," *Mechanical Systems and Signal Processing*, **15**:603–617.

[47] Jacquelin, E. and Hamelin, P. (2003) "Force recovered from three recorded strains," *International Journal of Solids and Structures*, **40**:73–88.

[48] Johlitz, M., Steeb, H., Diebels, S., Chatzouridou, A., Batal, J. and Possart, W. (2007) "Experimental and theoretical investigation of nonlinear viscoelastic polyurethane systems," *Journal of Materials Science*, **42:**9894-9904.

[49] Johnson, A.R., Quigley, C.J. and Freese, C.E. (1995) "A visco hyperelastic finite element model for rubber," *Computational Methods in Applied Mechanical Engineering*, **127**:163-180.

[50] Johnson, A.R., Quigley, C.J. and Mead, J.L. (1994) "Large-strain viscoelastic constitutive models for rubber, I. Formulations," *Rubber Chemistry and Technology*, **67**:904-917.

[51] Johnson, M.A. and Beatty, M.F. (1993a) "The Mullins effect in uniaxial extension and its influence on the transverse vibration of a rubber string," *Continuum Mechanics and Thermodynamics*, **5**:83-115.

[52] Johnson, M.A. and Beatty, M.F. (1993b) "A constitutive equation for the Mullins effect in stress controlled uniaxial extension experiments," *Continuum Mechanics and Thermodynamics*, **5**:301-318.

[53] Khan, A. and Zhang, H. (2001) "Finite deformation of a polymer: experiments and modeling," *International Journal of Plasticity*, **17**:1167-1188.

[54] Khan, A.S. and Farrokh, B. (2006) "Thermo-mechanical response of nylon 101 under uniaxial and multi-axial loadings: Part I, Experimental results over wide ranges of temperatures and strain rates," *International Journal of Plasticity*, **22**:1506-1529.

[55] Khan, A.S., Lopez-Pamies, O. and Kazmi, R. (2006) "Thermo-mechanical large deformation response and constitutive modeling of viscoelastic polymers over a wide range of strain rates and temperatures," *International Journal of Plasticity*, **22**:581-601.

[56] Kröner, E. (1960) "Allgemeine kontinuumstheorie der versetzungen und eigenspannungen," *Archive for Rational Mechanics and Analysis*, **4**:273–334.

[57] Lee, E.H. (1969) "Elastic plastic deformation at finite strain," *ASME Journal of Applied Mechanics*, **36**:1–6.

[58] Leonov, A.I. (1976) "Nonequilibrium thermodynamics and Rheology of viscoelastic polymer media," *Rheologica Acta*, **15**:85-98.

[59] Le Tallec, P., Rahier, C. and Kaiss, A. (1993) "Three-dimensional incompressible viscoelasticity in large strains: Formulation and numerical approximation," *Computer Methods in Applied Mechanics and Engineering*, **109**:233-258.

[60] Lianis, G. (1963) *Constitutive Equations of Viscoelastic Solids under Large Deformations*, A & ES Report No.63-5, Purdue University.

[61] Lion, A. (1996) "A constitutive model for carbon black filled rubber: Experimental investigations and mathematical representation," *Continuum Mechanics and Thermodynamics*, **8**:153-169.

[62] Lion, A. (1997) "A physically based method to represent the thermo-mechanical behaviour of elastomers," *Acta Mechanica*, **123**:1-25.

[63] Lockett, F.J. (1972) *Nonlinear Viscoelastic Solids*, New York, NY, Academic Press Inc., p59.

[64] Lubliner, J. (1985) "A model of rubber viscoelasticity", *Mechanics Research Communications*, **12**:93-99.

[65] Lundberg, B. and Blanc, R.H. (1988) "Determination of mechanical material properties from the two-points response of an impacted linearly viscoelastic rod specimen," *Journal of Sound and Vibration*, **126**:97–108.

[66] Lundberg, B. and Henchoz, A. (1977) "Analysis of elastic-waves from 2-point strain measurement," *Experimental Mechanics*, **17**:213–218.

[67] Magnus, J.R. and Neudecker, H. (1988) *Matrix differential calculus with applications in statics and econometrics*, Chichester, England, John Wiley & Sons Ltd., p15.

[68] McGrum, N.G., Buckley, C.P. and Bucknal, C.B. (1997) *Principles of Polymer Engineering*, New York, NY, Oxford University Press, p117.

[69] McGuirt, C.W. and Lianis, G. (1970) "Constitutive equations for viscoelastic solids under finite uniaxial and biaxial deformations," *Transaction of the Society of Rheology*, **14**:117–134.

[70] McShane, G.J., Stewart, C., Aronson, M.T., Wadley, H.N.G., Fleck, N.A. and Deshpande, V.S. (2008) "Dynamic rupture of polymer-metal bilayer plates," *International Journal of Solids and Structures*, **45**:4407-4426.

[71] Miehe, C. and Keck, J. (2000) "Superimposed finite elastic-viscoelastic-plastoelastic stress response with damage in filled rubbery polymers. Experiments, modelling and algorithmic implementation," *Journal of the Mechanics and Physics of Solids*, **48**:323-365.

[72] Mulliken, A.D. and Boyce, M.C. (2006) "Mechanics of the rate-dependent elastic-plastic deformation of glassy polymers from low to high strain rates," *International Journal of Solids and Structures*, **43**:1331-1356.

[73] Mulliken, A.D., Soong, S.Y., Boyce, M.C. and Cohen, R.E. (2006) "High-rate thermomechanical behavior of poly(vinyl chloride) and plasticized poly(vinyl chloride)," *Journal de Physique IV*, **134**:217–223.

[74] Ogden, R.W. (1984) *Non-linear Elastic Deformations*, New York, NY, Ellis Horwood Limited, p.209.

[75] Othman, R. and Gary, G. (2007) "Testing aluminum alloy from quasi-static to dynamic strain-rates with a modified split Hopkinson bar method," *Experimental Mechanics*, **47**:295–299.

[76] Othman, R. and Guegan, P., Challita, G., Pasco, F. and LeBreton, D. (2009) "A modified servohydraulic machine for testing at intermediate strain rates," *International Journal of Impact Engineering*, **36**:460–467.

[77] Palm, G., Dupaix, R.B. and Castro, J. (2006) "Large strain mechanical behavior of poly(methyl methacrylate) (PMMA) near the glass transition temperature," *Journal of Engineering Materials and Technology*, **128**:559-563.

[78] Park, S.W. and Zhou, M. (1999) "Separation of elastic waves in split Hopkinson bars using one-point strain measurements," *Experimental Mechanics*, **39**:287–294.

[79] Qi, H.J. and Boyce, M.C. (2004) "Constitutive model for stretch-induced softening of the stress-stretch behavior of elastomeric materials," *Journal of the Mechanics and Physics of Solids*, **52**:2187-2205.

[80] Qi, H.J. and Boyce, M.C. (2005) "Stress-strain behavior of thermoplastic polyurethanes," *Mechanics of Materials*, **37**:817-839.

[81] Quintavalla, S.J. and Johnson, S.H. (2004) "Extension of the Bergström-Boyce model to high strain rates," *Rubber Chemistry and Technology*, **77**:972-981.

[82] Rao, S., Shim, V.P.W. and Quah, S.E. (1997) "Dynamic mechanical properties of polyurethane elastomers using a nonmetallic Hopkinson bar," Journal of Applied Polymer Science, **66**:619–631.

[83] Reese, S. and Govindjee, S. (1998) "A theory of finite viscoelasticity and numerical aspects," *International Journal of Solids and Structures*, **35**:3455-3482.

[84] Roland, C.M. (1989) "Network recovery from uniaxial extension, I: Elastic equilibrium", *Rubber Chemistry Technology*, **62**:863-879.

[85] Roland, C.M. (2006) "Mechanical behavior of rubber at high strain rates," *Rubber Chemistry and Technology*, **79**:429–459.

[86] Roland, C.M., Twigg, J.N., Vu, Y. and Mott, P.H. (2007) "High strain rate mechanical behavior of polyurea," *Polymer*, **48**:574–578.

[87] Sarva, S.S., Deschanel, S., Boyce, M.C. and Chen, W. (2007) Stress-strain behavior of a polyurea and a polyurethane from low to high strain rates," *Polymer*, **48**:2208-2213.

[88] Sharma, A., Shukla, A. and Prosser, R.A. (2002) "Mechanical characterization of soft materials using high speed photography and split Hopkinson pressure bar technique," *Journal of Materials Science*, **37**:1005–1017.

[89] Shergold, O.A., Fleck, N.A. and Radford, D. (2006) "The uniaxial stress versus strain response of pig skin and silicon rubber at low and high strain rates," *International Journal of Impact Engineering*, **32**:1384–1402.

[90] Shim, J. and Mohr, D. (2009a) "Using split Hopkinson pressure bars to perform large strain compression tests on polyurea at low, intermediate and high strain rates," *International Journal of Impact Engineering*, **36**:1116-1127.

[91] Shim, J. and Mohr, D. (2009b) "Finite strain constitutive model of polyurea for a wide range of strain rates," submitted for publication.

[92] Shim, V.P.W., Yang, L.M., Lim, C.T. and Law, P.H. (2004) "A visco-hyperelastic constitutive model to characterize both tensile and compressive behavior of rubber," *Journal of Applied Polymer Science*, **92**:523-531.

[93] Sidoroff, F. (1974) "Un modèle viscoélastique non linéaire avec configuration intermédiaire," *Journal de Mécanique*, **13**:679–713.

[94] Simo, J.C. (1987) "On a fully 3-dimensional finite-strain viscoelastic damage model - Formulation and computational aspects," *Computer Methods in Applied Mechanics and Engineering*, **60**:153-173.

[95] Siviour, C.R., Walley, S.M., Proud, W.G. and Field, J.E. (2005) "The high strain rate compressive behaviour of polycarbonate and polyvinylidene difluoride," *Polymer*, **46**:12546–12555.

[96] Song, B. and Chen, W. (2003) "One-dimensional dynamic compressive behavior of EPDM rubber," *Journal of Engineering Materials and Technology, Transaction of the ASME*, **125**:294–301.

[97] Song, B. and Chen, W. (2004) "Dynamic compressive behavior of EPDM rubber under nearly uniaxial strain conditions," *Journal of Engineering Materials and Technology, Transaction of the ASME*, **126**:213–217.

[98] Song, B., Chen, W. and Lu, W.Y. (2007) "Mechanical characterization at intermediate strain rates for rate effects on an epoxy syntactic foam," *International Journal of Mechanical Sciences*, **49**:1336–1343.

[99] Strang, G. (1985) *Introduction to Applied Mathematics*, Wellesley, MA, Wellesley-Cambridge Press, p32.

[100] Tomita, Y., Azuma, K. and Naito, M. (2008) "Computational evaluation of strain-rate-dependent deformation behavior of rubber and carbon-black-filled rubber under monotonic and cyclic straining," *International Journal of Mechanical Sciences*, **50**:856-868.

[101] Walley, S.M., Field, J.E., Pope, P.H. and Safford, N.A. (1989) "A study of the rapid deformation behaviour of a range of polymers," *Philosophical Transactions of the Royal Society of London Series A-Mathematical Physical and Engineering Sciences*, **328**:1–33.

[102] Xue, Z.Y. and Hutchinson, J.W. (2008) "Neck development in metal/elastomer bilayers under dynamic stretchings," *International Journal of Solids and Structures*, **45**:3769-3778.

[103] Yanagihara, N. (1978) "New measuring method of impact force," *Bulletin of the Japan Society of Mechanical Engineers*, **21**:1085–1088.

[104] Yang, L.M., Shim, V.P.W. and Lim, C.T. (2000) "A visco-hyperelastic approach to modelling the constitutive behaviour of rubber," *International Journal of Impact Engineering*, **24**:545-560.

[105] Yi, J., Boyce, M.C., Lee, G.F. and Balizer, E. (2006) "Large deformation rate-dependent stress–strain behavior of polyurea and polyurethanes," *Polymer*, **47**:319–329.

[106] Zhang, H., Liechti, K.M. and Ravi-Chandar, K. (2009) "On the dynamics of localization and fragmentation - III. Effect of cladding with a polymer," *International Journal of Fracture*, **155**:101-118.

[107] Zhao, H. and Gary, G. (1995) "A three dimensional analytical solution of the longitudinal wave propagation in an infinite linear viscoelastic cylindrical bar. Application to experimental techniques," *Journal of the Mechanics and Physics of Solids*, **43**:1335–1348.

[108] Zhao, H. and Gary, G. (1997) "A new method for the separation of waves. Application to the SHPB technique for an unlimited duration of measurement," *Journal of the Mechanics and Physics of Solids*, **45**:1185–1202.

[109] Zhao, H., Gary, G. and Klepaczko, J.R. (1997) "On the use of a viscoelastic split Hopkinson pressure bar," *International Journal of Impact Engineering*, **19**:319–330.